AN EVALUATION OF THE THERMAL STABILITY OF CUBIC $Li_7La_3Zr_2O_{12}$ (LLZO) AND IMPLICATIONS FOR LLZO AS A SOLID-STATE LITHIUM ION CONDUCTING ELECTROLYTE

by

Steven Thomas Montoya

A thesis submitted in partial fulfillment
of the requirements for the degree

of

Doctor of Philosophy

in

Physical Chemistry

MONTANA STATE UNIVERSITY
Bozeman, Montana

May 2025

©COPYRIGHT

by

Steven Thomas Montoya

2025

All Rights Reserved

DEDICATION

To my family and friends that have supported me throughout this academic journey. Love you all!

ACKNOWLEDGEMENTS

I want to thank Dr. Rob Walker for his tireless work, and the rest of my committee, Dr. Erik Grumstrup, Dr. Nick Stadie, Dr. Paul Gannon, and Dr. Martin Mosquera, for their guidance throughout this journey. I would also like to thank the other members of the Walker research group both past and present, especially Tanner Henning, Shah Shanto, Steven Hisey, and Rhys Trousdale, for their help and great conversations. I would also like to thank Dr. Stephen Sophie, and members of the Sophie research group, Dr. David Driscoll, Dr. Stephen Haywood, and Matt Lessmeier, for their collaborative efforts. I would like to thank Serenity Juedeman, and our girls Aurora and Rosie for giving me support to finish this thing.

I would also like to thank the U.S. Army for funding us through DEVCOM Army Research Laboratory: under Cooperative Agreement (CA) Number W911NF-22-2-0021.

TABLE OF CONTENTS

1. INTRODUCTION 1

a. Batteries 1

i. Battery Principles 1

ii. Battery Types 2

b. Advantages and Disadvantages of Traditional Li^+ Batteries 7

c. All Solid-State Batteries 11

d. Lithium Lanthanum Zirconate (LLZO) 16

e. Methods 20

f. Thesis Outline 26

i. Chapter 2. 27

ii. Chapter 3 27

iii. Chapter 4 28

iv. Conclusions 29

2. LITHIUM VOLITILIZATION AND PHASE CHANGES DURING ALUMINUM-DOPED CUBIC $Li_{6.25}La_3Zr_2Al_{0.25}O_{12}$ (c-LLZO) PROCESSING. 31

a. Introduction 34

b. Materials and Methods 37

c. Results 39

d. Summary 49

3. DOPANT EFFECTS ON THE THERMAL STABILITY OF Li^+ CONDUCTING CUBIC $Li_7La_3Zr_2O_{12}$ 50

a. Introduction 53

b. Experimental Methods 55

TABLE OF CONTENTS CONTINUED

c. Results 58

d. Discussion 75

e. Conclusions 78

4. THERMAL HEAT TREATMENT AS STRATEGY FOR CLEANING t-LLZO AND c-LLZO SURFACES AND IMPROVING ELECTROCHEMICAL PERFORMANCE IN SOLID-STATE BATTERIES 80

a. Introduction 82

b. Methods 85

c. Results and Discussions 86

d. Conclusions 100

5. CONCLUSIONS AND FUTURE DIRECTIONS 101

a. Conclusions 101

b. Future Directions 104

i. Stress Induced Phase Transitions for LLZO 104

ii. Continued Work on Anneal Treatment vs Mechanical Polish Surface Cleaning Methods 107

REFERENCES CITED 109

APPENDIX: SUPPORTING INFORMATION FOR DOPANT EFFECTS ON THE THERMAL STABILITY OF Li^+ CONDUCTING $Li_7La_3Zr_2O_{12}$ 125

LIST OF TABLES

Table Page

1. Table 1.1 Solid State Electrolyte Material vs conductivity..... 15

2. Table 1.2 Comparison of SSBs polymer electrolyte materials, oxide, and sulfide materials. Check marks indicate strengths for a material in each category, - signs indicate neither a strength or a weakness, and X marks indicate weaknesses for a material. Adapted from Reference 61 16

3. Table 1.3 Symmetry assignments for c-LLZO vibrations..... 23

4. Table 3.1 Vibrational frequencies used to distinguish the three relevant materials (*c*-LLZO, LZO and La_2O_3) from each other. 61

5. Table 3.2 Time and temperatures of the DTA minima shown in Figure 3B. Times are in minutes, temperatures are in ˚C. The asterisk for Al-doped c-LLZO at 31.5 min/340˚C notes the derivative-type line shape shown in Figure 3B. 65

6. Table 3.3 Percentage of spectra showing LZO in mapping experiments (Figure 3) after sintering for 1 hour and 12 hours. The numbers in parentheses report the exact number of spectra showing evidence of LZO divided by the total number of spectra in a given mapping experiment. Uncertainties in these percentages are ±5%..... 68

7. Table 3.4 LZO percentage by dopant type and time sintered for a representative sample. Variances and ranges are included in the narrative. 75

8. Table 4.1 Frequencies and assignments for common Raman vibrational modes for LLZO and secondary phases..... 87

9. Table 4.2 Fit values for heat treated and mechanically polished *c*-LLZO using EIS data. 98

10. Table 5.1 Intensity ratios from vibrational modes of note from Figure 1. for each time point. 107

LIST OF FIGURES

Figure Page

1. Figure 1.1 Schematic of Lithium-ion battery with a lithium iron phosphate anode and a lithium metal anode. Adapted from Zhang et al. 6

2. Figure 1.2. Schematic of dendrite growth induced from SEI passivation layer on the surface of a lithium metal anode 10

3. Figure 1.3. Doping reaction of t-LLZO Raman spectra and crystal structure with both Nbi^{5+} doping schemes replacing one Zr^{4+} and a Li^{+} stablizing the cubic phase and Al^{3+} doping t-LLZO with 3 Li^{+} vacancies being created. Blue octahedra are ZrO_6, Orange dodecahedra are LaO_8, the red yellow and green spheres for t-LLZO are Li site atoms specific to t-LLZO, the green spheres are 96h site Li atoms and the red spheres are 24d site Li atoms for Al doped c-LLZO and for Nb doped c-LLZO the yellow spheres are Nb atoms, the blue spheres are La atoms and the green spheres are Zr atoms. 18

4. Figure 1.4. Raman spectra for a mixture of all three precursor powders: lithium carbonate, lanthanum oxide, and zirconium oxide. 19

5. Figure 1.5. Schematic of scattering and absorption events related to vibrational spectroscopy. 22

6. Figure 1.6. Raman spectra for t-LLZO, c-LLZO and the pyrochlore LZO. Materials provided by MSE (Tucson, Arizona). 24

7. Figure 2.1 A schematic showing mechanisms that create lithium concentration gradients in LLZO during sintering. As illustrated in the proposed reaction pathway below, lithium can volatilize from the material into the gas phase (as Li_2O) and be replaced by Li^{+} diffusing from the sample center to the sample edge. Li^{+} depletion at the sample center transforms *c*-LLZO into LZO, preventing Li^{+} back-diffusion and creating a LZO gradient that diminishes from the sample center to the edge 36

8. Figure 2.2. A schematic diagram illustrating the experimental procedure. A *c*-LLZO sample is sandwiched between two alumina plates and heated to 1000˚C for 1 hour. After cooling, Raman spectroscopy and X-ray diffraction show that the sample has formed LZO at its center with diminishing LZO concentrations towards the sample perimeter. 37

LIST OF FIGURES CONTINUED

Figure Page

9. Figure 2.3. A) Measured XRD patterns of commercial tetragonal (blue) and Al-stabilized cubic (red) LLZO and stick pattern showing lines associated with LZO. B) Measured Raman spectra of tetragonal (blue) and Al stabilized cubic (red) LLZO and Raman spectrum of LZO. 40

10. Figure 2.4. A) Heat map of spatially resolved LZO concentrations across the sintered cubic LLZO sample; B) Raman spectra from different points located on a line between the sample center and edge. C) Intensity ratios showing the intensity at 300 cm^{-1} (LZO) divided by the intensity at 648 cm^{-1} (*c*-LLZO). The horizontal line at 0.55 indicates the ratio corresponding to pure *c*-LLZO. 42

11. Figure 2.5. A) Schematic of sample used for cross sectional Raman mapping. Spectra were acquired from the center point between the two edges radially out from the sample center. B) Spectra from the different points along the sample interior. The dashed lines correspond to the LZO band intensity (at 300 cm^{-1}) and the LLZO band intensity (at 648 cm^{-1}). C) A plot of the LZO/LLZO intensity ratio as a function of position. Here, the 0 position is the mid-point between the two perimeter edges indicated in 6A. 44

12. Figure 2.6. Top: Measured XRD pattern from the surface of a sintered LLZO sample equivalent to the sample geometry used to acquire Raman data in Figure 4. Middle: Measured XRD pattern from 8 stacked LLZO sample cross sections equivalent to the geometry used to acquire Raman data shown in Figure 5. Bottom: Representative calculated XRD pattern of the top sample following Rietveld refinement. 46

13. Figure 2.7. A schematic representation of how the *c*-LLZO material changes during sintering and Li^+ loss through volatilization. The top panel (t= 0) notes a uniform composition across (and throughout) the pellet prior to sintering. The middle panel (t_1) shows an intermediate time during sintering as Li^+ is depleted at the sample center and LZO begins to form. The bottom panel shows the eventual complete conversion to LZO if the sample were left at high temperatures and all the Li^+ volatilized. 48

14. Figure 3.1. Schematic showing the experimental assembly using two alumina plates to cover the top and bottom of c-LLZO pellets sintered for 1 and 12 hours. In this configuration, Li^+could only volatilize from the pellet

LIST OF FIGURES CONTINUED

Figure Page

perimeter. Typical pellets measured 15 mm in diameter with a 1.2-1.5 mm thickness..... 55

15. Figure 3.2. Raman spectra for 3 dopants of c-LLZO (Ta, Nb, and Al) measured at the center and edge of sample pellets after each sample has been sintered for 1 hour. The diagram shows schematically where spectra were measured. Edge spectra were typically acquired within ~1 mm of each sample's perimeter. 60

16. Figure 3.3. Thermogravimetric analysis of Al, Ta, Nb plotted time vs derivative mass percent. **2b**. Derivative plot for TGA of Al, Ta, Nb and t-LLZO plotted time vs d[weight%]/dt. 64

17. Figure 3.4. Raman maps for Ta, Nb, and Al doped pellets sintered for 1 hr on the left and 12 hr on the right. 67

18. Figure 3.5. Waterfall plot of radial measured Ta-doped c-LLZO spectra for 1 hr sintered pellet. **5b**. Waterfall plot of radial measured Ta doped c-LLZO spectra for 12hr sintered pellet. **5c**. Waterfall plot of radial measured Al-doped c-LLZO spectra for 1hr sintered pellet. **5d.** Waterfall plot of radial measured Al-doped c-LLZO spectra for 12hr sintered pellet. 71

19. Figure 3.6 Radial distance from edge vs I_{300}/I_{650} ratio for each sample sintered. **6b.** Intensity of I_{940} where lanthanum oxide is measured from the center of Ta 1 hr and 12 hr sintered pellets to their edges. **6c.** Intensity ratio I_{940}/I_{300} measured radially from the center for Ta 1 hr and 12 hr sintered pellets. 72

20. Figure 3.7. XRD measured and calculated for 1 hr sintered Ta-doped c-LLZO pellet. LZO peak is marked for comparison. 73

21. Figure 3.8. XRD measured and calculated for 12 hr sintered Ta-doped c-LLZO pellet. LZO peak is marked for comparison.. 74

22. Figure 3.9 XRD measured and calculated for 12 hr sintered Al-doped c-LLZO pellet. LZO peak is marked for comparison. 75

23. Figure 4.1. Raman spectra of pre sintered t-LLZO, post sintered t-LLZO, and post annealed t-LLZO. 1b.In situ Raman spectra of heat treated (800 ℃ for 1 hr) post sintered t-LLZO pellet. 89

LIST OF FIGURES CONTINUED

Figure Page

24. Figure 4.2. Plot for intensity ratio I_{380}/I_{1064} from Figure 1 for each time point. Dashed line is linear regression for data.. 90

25. Figure 4.3. Expanded view of Figure 1b carbonate removal showing the lithium carbonate peak at 1064 cm^{-1}. 3b. Exponential decay kinetics for carbonate removal plotting time vs $\ln(I_{1064})$. 91

26. Figure 4.4. Thermal gravimetric analysis data for *t*-LLZO (black) and Al-doped *c*-LLZO (red) samples. The vertical dashed line at 77 minutes shows the time when the sample temperature reaches 800˚C. The horizontal dashed line at 87.5 weight % shows the threshold for LLZO decomposition and formation of LZO. (See Chapter 3.). 92

27. Figure 4.5 Raman spectra for post sintered t-LLZO, post heat treatment, and post 19 days in storage in desiccator before battery assembly. 93

28. Figure 4.6 Image of pre heat treated and post heat treated c-LLZO. 4b. Raman spectra for post sintered c-LLZO, post heat treated c-LLZO and post 2 weeks in storage. Spectra have been offset vertically for clarity.. 94

29. Figure 4.7 Raman spectra for mechanically polished Grafoil coated c-LLZO pellet, following polish, the day after and 1 week after. 95

30. Figure 4.8 Nyquist plot for averaged Z_{real} vs $-Z_{img}$ for mechanically polished and heat-treated *c*-LLZO pellets. Fitted curves are also plotted for both mechanically polished and heat-treated pellets. 97

31. Figure 4.9 Modified Randles circuit 98

32. Figure 5.1 Image through microscope objective of indented c-LLZO pellet. 1b. Raman spectra for indent 1 and 2 on c-LLZO pellet and control measurement. 104

ABSTRACT

Work described in this dissertation focuses on the properties and thermal stability of cubic lithium lanthanum zirconate (c-$Li_7La_3Zr_2O_{12}$ or *c*-LLZO), a lithium ion conducting ceramic generally regarded as a leading electrolyte candidate for all solid-state lithium-ion batteries. Experiments were carried out to characterize *c*-LLZO's thermal stability and identify mechanisms responsible for thermal induced degradation under conditions commonly used to sinter dense *c*-LLZO electrolytes. At room temperature the tetragonal phase of LLZO (*t*-LLZO) is thermodynamically stable but with a 10-fold smaller ion conductivity compared to *c*-LLZO. Different dopants are commonly used to stabilize *c*-LLZO under ambient conditions. Work described in this thesis examined *c*-LLZO where the cubic phase was stabilized by aluminum (Al^{3+}) substituting for lithium or either tantalum (Ta^{5+}) or niobium (Nb^{5+}) substituting for zirconium. Material stability for each doped sample was quantified using vibrational Raman spectroscopy (including spatially resolved Raman mapping), thermal gravimetric analysis (TGA), and X-ray diffraction (XRD). Results showed that heating Al-doped *c*-LLZO to 1000˚C leads to lithium volatilization and formation of a lithium deficient secondary phase, lanthanum zirconate ($La_2Zr_2O_7$ or LZO). A characteristic radial pattern showing the extent of LZO formation implies that lithium diffusion is much faster than Li_2O formation and volatilization. Ta-doped and Nb-doped *c*-LLZO are less thermally stable than Al-doped *c*-LLZO. These zirconium substituted materials lost more lithium when sintered and formed both LZO and La_2O_3. XRD experiments quantified the amount of LZO formed upon decomposition. After heating to 1000˚C with a 1-hour dwell at temperature, Al-, Ta- and Nb-doped samples showed 1.7, 13.1 and 17.9 % LZO content, respectively. A final study tested the role of post-sintering thermal treatment as a means of removing unwanted secondary materials and residues from the surface of *c*-LLZO. These last experiments compare the efficacy of thermal heating compared to mechanically polishing sintered *c*-LLZO samples in preparation for use as battery electrolytes. Electrochemical impedance spectroscopy measurements show a 1.7-fold increase in conductivity for samples that were thermally treated. Discoveries reported in this thesis should inform and guide processing strategies so that *c*-LLZO can be used effectively in new solid-state batteries.

INTRODUCTION

Batteries

Batteries are portable devices that convert chemical energy contained within active materials into electricity and products via electrochemical oxidation-reduction reactions.[1] Batteries have five main components: an anode (or negative terminal), a cathode (or positive terminal), current collectors that facilitate electron transfer to and from the electrodes during charge discharge cycles, an electrolyte that facilitates ion mobility between the electrodes, and a separator to prevent short circuits. Batteries leverage the electrochemical potential difference between half reactions occurring at the cathode and anode to drive ion current from the anode to the cathode through the electrolyte as electron current passes through an external circuit from the anode to the cathode.[2] Research described in this dissertation focuses on the lithium ion conducting solid state electrolyte lithium lanthanum zirconate or $Li_7La_3Zr_2O_{12}$ (LLZO) and the conditions that lead to this material breaking down into lithium ion insulating secondary phases. Before describing LLZO properties and knowledge gaps surrounding LLZO's behavior at elevated temperatures, this chapter will briefly describe basic battery principles and the benefits and limitations of liquid-electrolyte based lithium ion-based batteries. Subsequent sections summarize LLZO's properties and the methods used in this work to characterize LLZO's stability. This chapter concludes with brief summaries of discoveries resulting from these experiments and their impact on the community's understanding of LLZO stability.

Battery principles.

While a functional description of batteries is straightforward, these devices are complicated systems, where each battery component must be carefully matched to other components to ensure optimum performance and durability. Different anode/cathode pairs frequently require different electrolytes depending on a battery's intended application. In this context, a battery's electrochemical window is the voltage range over which an electrolyte will remain stable and not suffer detrimental reactions at either the cathode or anode.[3, 4, 5] The electrochemical window is often more than a battery's maximum theoretical voltage defined by the reduction and oxidation half reactions occurring at the anode and cathode, respectively.[6]

The first battery was developed in 1800 by Alessandro Volta who stacked zinc and copper metal plates separated with brine soaked cloth.[2, 7] Zinc has a standard hydrogen electrode reduction potential of -0.76 V and copper has a standard reduction potential of 0.34 V. The convention is that the cathode is the electrode with a higher standard reduction potential, meaning the copper electrode is the cathode and the zinc electrode is the anode. The relevant standard reduction half reactions for this device are:

$$Cu^{2+} + 2e^- \rightarrow Cu^0 \quad \mathcal{E}_0 = +0.34\,V$$

$$Zn^{2+} + 2e^- \rightarrow Zn^0 \quad \mathcal{E}_0 = -0.76\,V$$

In all batteries, the more positive standard reduction potentials ($\mathcal{E}_0$) describe the reaction happening at the cathode and the half reaction having the less positive standard reduction potential is reversed to describe the corresponding oxidation reaction at the anode.[1] For Volta's battery, Cu^{2+} is reduced at the cathode and Zn^0 is oxidized at the anode for a net potential difference:

$$\Delta\mathcal{E}_0 = \mathcal{E}_0^{cathode} - \mathcal{E}_0^{anode} = +1.10V$$

Batteries rely on a positive potential difference between the cathode and anode to spontaneously drive the two half reactions and produce current. To maintain charge balance in Volta's battery, Cu^{2+} ions in solution migrate to copper cathode, and Zn^{2+} ions move from Zn anode to electrolyte solution.

Battery types.

Since this first demonstration, battery technologies have employed the same principles to produce current from electrochemical reactions but with increasingly complex materials. Currently, more than 10 commercially available battery types are prevalent in energy storage, transportation, and consumer electronics. Lead-acid were the first developed rechargeable batteries and comprise the second largest fraction of the global battery market.[8, 9] Lead acid batteries use lead dioxide for the cathode, lead for the anode, and sulfuric acid for the electrolyte These batteries are primarily used for industrial energy storage where space is not a large consideration, and as starter batteries for vehicles. These batteries have energy density ranges between 30-50 Wh/kg and can support 300-1000 discharge/charge cycles, depending on depth of discharge.[10, 11] When discharging beyond 50% of their total capacity, lead acid batteries begin to experience irreversible degradation. This restriction places limits on the technologies that can utilize these batteries.

Sodium-ion batteries are a more recently developed rechargeable battery type, first developed and patented in 1968 by Krummer, Arbor and Weber at the Ford motor company.[12] Sodium ion batteries use Na^+ ions as charge carriers and typically use anode materials such as hard carbon, and layered transition metal oxides such as sodium iron oxide $NaFeO_2$.[13] Sodium

ion batteries have significantly higher energy densities (160 Wh/kg) than lead acid batteries with longer life cycles (2000 – 3000), and, importantly, sodium is one of the most abundant elements making sodium ion batteries more sustainable.[14, 6, 15] Due to these advantages sodium ion batteries were initial candidates for electric vehicles. The difficulties limiting sodium ion battery development revolve around finding suitable materials for anode and cathode components.[13] During initial stages in development, electrolytes and glove boxes were inadequate, making it difficult to measure electrode performance. Over time, interest in sodium ion batteries waned as more popular and commercially viable lithium-ion batteries emerged in the 1990s.[16] More recently in the mid-2000s, sodium ion batteries have garnered renewed interest as an alternative to lithium-ion batteries due to sodium's greater abundance and similar but lower theoretical energy density.[17]

Lithium-ion batteries are the fastest growing battery type available commercially, and lithium-ion battery technology remains an area of active scientific research.[18] Lithium-ion battery popularity stems from its versatility: these batteries are flexible and can be tailored to fit small devices in coordination with the electronics those devices employ. Small lithium-ion batteries are capable of powering consumer electronics due to their high energy densities (>150 Wh/kg).[19] When using lithium metal as an anode, lithium ion batteries have the highest theoretical energy density of any battery type, and they typically have a very wide electrochemical window.[20, 21] Lastly, lithium-ion batteries can accommodate a variety of anode, cathode, and electrolyte materials.

Traditional lithium-ion batteries typically have anodes comprised of graphite. However these batteries are designed to have increased stability, and with that stability, lower energy

densities result.[22, 23] Cathodes often consist of lithium metal oxide materials or phosphate-based materials. The electrolyte in commercial lithium-ion batteries is typically a carbonate solvent containing a dissolved lithium salt. Different materials for separators and additives to the electrolyte system are often included to help improve efficiency and prevent or slow material degradation.[24] Figure 1 shows a rechargeable lithium-ion battery schematic with a lithium metal anode, and a lithium iron phosphate ($LiFePO_4$ or LFP) cathode.[25] This battery schematic can be considered a general battery schematic for all lithium ion batteries. During discharge and as the battery produces current, lithium is oxidized at the anode and lithium ions migrate from the anode to the cathode as the electrons move from anode to the cathode through the external circuit powering a device. The relevant half reactions are as follows:

Anode: $Li(s) \rightarrow Li^+ + e^-$

Cathode: $FePO_4 + Li^+ + e^- \rightarrow LiFePO_4$ $\quad (\mathcal{E}_0 = 3.45\ V\ vs\ Li/Li^+)$

In this example, Fe(III) is reduced to Fe(II) at the cathode. The maximum cell voltage is 3.45 V due to LFP having a reduction potential of +3.45V vs lithium metal. To recharge the battery, an applied potential reverses the bias and the iron is re-oxidized to Fe(III) at the cathode releasing lithium ions back into the electrolyte. Under the applied electrochemical potential gradient, the lithium ions return to the lithium metal anode where they are reduced.

The solid electrolyte interphase or SEI layer is a layer that forms during initial charging of the battery from reactions of the electrolyte with the anode forming a passivation layer, allowing Li^+ transport, but preventing the flow of electrons. The cathode electrolyte interphase is a protective layer that forms on the surface of the cathode and prevents direct contact between

cathode and electrolyte, adding to battery stability. For a solid-state lithium-ion battery, the electrolyte acts as both an electrolyte and the separator preventing short circuiting.

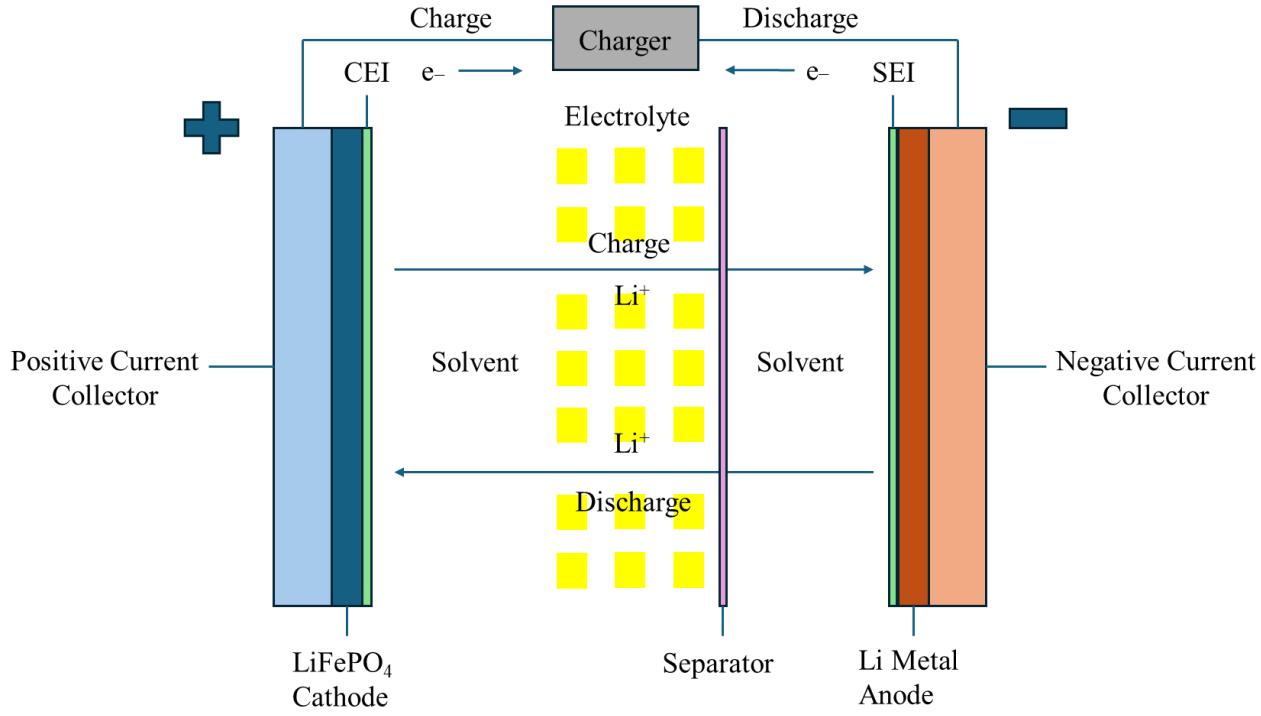

Figure 1. Schematic of Lithium-ion battery with a lithium iron phosphate anode and a lithium metal anode. Adapted from Zhang et al. [26]

While lithium-ion batteries remain a critical part of today's global energy infrastructure, they do have significant limitations. Ever since they were first produced, commercial lithium-ion batteries have been fabricated with organic liquid electrolytes. Liquid electrolytes restrict lithium-ion battery performance and durability. Organic electrolytes used in lithium-ion batteries cause serious safety risks and make these batteries susceptible to dendrite formation, as well as secondary reactions at either the anode or cathode. The following section discusses in more detail the advantages and disadvantages of traditional lithium-ion batteries that use organic liquid

electrolytes. The advantages and disadvantages of traditional lithium-ion batteries are compared to all solid-state batteries in the section below.

Advantages and Disadvantages of Traditional Li^+ Batteries

Electrochemical windows describe the voltage range available for stable electrolyte performance. The wider this window, the larger the potential voltage range where a battery can operate and, in principle, provide more energy. Lithium bis(trifluoromethanesulfonyl)imide (LiTFSI), a recently developed electrolyte salt for lithium ion batteries, has a high electrochemical window of 1.9-4.9 V vs. Li^+/Li when in solution.[27] If a battery is subjected to a potential greater than the electrochemical window maximum voltage during charging, unwanted secondary reactions will occur, depleting electrolyte material and lowering battery performance. Organic liquid electrolyte-based batteries typically have narrower electrochemical windows than solid-state lithium-ion batteries. For example, the garnet structured solid oxide electrolyte c-LLZO has an electrochemical window of 0-6.4 V vs Li^+/Li while a second solid-state electrolyte, $Li_{1.5}Al_{0.5}Ge_{1.5}(PO_4)_3$, has an electrochemical window of 1.7 – 5.25 V vs Li^+/Li .[4, 28]

Energy density, another common metric used to assess battery performance, is the amount of energy stored in a battery per unit mass A device with a mass of 1 kg and an energy density of 100 Wh/kg would be able to use 1 W of power for 100 hrs or 100 W for 1 hr or any combination of power and time whose product equals 100 Wh. This metric is important because it determines the weight of a battery based on the Wh of the intended application. An electric vehicle needs considerable power for long durations, but battery weight becomes an important consideration as it affects the amount of power needed to move the vehicle.[29] Thus, a very high energy density of greater than 350 Wh/kg is necessary to match gasoline driving ranges for

electric vehicles.[29] Industrial energy storage batteries that have near unlimited space and no weight requirements can use a lower energy density battery having a higher cycling lifespan and stability. Typical lithium-ion batteries have energy densities between 150 – 250 Wh/kg, much higher than other battery types, with noncommercial lithium-ion batteries being the only type of batteries to have much higher energy densities.[30] Due to this intrinsic property, Li^+ batteries are very suitable to be used in technologies that require smaller batteries such as portable electronics and transportation.

Power density is another performance metric used to assess batteries. Power density is the amount of power per unit volume or mass and measures how much power can be accessed quickly. A high power density material such as A123 Systems patented batteries utilizing a LFP cathode and graphitic anode has power densities as high as 2.5 kW/kg, compared to Samsung's INR21700 batteries that utilize a graphitic anode and a lithium cobalt oxide cathode and have lower power densities of 0.5 kW/kg.[31, 32, 33] The higher the power density, the more available power in a charge/discharge cycle. Power density is related to ionic conductivity so materials with higher conductivity will have higher power densities. Lithium-ion batteries have power densities comparable to or higher than all other commercially available battery types.

A battery cycle describes one discharge followed by a recharge to full capacity, and the cycle life is defined as the number of cycles a battery can undergo before its charge capacity has degraded beyond a certain point, typically 60-80% of its original charge capacity. Lithium-ion batteries have cycle lifetimes between 1000-3000 cycles on average.[17] Some new lithium ion batteries still under development have reported lifecycles as high as 10,000.[34] In contrast,

batteries such as flow batteries can cycle between 3000 – 15000 times but only have energy densities of approximately 20 Wh/kg.[35]

Intrinsic to all lithium-ion batteries operating with liquid electrolytes is the solid electrolyte interphase (SEI) that forms between an electrode and the electrolyte. SEI layers can be between 1.5 and ~600 nm thick, with electrical resistance ranging from 1 to 10 $\Omega\, cm^2$.[36] SEI films have been described as multilayer structures with an inorganic inner layer made up of LiF, Li_2O and Li_2CO_3 components and an organic outer layer, made up of Li_2EDC (EDC = ethylene carbonate) and ROLi (R depends on solvation environment).[37] The two layers facilitate Li^+ transport with the organic layer being porous and permeable to electrolyte solvent molecules. Both layers can grow during charge/discharge cycles and will do so nonuniformly starting at the anode/electrolyte interface.[38] The SEI improves the chemical and electrochemical stability of the electrolyte but often results in capacity fading, or a gradual loss of a battery's ability to hold charge, increasing a battery's internal impedance and resulting in diminished power densities.[39] SEI layers are known to grow when the redox potentials are outside the electrochemical window of the electrolyte material.[21]

The most significant constraint limiting lithium ion battery performance is the tendency of traditional lithium-ion batteries to form dendrites that can eventually lead to device shorting and catastrophic failure.[40] Dendrites are solid lithium metal structures that originate at electrodes and extend into the electrolyte. Dendrites can eventually pierce charge separators and short circuit a battery.[40] The resulting failure can cause a spark and ignite the highly flammable organic electrolyte solution.[41] This phenomenon is responsible for many of the iconic images that have documented lithium-ion battery failures in automobiles, aircraft, and consumer electronics.

These failures pose grave health threats not only because of the heat and destruction resulting from the fire, but the burning electrolytes also create toxic hydrogen fluoride gas.[42] An additional threat is thermal runaway where one battery fails and ignites neighboring cells.[43] Dendrites form when the mass transport of lithium ions is limited due to degradation of the battery's electrolyte or electrode. Dendrites form more easily when an SEI layer has created surface inhomogeneities at the electrode/SEI interface.[44] Figure 2 is reproduced from an earlier report describing dendrite formation mechanisms and shows how dendrites grow from a lithium metal anode. [43] Initially electrolyte materials and additives react with the lithium metal anode forming a SEI layer. Importantly, This SEI layer forms inhomogeneous Li^+ conduction pathways, which form these nucleation sites for Li metal dendrite growth. These pathways concentrate and reduce Li^+ ions to form Li metal structures that fracture the SEI layer as they grow. The SEI layer then will re-form over these clusters, and the process repeats to create longer dendrites.

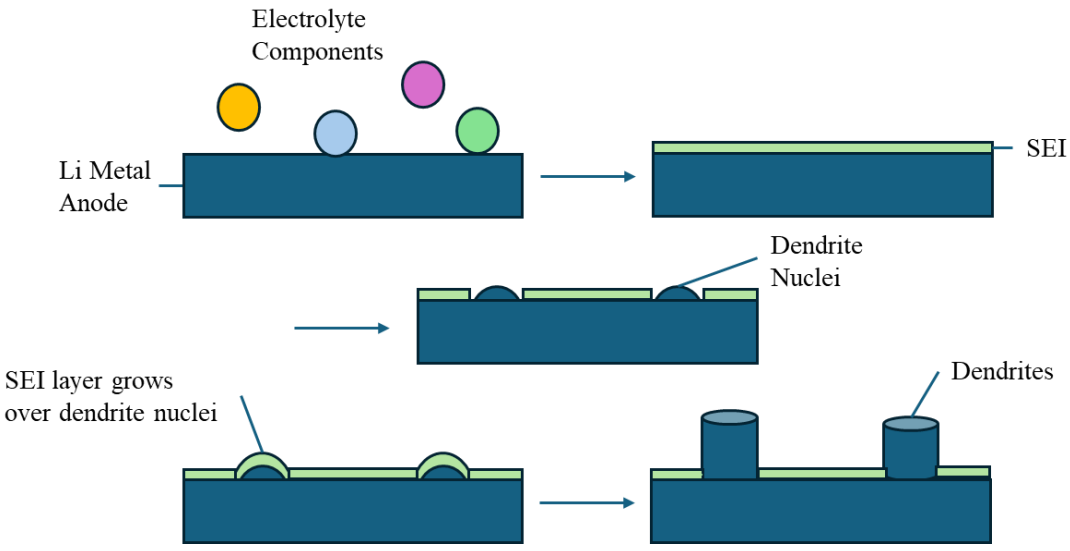

Figure 2**.** Schematic of dendrite growth induced from SEI passivation layer on the surface of a lithium metal anode.[45]

For SSBs, dendrites form at both low and high current densities where active lithium is deposited on electrode, typically on anode nucleation sites.[45] As they form, dendrites lower current densities and reduce battery performance. These effects occur because dendrites consume electrolyte Li^+ ions, so the longer each dendrite becomes, and the more numerous they are, less Li^+ is available to participate in the battery's redox chemistry.[46] Mechanical properties such as toughness determine the suppression of dendrite propagation, where more mechanically tough solids reduce dendrite formation compared to weaker solids.

To suppress dendrite formation and uncontrolled and uneven SEI formation, researchers have tested numerous strategies. One approach is to include additives in the electrolyte designed to occupy active generation sites where dendrites are believed to originate.[47] Other efforts have focused on designing separators with tailored pore structures to impede dendrite growth through the battery.[48] Still other tactics have developed protective electrode coatings that inhibit continued SEI growth during battery operation and thus prevent dendrite formation.[49] Many of the problems arising from SEI and dendrite formation can be significantly reduced or eliminated by replacing the liquid electrolyte with an electronically insulating, Li-ion conducting solid state electrolyte.[50] Work described in this dissertation examines the stability of one such solid state electrolyte, $Li_7La_3Zr_2O_{12}$ or LLZO.

All Solid-State Batteries

SSBs represent a new and attractive approach to harnessing the power of lithium-ion batteries, and these devices have the potential to overcome the two primary limitations – dendrites and SEI formation – that have traditionally hindered lithium-ion battery performance. Materials like lithium lanthanum titanate ($LiLaTiO_4$, LLTO), have intrinsic mechanical strength

that applies compressive stress on dendrite tips, hindering their growth.[51] SSBs typically have nonflammable, solid electrolytes such as inorganic sulfide $Li_{10}GeP_2S_{12}$ and glass-ceramic Li_2S-P_2S_5 separating the cathode and anode. With dendrite resistance and being nonflammable, solid-state electrolytes stand out as attractive alternatives for next-generation lithium-ion batteries. Furthermore, SSBs are capable of sustaining high energy densities because they are more dense than traditional electrolytes allowing for more Li^+ transport.[52] Due to safety concerns, liquid electrolytes cannot use high energy density lithium metal anodes (>400 Wh/kg), but SSBs can.[53] Finally, SSBs allow for more compact battery designs making more efficient batteries capable of storing more total energy.

SEI layers do not form at the electrode-electrolyte interface in SSBs.[50] SSBs are defined by interfaces formed between a *solid* electrode and a *solid* electrolyte, meaning that the organic content forming the outer layer in a liquid electrolyte lithium-ion battery SEI is not present. Materials such as Li_2O and Li_2CO_3 can still introduce unwanted impedance across SSB electrode-electrolyte interfaces, but these secondary phases behave differently compared to the inner SEI layer in batteries having liquid electrolytes.[53]

A recent review by Y. K. Sun considered the suitability of SSBs in the transportation sector. [52] Sun listed three categories with challenges that must be overcome if lithium ion SSBs are to become commercially viable. Specifically, interface contact between grains of electrolyte materials, as well as incompatible electrolyte-electrode interfaces can be problematic if the ceramic electrolyte weakens. This weakening increases interface resistance, can limit ionic mobility, and can alter the electronic structure of the material at the interface, causing harmful secondary reactions that deplete the electrolyte. Improving interface compatibility is crucial to

commercializing SSBs. An additional challenge to SSB development involves increasing energy density of SSBs; increasing energy densities can be accomplished by creating ultra-thin electrolytes with thick, high-energy cathodes. Using lithium metal anodes in SSBs to create stable, high energy, dense batteries, and methods to improve fabrication of dendrite resistant cells are additional research topics being studied. The last major challenge for SSBs is finding and characterizing new cathode, anode and electrolyte materials.

SSBs are more stable at higher temperatures than liquid electrolyte-based lithium-ion batteries. Typical lithium-ion batteries with liquid electrolytes break down over time and this degradation can be thermally accelerated when the temperature rises above 100˚C. SSBs perform better at temperatures as high as ~250℃ due to more thermally stable electrolyte materials.[54] SSBs are also more environmentally friendly as fewer volatile and toxic compounds are used during manufacture compared to liquid electrolyte batteries.[55] These advantages over liquid-electrolyte devices position SSBs to be a more sustainable and more reliable source of energy storage compared to traditional lithium-ion batteries.

Before lithium-ion SSBs can become commercially viable, several important limitations must be overcome. The most significant drawback to SSBs is that solid state electrolytes typically have lower ionic conductivities (<2.0 mS/cm) than liquid electrolyte batteries (>2.4 mS/cm).[50] Lower conductivities result in lower power densities and limited utility. Even if more charge is stored in SSBs, that capacity cannot be accessed as quickly as in liquid electrolyte batteries.

Some SSBs have displayed higher ionic conductivities such as sulfide electrolytes. One example is LPS ($75Li_2S$-$25P_2S_5$) that has an ionic conductivity as high as 17 mS/cm.[56] Materials

such as LPS, however, are extremely sensitive to air and moisture, and reactions can result in release of hydrogen sulfide gas. Other sulfide electrolytes like Li_6PS_5Cl also have high conductivities (>2 mS/cm), but decomposition at solid electrolyte – electrode interfaces remains a challenging problem.[57] Furthermore, interfacial resistance on account of poor contact between solid - solid interfaces, typically due to inhomogeneity in electrolyte or electrode surfaces, lead to low charge transfer efficiencies and unstable cycling stability.[58] The mechanical stresses of operating a battery through many cycles can further degrade these interfaces resulting in rapidly diminishing performance.

SSBs have a wider electrochemical window than liquid-electrolyte batteries allowing for higher voltages and higher energy densities. However outside of the electrochemical window of stability, SSBs can be more susceptible to oxidative or reductive secondary reactions that are accelerated at electrode/electrolyte interfaces, increasing interfacial resistance and diminishing charge transfer efficiency.[59] SSB electrolytes are also often extremely brittle making handling and durability during manufacturing difficult to scale. Finally, materials suitable for solid state battery applications are significantly less well studied than liquid electrolyte lithium batteries. [60]

Electrolytes being considered for SSBs fall into 3 broad categories: sulfide based electrolytes, polymer based electrolytes and oxide based electrolytes.[61] Table 2 shows conductivities for some common solid-state electrolytes. Of these electrolytes, oxide electrolytes tend to have the best chemical stability, but they can be challenging to match to cathode and anode materials leading to high interfacial impedances. Table 3 is adapted from a recent report listing the three most commonly researched types of SSB electrolytes, along with a qualitative review of their fundamental electrolyte properties.[61] Oxide materials are varied and include

glassy materials like lithium phosphorus oxynitride (LiPON), and hard ceramic materials including the garnet lithium lanthanum zirconate (LLZO).

Table 2. Solid State Electrolyte Material vs conductivity.

Electrolyte Type	Electrolyte	Ionic Conductivity
Oxide Type	LiPON	3.2×10^{-3} mS/cm[62]
Oxide Type	NASICON	1 mS/cm[63]
Oxide Garnet Type	LLZO	Up to 1 mS/cm[68]
Sulfide Type	LPS	17 mS/cm[64]
Sulfide Type	Argyrodites (Li_6PS_5Cl)	Up to 16.1 mS/cm[65]
Polymer Type	Poly(ethylene oxide)/Li^+ salt	0.4 mS/cm[66]
Polymer Type	Polyacrylonitrile/Li^+ salt	0.1 - 10 mS/cm[67]
Liquid Electrolyte	$LiPF_6$	2.4 - 6.2 mS/cm[68]

Polymer electrolytes are similar in some ways to liquid organic electrolytes. The polymer materials are composed of repeating monomer units that form molecular chains and contain dissolved lithium salts. The long chains facilitate lithium mobility within the electrolyte material. Like liquid electrolyte batteries, polymer electrolytes have three components: organic polymer chains, lithium salts and additives to improve performance. Polymer electrolytes typically have poorer ionic conductivities compared to other solid state electrolytes, but they do have the best interface compatibility with electrodes.

Table 3. Comparison of SSBs polymer electrolyte materials, oxide, and sulfide materials. Check marks indicate strengths for a material in each category, - signs indicate neither a strength or a weakness, and X marks indicate weaknesses for a material. Adapted from Reference 61.[61]

Electrolyte Type	Mechanical Strength	Chemical Stability	Electrochemical Stability	Interface Compatibility	Li-Ion Conductivity
Sulfide	✓	X	X	✓	✓
Oxide	✓	✓	✓	X	✓
Polymer	X	–	✓	✓	–

LLZO

This thesis will focus on the characterization of the garnet type oxide electrolyte, LLZO. This material shows great promise with a high ionic conductivity (up to 1mS/cm), a wide electrochemical window (reported as high as 0 – 9V vs. Li^+/Li, although more recent reports suggest 0 - 6V is a more widely accepted value) and high thermal stability.[69] Unlike most other solid electrolytes, LLZO are compatible with lithium metal anodes endowing LLZO-based batteries with high energy densities. However, LLZO is susceptible to secondary phase formation during processing, which results from decomposition of the primary phase, LLZO, into decomposition products.[70] These secondary phases reduce Li^+ conductivity and diminish device performance.[71] Furthermore, LLZO is relatively brittle, increasing the likelihood of a battery's structural failure.

LLZO has two primary solid phases, a cubic phase and a tetragonal phase. LLZO's tetragonal phase (t-LLZO) is stable at room temperature. t-LLZO is also mechanically tougher than the cubic phase but has poor electrochemical properties (10^{-6} S/cm ionic conductivity).[72] Cubic LLZO (c-LLZO) has enviable electrochemical properties but is more brittle and prone to fracturing than t-LLZO. c-LLZO is the preferred phase for battery applications as it has a higher

ionic conductivity (~1 mS/cm).[73] c-LLZO was first discovered when t-LLZO was being sintered and aluminum metal leached into the material from the alumina boat containing the original sample.[74] This doping stabilized the c-LLZO phase at room temperature, which is typically only stable above 650 ℃, and created significant interest in this new electrolyte material. Since the original reports of stabilized c-LLZO's discovery, over 59 different dopants have been reported to stabilize c-LLZO at room temperature.[75]

c-LLZO can be stabilized by four dopant types: aliovalent Li site dopants, Zr site dopants, La site dopants and O site dopants. Li and Zr site dopants are the most common dopants.[75] Ions such as Al and Ga are lithium site dopants and force the loss of three lithium ions for every Al^{3+} or Ga^{3+} substituted into the LLZO crystal structure.[76] Ta and Nb are Zr site dopants and for every Ta^{5+} or Nb^{5+} atom added, one lithium ion and one zirconium ion are displaced.[77] As a rule, Zr substituted c-LLZO will have more lithium ions per unit formula than Li-substituted c-LLZO. Figure 3 shows Raman spectra and crystal structures for t-LLZO, Al-doped c-LLZO, and Nb-doped c-LLZO.

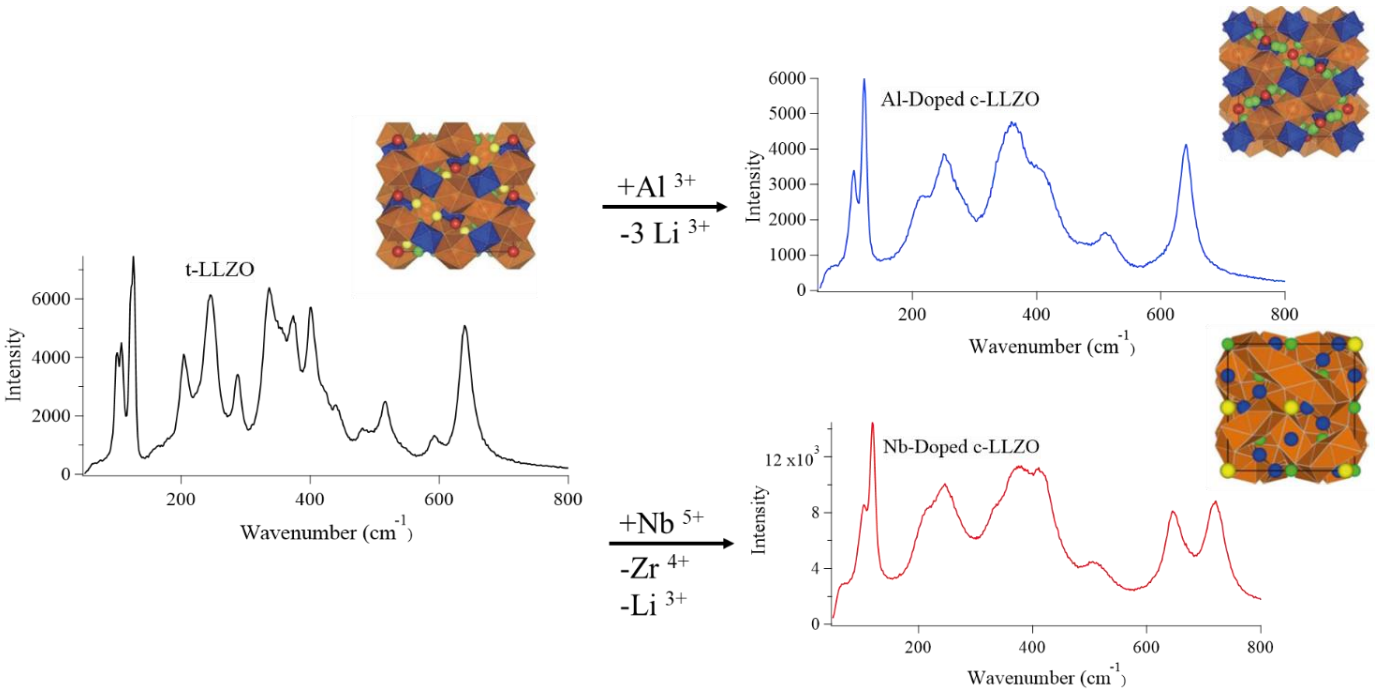

Figure 3. Doping reaction of t-LLZO Raman spectra and crystal structure with both Nbi^{5+} doping schemes replacing one Zr^{4+} and a Li^{+} stablizing the cubic phase and Al^{3+} doping t-LLZO with 3 Li^{+} vacancies being created.[78] Blue octahedra are ZrO_6, Orange dodecahedra are LaO_8, the red yellow and green spheres for t-LLZO are Li site atoms specific to t-LLZO, the green spheres are 96h site Li atoms and the red spheres are 24d site Li atoms for Al doped c-LLZO and for Nb doped c-LLZO the yellow spheres are Nb atoms, the blue spheres are La atoms and the green spheres are Zr atoms.

When LLZO is doped, lithium is displaced, leading to fewer lithium ions per formula unit than the stoichiometric 7 lithium ions in *t*-LLZO. This substitution increases lithium vacancies in the material and enables higher lithium ion conductivity.[77] *c*-LLZO has a cubic $Ia\bar{3}d$ crystal structure that includes two different types of lithium sites. One site consists of octahedral locations in the lattice (designated 96h) and the other sites are in tetragonal locations (designated 24d).[79] When filled with an aliovalent substituent, 24d sites block four Li^{+} conduction pathways, whereas 96h sites when filled only block one conduction pathway. Zr site doped *c*-LLZO creates Li vacancies while not blocking any conduction pathways, increasing overall ionic conductivity.

Li site dopants such as Al or Ga, favor filling 24d sites, making the ionic conductivity of Al doped *c*-LLZO to be lower than Zr site dopant materials such as Ta-doped *c*-LLZO.

Both *c*-LLZO and *t*-LLZO are difficult to synthesize and process because both materials are brittle and will chemically decompose into lithium depleted secondary phases when subjected to high temperatures and/or mechanical stress. All LLZO synthesis methods do start with a series of precursor materials including a lithium source, a lanthanum source and a zirconium source, and, for cubic LLZO, a dopant oxide source. These precursors are typically are heated to temperatures between 900 and 1250 ℃ for synthesis times greater than 2 hrs but are temperature dependent. Lithium carbonate, lanthanum oxide and zirconium oxide are frequently used as sources for the Li, Zr, and La with dopant sources depending on the dopant of choice.[80] Figure 4 shows the Raman spectra of the above mentioned precursors individually and mixed together. Some methods start with pre-synthesized lanthanum zirconate ($La_2Zr_2O_7$) or LZO mixed with a lithium source, some additional La_2O_3 and a dopant in order to synthesize the c-LLZO.[81]

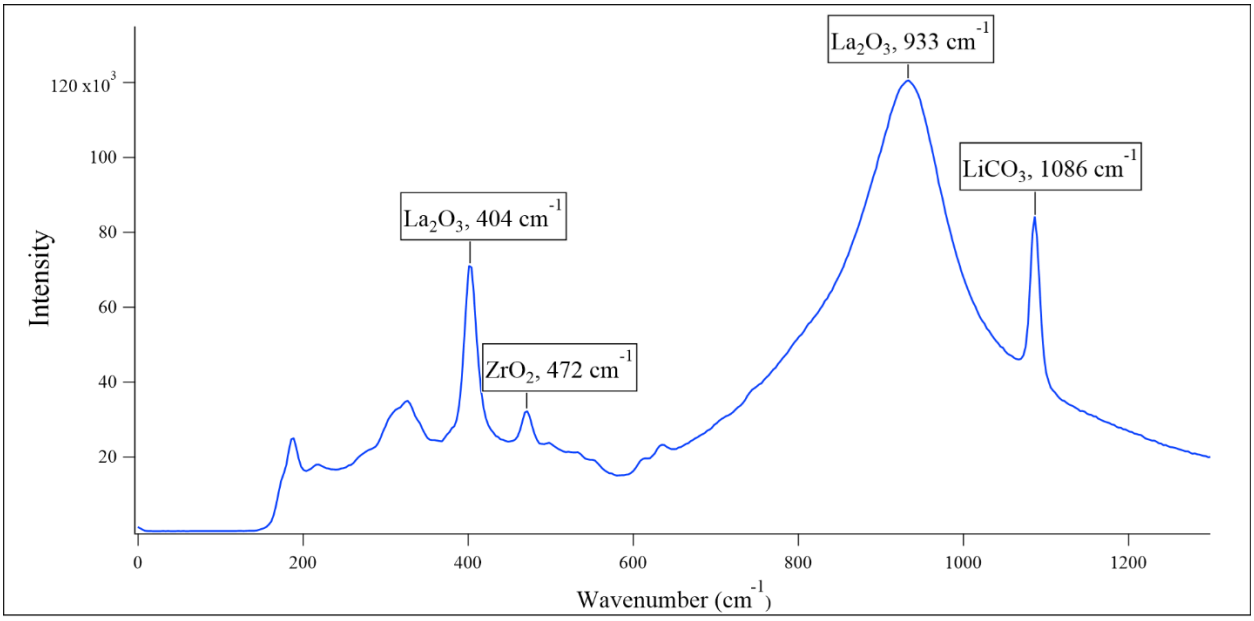

Figure 4. Raman spectra for a mixture of all three precursor powders: lithium carbonate, lanthanum oxide, and zirconium oxide.

Many different analytical tools have been used previously to characterize c-LLZO and assess sample purity by phase identification. The primary tools used in this dissertation are vibrational Raman spectroscopy, thermogravimetric analysis and X-ray diffraction and will be discussed in the methods section below.

Methods

LLZO characterization in this dissertation relies on 3 primary characterization methods: vibrational Raman spectroscopy, thermal gravimetric analysis (TGA), and X-ray diffraction (XRD). Specifically, Raman spectroscopy is used to identify changes in material composition and spatial distribution induced by heating LLZO. Raman spectroscopy can determine if LLZO has degraded, where it has degraded, and the specific degradation products that have formed. TGA experiments report on a material's thermal stability under inert and oxidizing atmospheres, and indirectly highlight Li^+ diffusion rates. XRD quantifies material structure and composition (as mass percent) in processed samples.

Raman spectroscopy. Raman spectroscopy is a technique that measures a change in energy due to inelastic light scattering that accompanies a change in vibrational state. Specifically, Raman spectra report changes in vibrational frequencies using the equation $\Delta\tilde{\nu} = 10^7 x \left(\frac{1}{\lambda_0} - \frac{1}{\lambda_1}\right)$ where $\Delta\tilde{\nu}$ is the Raman shift in wavenumbers (cm^{-1}) and λ_0 is the laser wavelength and λ_1 the scattered wavelength (in nm).[82] The range of a typical Raman spectrum is between 50 and 4500 cm^{-1}, and each measured spectrum is a unique fingerprint that is material dependent. Raman microscopy can spatially resolve data from a (solid) sample using a

microscope, probing where phases are on a materials surface.[83] Depending on the microscope objective properties (i.e. numerical aperture, magnification), Raman microscopy can distinguish material changes on a sample surface with μm or sub-μm resolution. Pairing spatial information with structural and chemical changes that occur during sintering and additional heat treatment provides insight into the mechanisms responsible for these changes. For work described in this dissertation, Raman microscopy is used to measure differences in LLZO samples that have been subjected to different heat treatments under oxidizing, inert, and reducing atmospheres.

Figure 5 shows a diagram illustrating how light scattering can change the vibrational state of a system. Rayleigh scattering is an elastic scattering event where the incident frequency is the same as the scattered frequency. This type of scattering event is the most common type of light scattering. If the oscillating electric field of incident light is sufficiently strong, the field can interact with an incident molecule or material and transfer vibrational population by 1 vibrational quantum number. This type of scattering is called Raman scattering. If the vibrational state of a molecule changes by $\Delta v = +1$, the resulting light is said to be Stokes scattered and emerges with a longer wavelength or lower frequency than the incident light. If the vibrational state of a molecule changes by $\Delta v = -1$, the resulting light is said to be anti-Stokes scattered and emerges with a shorter wavelength or higher frequency than the incident light. The difference in energy between the Stokes (or anti-Stokes) scattered light and the incident light matches the energy separation between the two involved vibrational states. Stokes scattered light is typically stronger than anti-Stokes scattered light because at room temperature, most molecular vibrations are in their ground state.[84]

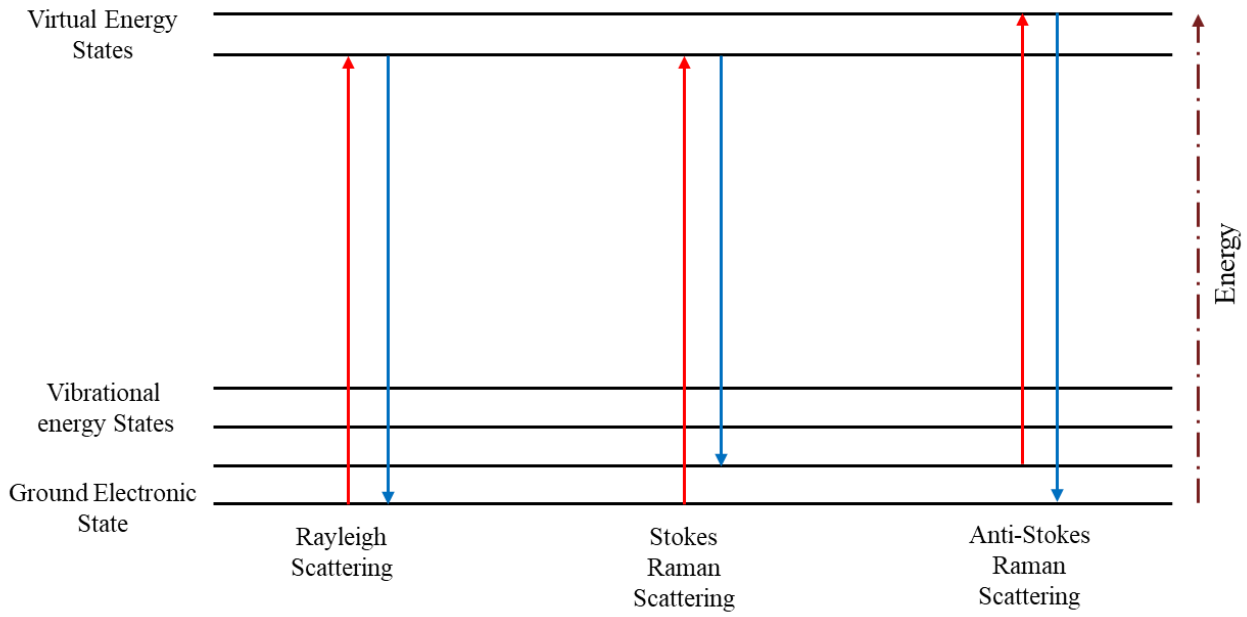

Figure 5. Schematic of scattering and absorption events related to vibrational spectroscopy.

For Raman spectroscopy to be useful as a tool to study LLZO, the vibrational modes of LLZO and common degradation products or contaminants must be identified. c-LLZO has 9 Raman active vibrational bands. These nine vibrational bands can be divided into 5 categories:[85] 1) the heavy O-La-O stretching modes cations in the 100-150 cm^{-1} region; 2) an oxygen bending region found between 200 – 290 cm^{-1} having one distinct peak at 255 cm^{-1} assigned to T_{2g} and A_{1g} oxygen bending bands; 3) lithium oxygen stretching between 330 – 405 cm^{-1} consisting of two overlapping peaks; 4) a second lithium oxygen stretching region between 480 to 550 cm^{-1}; and 5) metal oxide stretching assigned to zirconium oxide octahedra near ~645 cm^{-1}. Table 4 lists the symmetry assignments and their vibrational frequencies for *c*-LLZO's Raman active modes. *t*-LLZO has 23 vibrational modes that can also be split into approximately 5 main regions, these regions overlap with *c*-LLZO but show additional peak splitting due to lowered symmetry.

Table 4 Symmetry assignments for c-LLZO vibrations.

Symmetry Assignment	c-LLZO vibrational mode energy (cm^{-1})	Atoms involved in predicted phonon motion
T_{2g}	107	O-La-O stretching
E_g	121	O-La-O stretching
T_{2g}	144	O bending
T_{2g}	209	O bending
A_{1g}	251	O bending
T_{2g}	361	Li-O stretching
E_g or T_{2g}	410	LiO
T_{2g} or E_g	514	LiO
A_{1g}	645	ZrO_6

Being able to distinguish between both LLZO polymorphs as well as common degradation products/contaminants (LZO, Li_2CO_3, and La_2O_3) is foundational for understanding LLZO's chemical changes resulting from sample processing. LZO, La_2O_3 and both polymorphs of LLZO do not have any vibrations in the 1000-1200 cm^{-1} range so lithium carbonate is easily resolved.[86] Similarly La_2O_3 has a lone peak at 935 cm^{-1} making it easy to distinguish from other materials.[87] LZO, unlike La_2O_3 and Li_2CO_3, has 4 primary peaks, and all but one overlaps with both polymorphs of LLZO.[88, 89] This unique feature in an LZO spectrum appears at 300 cm^{-1} and has a narrow linewidth between two LLZO vibrational regions. Figure 6 shows room temperature Raman spectra for Al – doped c-LLZO, undoped t-LLZO and LZO.

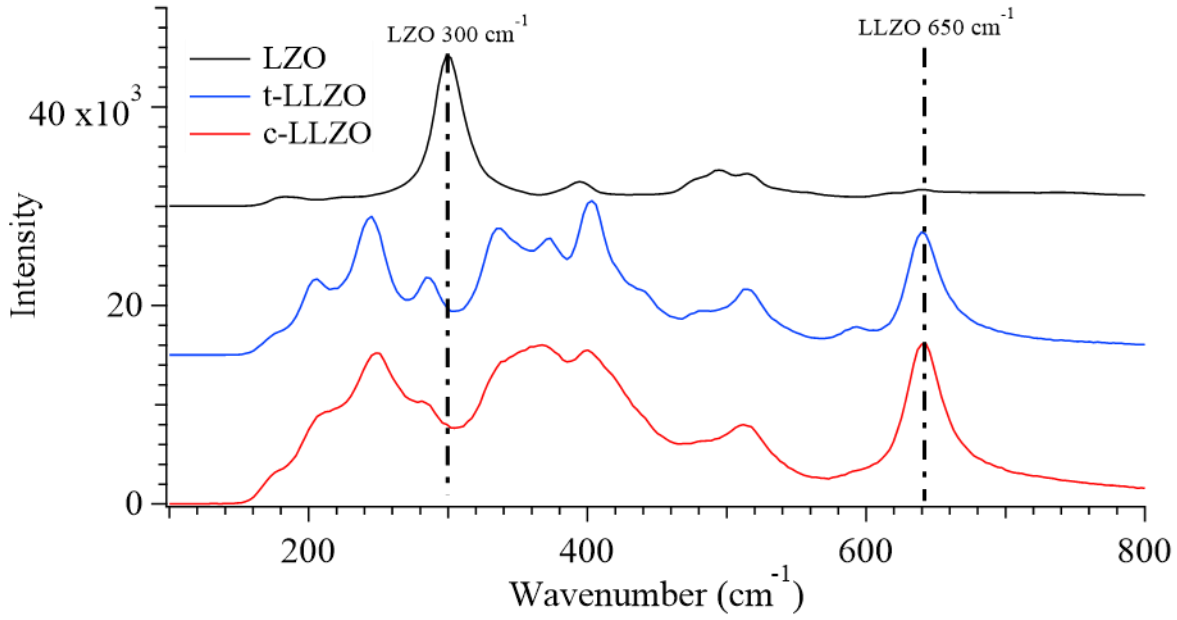

Figure 6. Raman spectra for t-LLZO, c-LLZO and the pyrochlore LZO. Materials provided by MSE (Tucson, Arizona).

X-ray Diffractometry. XRD is a nondestructive technique that relies on constructive and destructive interference from diffracted x-rays to create a diffraction pattern that can be analyzed to determine crystal symmetry. Diffraction results from Bragg's Law:

$$n\lambda = 2d \sin\theta$$

where n is an integer, λ is the incident wavelength, d is the distance between the diffracting planes of the material, and θ is the angle of incidence. [90]

Typical XRD data show diffracted signal as a function of 2θ. Different crystal symmetries give rise to different lattice parameters depending on their symmetries. A crystal structure having a simple cubic symmetry has 1 lattice constant which is the length/width/height of the unit cell, a, and the angle between all unit vectors, α, is 90°. This condition makes it so d, the spacing between adjacent lattice planes, is directly proportional to a. A more complicated

crystal symmetry such as monoclinic has three unique lattice constants, *a*, *b* and *c*, and two angles α and β where $\beta \neq 90°$. This condition makes the relationship with d spacing and *a*, *b*, and *c* much more complicated than a simple cubic system and is defined by the equation:

$$\frac{1}{d^2} = \frac{1}{\sin^2\beta}\left[\frac{h^2}{a^2} + \frac{k^2}{b^2} + \frac{l^2}{c^2} + \frac{2hlcos\beta}{ac}\right]$$

Rietveld refinement is a mathematical tool used for structure determination of an unknown material based on a measured XRD pattern. However, when paired with peak matching software, where an open database of every published XRD pattern can be compared to a measured XRD pattern, Rietveld refinement can be used to calculate mass percent composition for heterogeneous (diffracting) materials. This calculation is performed by refining parameters such as lattice parameters and peak shapes, to achieve a fit between the reference patterns and the measured patterns. During the Rietveld refinement, scaling factors which are related to the concentration of each phase are also refined, and the ratio of the scaling factors are used post-refinement to calculate the mass percent of each phase of the sample. This analysis is useful in calculating how material processing changes material composition. Relevant for work described in this dissertation are the XRD patterns showing how thermal stress under oxidizing conditions drives *c*-LLZO to decompose into materials including LZO and La_2O_3 and the relative amounts of these decomposition products. We note here that La_2O_3 can be difficult to evaluate in terms of mass percent in the sample due to overlap between La_2O_3 peaks and LZO and LLZO peaks. Due to this calculations of La_2O_3 mass percents below 2% are not accurate. XRD measurements, and Rietveld refinements by extension, are only sensitive to crystalline materials, and so amorphization of the material of interest will result in poor calculations.

Thermogravimetric analysis. Thermogravimetric analysis or TGA is a technique that uses a very sensitive balance coupled with a carefully calibrated furnace to record mass loss as a function of temperature. The TGA used for studies described in this dissertation can perform experiments under both inert and oxidizing conditions. Data typically take the form of mass loss (expressed in terms of % of sample) vs. temperature.[91] Often, TGA data show mass loss occurring not as a monotonic process but, rather, in a series of steps. In these instances, differential thermal analysis (DTA) is an effective means of identifying those temperatures corresponding to specific mass-loss events. DTA data show the derivative of mass loss with respect to time. When a material's mass loss passes through an inflection point, a plot of $\frac{d(mass\ loss)}{dt}$ vs. time will reach a maximum corresponding to the time (and temperature) where the sample is changing mass at the fastest rate.

TGA experiments can also be run in a pseudo-isothermal fashion. In these instances, the instrument is ramped to the desired temperature as quickly as possible and then the sample dwells at that temperature as the balance records mass loss. The TGA instrument used in this work can be ramped at 50˚C/min. The advantage to using this isothermal method is that the rate of mass loss can be tracked vs. time *at constant temperature* meaning that the data can be treated using traditional kinetic models.

Thesis Outline

This thesis is composed of chapters that have either been published or submitted for publication in the peer reviewed literature or are currently in preparation for submission. Consequently, each chapter may contain redundant material describing the properties of LLZO and/or the analytical

tools used to characterize LLZO and the secondary phases that form. A summary of the individual chapters is provided below.

Chapter 2: Lithium Volatilization and Phase Changes During Aluminum-Doped Cubic $Li_{6.25}La_3Zr_2Al_{0.25}O_{12}$ (*c*-LLZO) Processing

Chapter 2 uses Raman mapping to investigate material changes of Al-doped c-LLZO that occur during sintering. Results show that lanthanum zirconate or LZO is found in the center of sintered pellets, but the Raman intensity of the 300 cm^{-1} LZO peak continues to reduce the further from the center the measurements were taken. This LZO gradient is approximately 6 mm in diameter determined by Raman heat mapping of the 300 cm^{-1} peak. This radially symmetric LZO gradient, with less Li^+ concentration at the sample center, and more Li^+ at the sample edge, indicates that lithium volatilization must be faster than Li^+ diffusion, and so when LLZO is decomposed to form LZO, Li^+ back diffusion is prevented at the pellet center increasing the growth of this gradient. XRD results using two different measurement geometries were used to calculate how much LZO is in the sample (3%), and how much LZO is in the gradient area (18%). This work has been published in the journal *Crystals*. (Montoya September 2024, https://doi.org/10.3390/cryst14090795)

Chapter 3: Dopant Effects on the Thermal Stability of Li+ Conducting cubic-$Li_7La_3Zr_2O_{12}$

Expanding on the findings from Chapter 2, Chapter 3 investigates how dopant type affects thermal degradation by comparing the behavior of lithium substituted Al-doped c-LLZO with that of zirconium substituted Ta and Nb doped c-LLZO. These studies also examine the role of sintering time in c-LLZO degradation by comparing samples sintered for 1 and 12 hours.

Raman spectra show that the Ta-doped and Nb-doped samples form more LZO and the LZO was distributed across the sample. In contrast, LZO formation in the Al-doped sample remained tightly confined to the sample center. Additionally, the Ta-doped and Nb-doped samples showed clear evidence of La_2O_3 formation indicating significantly more lithium depletion during sintering. The Al-doped sample showed only traces of La_2O_3. These results were supported by TGA measurements. TGA results from the three samples showed sooner onset for mass loss, as well as longer mass loss events for Ta and Nb doped c-LLZO samples compared to Al doped c-LLZO. XRD results confirmed Raman and TGA results, showing a 7 to 10x increase in LZO mass percentage for Ta and Nb doped c-LLZO in comparison to Al doped samples. This indicates that Al doped c-LLZO is easier to process due to less decomposition and homogenous behavior. This work is currently under review at the ACS journal *Applied Energy Materials*.

Chapter 4: Thermal annealing as a tool for cleaning t-LLZO and c-LLZO and improving electrochemical performance.

Chapter 4, unlike Chapters 2 and 3, focuses on the post-sintering step of processing LLZO to render it suitable for use as a solid-state electrolyte. Ceramic materials, especially LLZO, must be cleaned post sintering to allow for good surface contact between LLZO and cathodes/anodes. Typical cleaning methods involve mechanically polishing the surface of LLZO with sandpaper, this will smooth the surface, as well as rid the surface of any chemical contaminants. Recently published work demonstrated a novel thermal cleaning treatment in an inert atmosphere that effectively cleaned a c-LLZO surface of lithium carbonate. Our work in chapter 4 expands on this initial discovery with three critical improvements. The first improvement is that the thermal treatment does not require an inert atmosphere, but instead can be carried out with air at lower

temperatures (800 ℃ vs 900 ℃). At this lower temperature, we observe no LZO growth indicating that these conditions are below a threshold temperature that leads to c-LLZO degradation and the formation of secondary phases. The second improvement is the generalization of the thermal cleaning treatment which was used to clean c-LLZO pellets of surface protective residues that remain after the initial sintering. This coating is typically made of graphitic sheets and leaves a carbon residue. The third improvement is the observation that this high temperature thermal cleaning method improves both chemical stability of LLZO during storage, as well as we saw a ~2x increase in conductivity compared to mechanically polished samples. Results indicate that thermally cleaning LLZO post sintering has considerable advantages compared to traditional cleaning methods.

Chapter 5: Conclusions and Future Directions

Chapter 5 summarizes the findings for chapters 2, 3, and 4, and outlines future directions for this work. The primary finding from research described in this dissertation is that c-LLZO is a complicated material that is sensitive to processing conditions and susceptible to secondary phase formation that compromises its ionic conductivity. The identity of the dopant used to stabilize LLZO's cubic phase affects the material's thermal stability and the thermal degradation pathways. Despite this sensitivity to sintering temperatures, heating at lower temperatures proved to be a very effective means at removing surface contaminants (like carbonates) and residues (like graphitic carbon), leaving a pristine c-LLZO surface ready to bind to electrodes. Thermally cleaning c-LLZO in this way resulted in conductivities that were ~2-fold higher than samples that were mechanically polished.

Future work on this project would likely focus on two specific topics: 1) thermally treating post-sintered LLZO for improved use as a SSB electrolyte and 2) leveraging the mechanical strength of t-LLZO and conductivity of c-LLZO to create more durable, high performance electrolytes. Thermally treating post-sintered c-LLZO has led to noticeable improvements in electrochemical performance when compared to traditional cleaning methods. The origins of these improvements, however, remain largely unknown. Surface roughness measurements can be used to determine if mechanically polishing is leaving a rough surface compared to thermally cleaning. The second project would be carried out in collaboration with Professor Stephen Sophie's research group in Mechanical and Industrial Engineering. Prof. Sofie and his team have manipulated LLZO so that applied indentation will drive stress induced phase transitions (from c-LLZO to t-LLZO). This processing is intended to inhibit dendrite growth by 'squeezing off' cracks created by dendrites by forcing the adjacent c-LLZO to transform into the mechanically tougher t-LLZO.

CHAPTER TWO

LLITHIUM VOLITILIZATION AND PHASE CHANGES DURING ALUMINUM-DOPED CUBIC $Li_{6.25}La_3Zr_2Al_{0.25}O_{12}$ (c-LLZO) PROCESSING

Contribution of Authors and Co-Authors

Manuscript in Chapter 2

Author: Steven Thomas Montoya

Contributions: Collected and analyzed all data, generated figures and wrote manuscript in preparation for publication, addressed reviewers comments.

Co-Author: Shah Ali Haider Shanto

Contributions: Made pellets, measured replicated data, made 1 figure and wrote pressing method section.

Co-Author: Robert A. Walker

Contributions: Helped plan experimental program and interpret results. Edited and assisted in preparation of the manuscript.

Manuscript Information

Steven T. Montoya, Shah A. H. Shanto, Robert A. Walker

Crystals

Status of Manuscript:
☐ Prepared for submission to a peer-reviewed journal
☐ Officially submitted to a peer-reviewed journal
☐ Accepted by a peer-reviewed journal
☒ Published in a peer-reviewed journal

Published by MDPI
In Volume 14, Issue 9, 795 (2024)
Doi: 10.3390/cryst14090795

LITHIUM VOLITALIZATION AND PHASE CHANGES DURING ALUMINUM-DOPED CUBIC $Li_{6.25}La_3Zr_2Al_{0.25}O_{12}$ (*c*-LLZO) PROCESSING

Steven T. Montoya[a], Shah A. H. Shanto[b], and Robert A. Walker[*a,b]

[a]Department of Chemistry and Biochemistry, Montana State University, Bozeman, MT 59717

[b]Montana Materials Science PhD Program, Montana State University, Bozeman, MT 59717

[*]corresponding author, rawalker@montana.edu

Abstract. Stabilized $Li_{6.25}La_3Al_{0.25}$ Zr_2O_{12} (cubic LLZO or *c*-LLZO) is a Li^+ conducting ceramic with ionic conductivities approaching 1 mS-cm. Processing *c*-LLZO so that it is suitable for use as a solid state electrolyte in all solid state batteries, however, is challenging due to the formation of secondary phases at elevated temperatures. Work described in this manuscript examines the formation of one such secondary phase $La_2Zr_2O_7$ (LZO) formed during sintering *c*-LLZO at 1000˚C. Specifically, spatially resolved Raman spectroscopy and X-ray Diffraction (XRD) measurements have identified gradients in Li distributions in the Li ion (Li^+) conducting ceramic $Li_{6.25}La_3Al_{0.25}$ Zr_2O_{12} (cubic LLZO or *c*-LLZO) as a function of thermal processing. Sintering *c*-LLZO under conditions relevant to solid state Li^+ electrolyte fabrication conditions lead to Li^+ loss and the formation of new phases. Specifically, sintering for 1 hour at 1000˚C leads to Li^+ depletion and the formation of the pyrochlore lanthanum zirconate ($La_2Zr_2O_7$ or LZO), a material known to be both electronically and ionically insulating. Circular *c*-LLZO samples are covered on the top and bottom surfaces exposing only the 1.6 mm thick sample perimeter to the furnace's ambient air. Sintered samples show a radially symmetric LZO gradient

with more LZO at the center of the pellet and considerably less LZO at the edges. This profile implies that Li^+ diffusion through the material is faster than Li^+ loss through volatilization, and that Li^+ migration from the center of the sample to the edges is not completely reversible. These conditions lead to a net depletion of Li^+ at the sample center. Findings presented in this work suggest new strategies for LLZO processing that will minimize Li^+ loss during sintering, leading to a more homogeneous material with more reproducible electrochemical behavior.

Introduction.

All solid-state batteries (ASSBs) represent the next generation of energy storage devices.[92, 93, 94] Defined by their solid ion-conducting electrolytes, ASSBs promise improved safety as well as higher energy densities relative to traditional batteries that rely on liquid or gel electrolytes to convey ions between electrodes. Such advances are needed if Li^+ and other alkali ion-based batteries are to assume greater roles in transportation and large-scale grid power applications.[95] Given the intrinsic advantages that ASSBs *should* have over their liquid electrolyte counterparts, considerable attention has focused on the discovery and development of new solid-state materials having sufficiently high ionic conductivities as well as material compatibility with electrodes including elemental Li metal electrodes.[96]

One such material identified for ASSBs is garnet structured lithium lanthanum zirconate ($Li_7La_3Zr_2O_{12}$ or LLZO). Cubic LLZO (or *c*-LLZO) has a relatively high ionic conductivity (~1 mS/cm), good thermal stability, and wide electrochemical window.[97] Furthermore, *c*-LLZO is not overly reactive to humidity and is chemically compatible with solid Li electrodes.[98] LLZO is typically in its tetragonal phase (*t*-LLZO) at room temperature, and *t*-LLZO has an ion conductivity approximately 2 orders of magnitude less than *c*-LLZO.[93] Preserving *c*-LLZO's

high conductivity at ambient temperatures requires stabilizing the cubic phase with cation dopants such as Al, Ta, Nb, and others.[97, 99, 100] Doping creates lithium vacancies that allow for greater ionic conductivity. Several reports have discovered that *c*-LLZO's conductivity peaks with Li^+ stoichiometries of 6.25 – 6.5.[101, 102]

Despite *c*-LLZO's many attractive properties as a solid-state, Li^+ conducting electrolyte, the material itself is very challenging to fabricate and process.[103] Li^+ volatilization together with c-LLZO's intrinsic phase instability at ambient temperatures require careful attention to all steps during fabrication and processing.[104, 105, 106, 107] Small differences in starting material purity as well differences in sintering procedures and uncharacterized thermal gradients can all contribute to heterogeneity in the desired *c*-LLZO product.[108, 109] Efforts to improve *c*-LLZO quality and stability have included adding excess Li (in the form of Li_2CO_3) to accommodate Li volatilization during sintering as well as fast sintering procedures to limit Li loss and resulting phase heterogeneity.[110, 111] Li_2CO_3, however, can also segregate to the surface forming a metal carbonate layer that serves as an insulator between the electrode and the electrolyte. Li^+ depletion will lead to the formation of new undesirable material phases including a lanthanum zirconate pyrochlore ($La_2Zr_2O_7$ or LZO) that is known to have both electronic and ion insulating properties.[112, 113, 114]

Findings presented in this study characterize the LZO that forms as the result of sintering *c*-LLZO at 1000˚C. LZO formation is associated directly with decreasing Li^+ content and indirectly with Li volatilization (often as Li_2O).[92] By making use of spatially resolved vibrational Raman measurements together with X-ray diffraction, we characterize LZO formation in a pellet that has been sintered at 1000˚C while covered on its top and bottom with inert substrates,

meaning that the only way Li can volatilize from the sample is by leaving from the (round) sample's perimeter. (Figure 1)

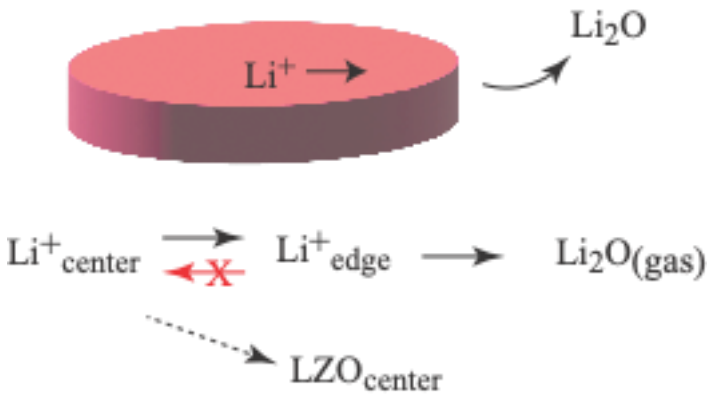

Figure 1. A schematic showing mechanisms that create lithium concentration gradients in LLZO during sintering. As illustrated in the proposed reaction pathway below, lithium can volatilize from the material into the gas phase (as Li_2O) and be replaced by Li^+ diffusing from the sample center to the sample edge. Li^+ depletion at the sample center transforms *c*-LLZO into LZO, preventing Li^+ back-diffusion and creating a LZO gradient that diminishes from the sample center to the edge.

Data show that LZO forms having a higher concentration at the center of the sample and lower concentrations closer to the edges. This discovery implies that Li^+ diffusion in the material is faster than Li volatilization so that Li lost from the sample through volatilization at the sample perimeter is quickly replaced by Li^+ diffusing from the center of the material in response to a concentration gradient. Furthermore, Li^+ migration from the center to the edge cannot be completely reversible, otherwise the sample would have a uniform Li^+ concentration in the material and a more uniform distribution of secondary phases that form as the Li^+ evaporates.

Materials and Methods.

Sample processing. A 15-mm diameter LLZO pellet was prepared using Aluminium-doped, cubic phase LLZO (*c*-LLZO) powder (manufactured by Ampcera, distributed by MSE Supplies). Initially, the powder was weighed in a plastic boat and transferred to a glass beaker where it was mixed with a small amount of organic polymer binder. The LLZO-binder mixture was poured into a 15-mm diameter pellet press die set and subjected to compression using a manual hydraulic press at 495 MPa for 10 seconds. Subsequently, the compressed pellets were placed in a muffle furnace and sintered at 1000°C for one hour, with alumina slides covering both the top and bottom surfaces. A schematic illustration of the experimental procedure is shown in Figure 2.

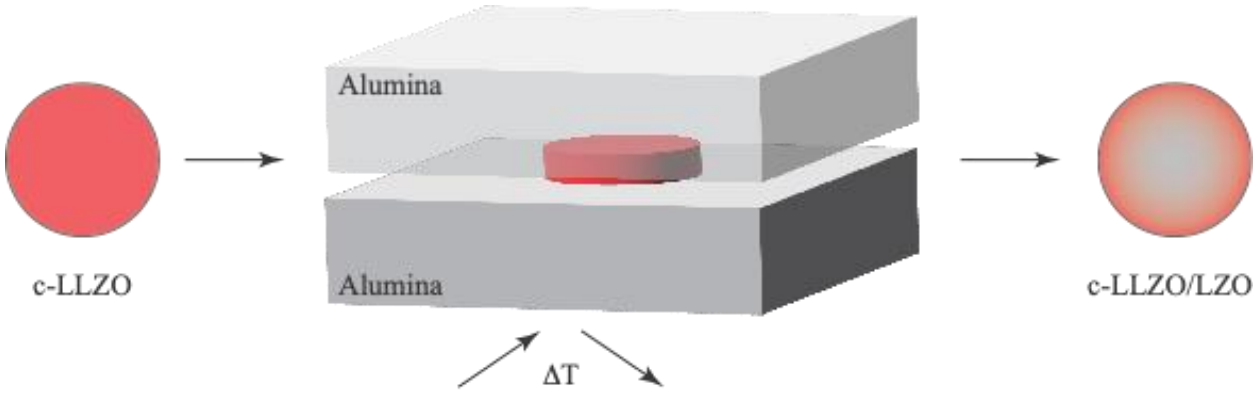

Figure 2. A schematic diagram illustrating the experimental procedure. A *c*-LLZO sample is sandwiched between two alumina plates and heated to 1000˚C for 1 hour. After cooling, Raman spectroscopy and X-ray diffraction show that the sample has formed LZO at its center with diminishing LZO concentrations towards the sample perimeter.

The sintering process consisted of ramping the temperature from ambient to 1000 ˚C at 5 ˚C per minute, holding at 1000 ˚C for one hour and cooling at 5˚ C per minute back to ambient temperature. In all the studies reported in this work, LLZO samples measured 15 mm in diameter with a thickness of 1.6 mm.

Characterization – Raman spectroscopy. Raman spectra were acquired using a Renishaw InVia Raman microscope equipped with a 488 nm single line argon ion laser (488 nm). All spectra were recorded using 0.1 mW of incident laser power. Wire 3.3 software for the microscope enables mapping measurements that scan either part of one field of view or create a montage that can be scanned across to create an image of the material. A mapping measurement of 15 x 2 was used for the Raman data in this report, however, a 15 x 15 scan was used to ensure the data was reproducible and evenly dispersed. All Raman scans were using 100% laser power for 10 seconds with 3 acquisitions. The laser spot size in these experiments had an approximate 5 μm diameter. Mapping data were acquired using Renishaw's Wire 3.3 software and spectra were analyzed using Igor Pro (Wavemetrics).

Characterization – X-ray diffraction. All XRD data were acquired using a 1kW Bruker D8 Advance X-ray diffractometer rotational stage and processed using Diffrac Eva and MDI Jade peak matching software. We placed a sintered LLZO pellet onto a microscope slide that has clay underneath and pressed it down in a deep sample holder until flat and then placed the sample holder in the diffractometer. Data were acquired from $2\theta = 8^{\circ}$ to 80° with .2 seconds per step with .05 degree steps. All peak PDFs were taken from the ICDD full database. All Rietveld refinements and elemental analyses were performed with Jade peak match report functionality.

Results

This work is motivated by the need to understand the phase stability and phase changes that occur in *c*-LLZO during the processing required to create viable Li^+ ion conducting electrolytes for ASSB applications. The most likely products to form as *c*-LLZO loses lithium through volatilization are *t*-LLZO and LZO. Figure 3a. shows the XRD patterns for these three materials. As expected, *c*-LLZO (red, space group $Ia\bar{3}d$) has a simpler diffraction pattern with 21 observed diffraction peaks compared to *t*-LLZO's 32 diffraction peaks (blue, space group $I4_1/acd$, PDF 04-018-9023). The *c*-LLZO pattern resulted in a lattice constant of 12.972 Å Figure 1a also shows the 2θ locations of LZO's (black) diffraction peaks (space group $Fd\bar{3}m$, PDF 04-008-6353, lattice constant 10.800 Å). These data were used to calculate material composition in the processed samples. Figure 3b. shows Raman spectra for *c*-LLZO, *t*-LLZO, and LZO. In general, the LLZO spectra are characterized by strong vibrational bands in 3 regions. A collection of oxygen bending modes are centered near 250 cm^{-1}, vibrations between 300 – 600 cm^{-1} are assigned to Li-oxygen stretching vibrations and the symmetric stretching motion of ZrO_6 octahedra is assigned to the strong feature between 635 and 650 cm^{-1}.[98 100] Despite these similarities, several differences are important to note. First, features are more sharply resolved in the *t*-LLZO relative to the *c*-LLZO. Second, the *t*-LLZO spectrum does contain several smaller features not observed in the *c*-LLZO spectrum. Two such vibrational bands in the *t*-LLZO spectrum appear at 284 cm^{-1} and 593 cm^{-1}.

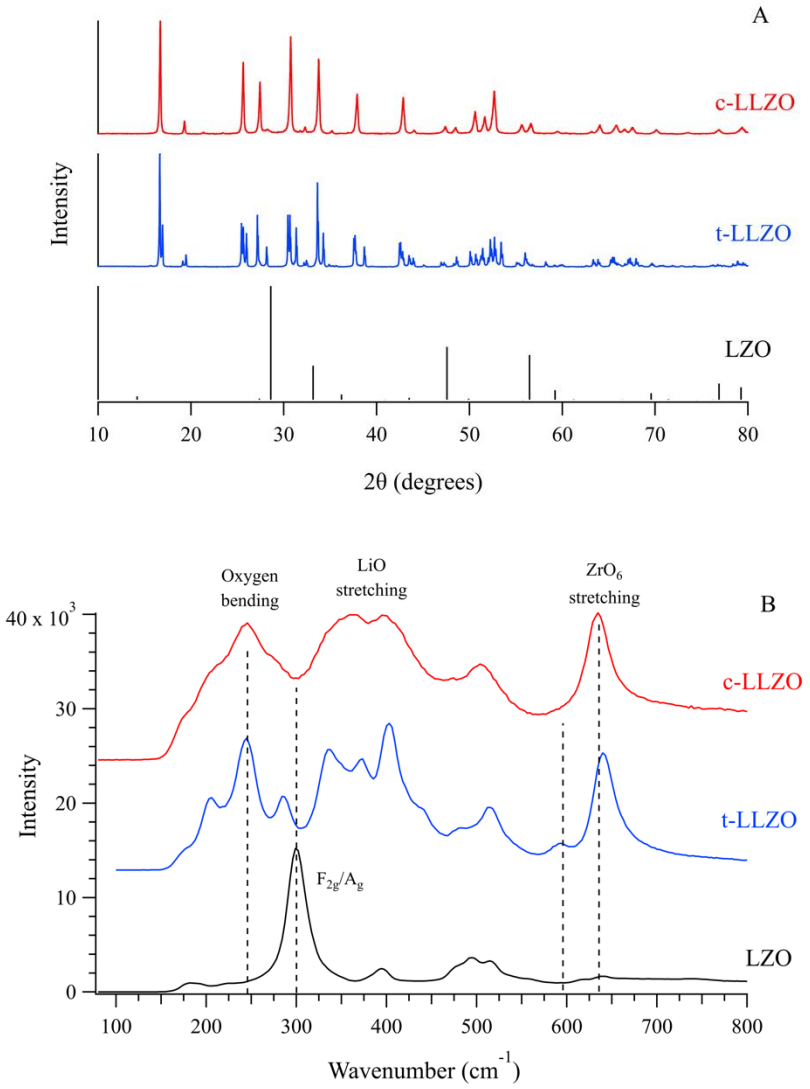

Figure 3. A) Measured XRD patterns of commercial tetragonal (blue) and Al-stabilized cubic (red) LLZO and stick pattern showing lines associated with LZO. B) Measured Raman spectra of tetragonal (blue) and Al stabilized cubic (red) LLZO and Raman spectrum of LZO.

LZO's XRD pattern and vibrational Raman spectrum are simpler than those of *t*-LLZO and *c*-LLZO, with one dominant feature centered at 300 cm^{-1} assigned to F_{2g} and/or A_{1g} lattice vibrations.[89] Notably, this vibrational feature falls at a frequency where both *t*-LLZO and *c*-LLZO are spectroscopically quiet although the broad phonon structure of *c*-LLZO retains some

intensity at this frequency. In the analyses below, we will compare spectral intensity at 300 cm^{-1} to spectral intensity of the ZrO_6 stretching vibrations near 645 cm^{-1} to assess how much LZO has formed during processing. Based on the data above, we note that the limits of this intensity ratio range from 0.55 (pure *c*-LLZO) to ≥10.0 (pure LZO). (If comparing LZO to *t*-LLZO, the ratio ranges from 0.40 (pure *t*-LLZO) to ≥10.0 (pure LZO), although in the data shown below, we never observe conclusive evidence that *t*-LLZO has formed.

Given that the top and bottom of the *c*-LLZO pellet are covered with alumina blocks (Figure 2), the only way Li can be lost through volatilization is from the pellet edge. Figure 4A shows a software mapping image of the LLZO pellet after sintering at 1000˚C for 1 hour. This image is a collection of still image viewer snapshots that are stitched together using the Wire 3.3 software provided with the InVia microscope. Figure 4A contains two separate images. The image on the right illustrates the intensity at 300 cm^{-1} in the Raman spectra acquired at each spot using heat map imagery. In this case, the brighter red (at center) corresponds to higher intensities (and more LZO) and the darker red at the edges corresponds to lower intensities (and less LZO).

The image in Figure 4A implies more LZO formed in the center of the pellet compared to the edges. Figure 4B shows the spectra taken radially from the pellet center. While each spectrum has the general appearance of c-LLZO, the spectra closest to the center show clear evidence of a new band appearing at 300 cm^{-1} indicating the growth of LZO. Figure 4C plots the ratio of the LZO intensity divided by the *c*-LLZO ZrO_6 vibration intensity (at 648 cm^{-1}). The dashed horizontal line designates a ratio of 0.55 or the limit of pure *c*-LLZO with no detectable LZO. From these data, we conclude that after sintering, the *c*-LLZO sample has a measurable

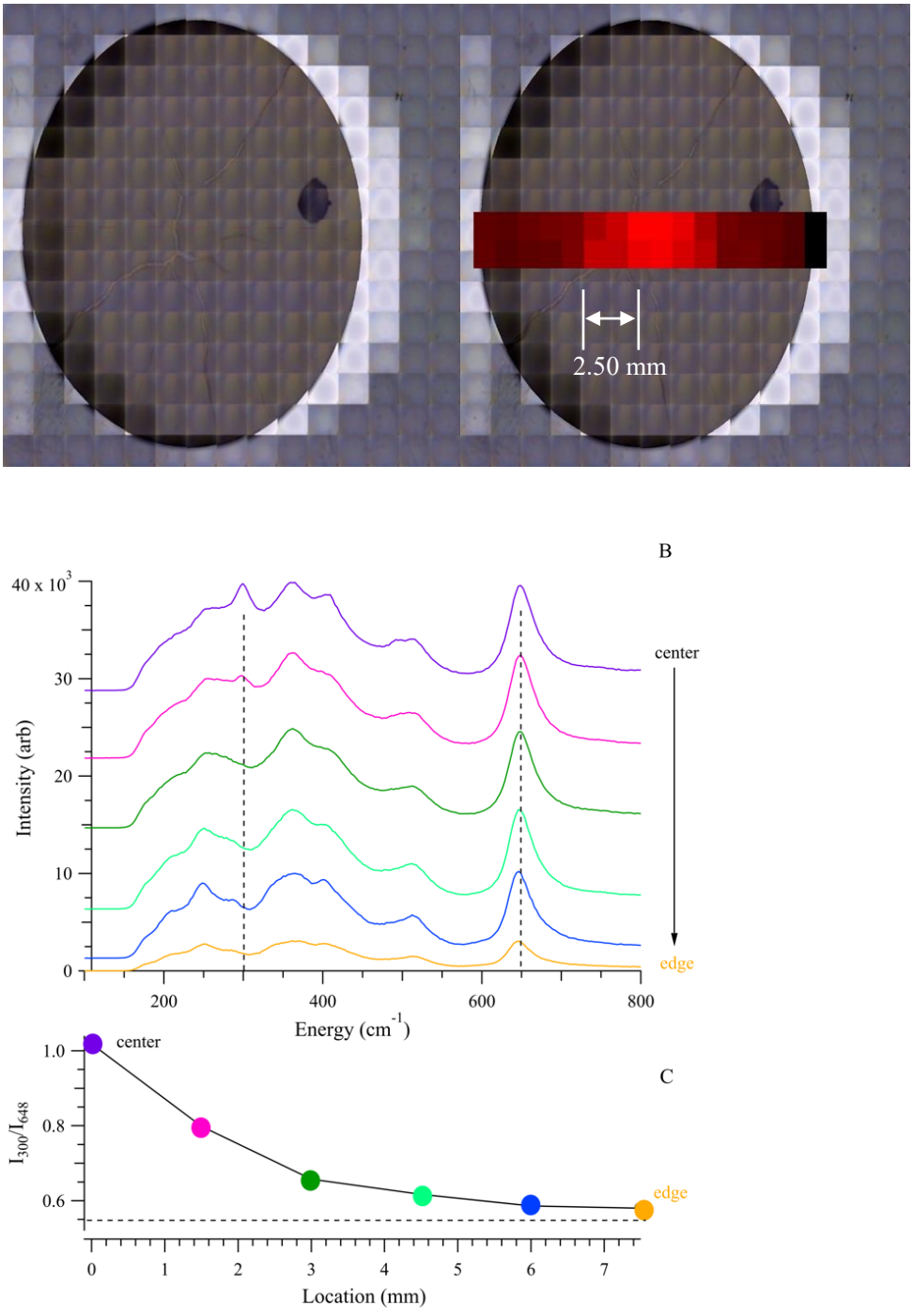

Figure 4. A) Heat map of spatially resolved LZO concentrations across the sintered cubic LLZO sample; B) Raman spectra from different points located on a line between the sample center and edge. C) Intensity ratios showing the intensity at 300 cm^{-1} (LZO) divided by the intensity at 648 cm^{-1} (*c*-LLZO). The horizontal line at 0.55 indicates the ratio corresponding to pure *c*-LLZO.

amount of LZO at its center while *c*-LLZO content at the edges appears unchanged from its pre-sintering composition. Also, we note that while some of the spectra *may* show a hint of a shoulder near 284 cm^{-1} implying possible *t*-LLZO formation, we do not observe a corresponding feature at 593 cm^{-1} that would confirm *t*-LLZO growth. This latter observation coupled with a I_{300}/I_{648} intensity ratio that never drops below 0.55 shows that *t*-LLZO formation was negligible.

A remaining question about *c*-LLZO's phase evolution during thermal processing is whether the changes observed in Figures 4 persist through the bulk of the material. Raman measurements shown in Figure 4 will probe ~100 nm into the material, only a small fraction of the sample's 1.6 mm thickness. To assess if these radially dependent material changes measured in the near surface region extend throughout the entire sample, we broke a sample pellet in half and then measured Raman spectra at approximately 1 mm intervals from the center of the pellet out to the edge as indicated schematically in Figure 5a. Raman spectra from the different points are shown in Figure 5B.

Again, using a ratio of the Raman features assigned to LZO (at 300 cm^{-1}) and LLZO (648 cm^{-1}), we evaluated the extent of LZO formation in the bulk material as a function of position relative to the pellet's center. The spatially dependent ratios (Figure 5C) show clearly that the pellet is defined by a compositional gradient with more LZO in the center and less towards the perimeter. This LLZO-LZO distribution pattern is consistent with what is observed on the pellet's surface. The radial distribution observed in the pellet's cross-section, along with the surface LZO composition, show a consistent LZO concentration normal to the surface throughout the sample's interior.

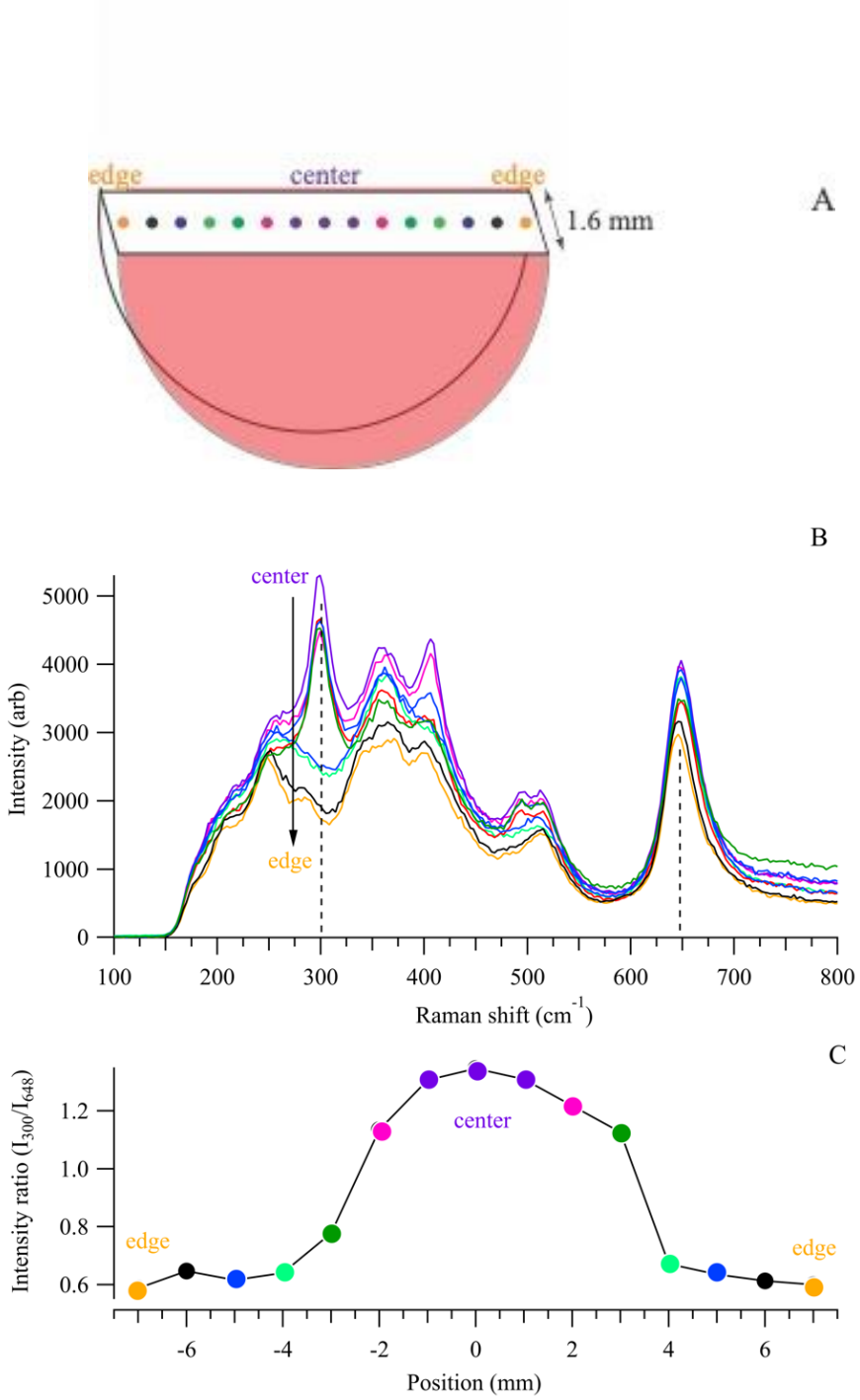

Figure 5. A) Schematic of sample used for cross sectional Raman mapping. Spectra were acquired from the center point between the two edges radially out from the sample center. B) Spectra from the different points along the sample interior. The dashed lines correspond to the LZO band intensity (at 300 cm^{-1}) and the LLZO band intensity (at 648 cm^{-1}). C) A plot of the LZO/LLZO intensity ratio as a function of position. Here, the 0 position is the mid-point between the two perimeter edges indicated in 6A.

XRD measurements support findings from the vibrational Raman studies. Figure 6 shows XRD patterns from LLZO samples arranged in 2 different geometries and the LLZO pattern from *c*-LLZO (bottom). The top pattern (labeled 'Top surface') was acquired from a surface of a single sample, similar to the sampling geometry used for the Raman mapping shown in Figure 4. Following Rietveld refinement, the total calculated material percentages were 97% LLZO and 3% LZO. (Rwp = 17.4%) Efforts to include *t*-LLZO in the fit did not lead to any improvement in the refinement. From this finding, we conclude that any *t*-LLZO that may have formed during sintering was below detection limits, consistent with conclusions from the Raman mapping experiments. Based on the Raman mapping experiments shown in Figure 4, the area showing clear evidence of LZO formation has a radius of ~3 mm or an area of 28 mm^2. This Li^+ depleted region constitutes ~16% of the total surface area. Given that the Raman data in Figure 4 show that the center region contains a mixture of both *c*-LLZO and LZO, the 3% value reported by the XRD pattern is not unreasonable.

The middle pattern ('Cross section') shown in Figure 6 resulted from 4 samples that had been broken in half and then stacked together so that the "surface" being sampled in the XRD experiment consisted of 8 cross sections similar to the sampling geometry used for the Raman cross sectional mapping data shown in Figure 5. At first glance, the two patterns (top and middle) look similar but close inspection shows small differences. Rietveld refinement (Rwp = 27.2%) leads to a calculated composition of 93% LLZO and 7% LZO. Again, assuming that the Li^+ depleted region extends ~3 mm away from the sample center, geometric considerations show that approximately 40% of the total area should contain measurable amounts of LZO. With these

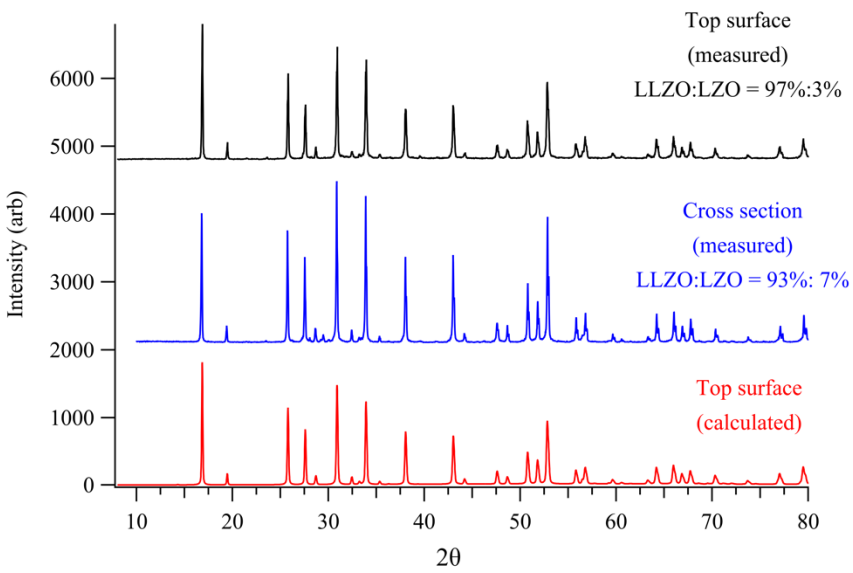

Figure 6. Top: Measured XRD pattern from the surface of a sintered LLZO sample equivalent to the sample geometry used to acquire Raman data in Figure 4. Middle: Measured XRD pattern from 8 stacked LLZO sample cross sections equivalent to the geometry used to acquire Raman data shown in Figure 5. Bottom: Representative calculated XRD pattern of the top sample following Rietveld refinement.

differences in LZO area being sampled in the two different geometries, we expect to observe 2.5 times more LZO in the cross section experiment (40% /16%) compared to the top surface experiment. This estimate agrees with the 2.3 fold excess of LZO measured in the cross section XRD pattern, especially given the rough estimates used to assess the Li^+ depleted regions based on the Raman mapping measurements and uncertainties in area irradiated by the incident X-rays.

Based on the data shown in Figures 4-6, we propose that that Li^+ diffusion through *c*-LLZO is faster than lithium volatilization at 1000˚C. A consequence of this behavior is that as Li is lost from the material at the sample edges, it is replaced rapidly by Li^+ diffusing from the sample's center. In principle fast Li^+ diffusion should maintain a constant concentration gradient across the sample, but the data show clearly that LZO forms at the center of the sample during sintering but not at the edges. We propose that as Li^+ diffuses from the center to the edge, Li^+

depletion in the center drives the formation of LZO *preventing* Li^+ 'back-migration' leading Li^+ to accumulate at the sample edges. We note that our findings complement those reported recently by Zheng and coworkers.[115] In their work, Zheng and coworkers compared different methods for preparing (Ta-stabilized) *c*-LLZO. The authors found that LLZO precursors first formed an LZO intermediate phase that then converted into LLZO. Samples prepared for conductivity measurements were sintered at 1200˚C – higher than the 1000˚C in our work – but that samples were 'covered with the same mother powder' during sintering. Based on our findings presented above, we expect covering the samples in this way limited the amount of Li^+ volatilization and allowed the samples to retain a homogeneous *c*-LLZO composition throughout the sample.

Our proposed mechanism is illustrated schematically in Figure 7. In this figure, the relative Li^+ content along the y axis corresponds to the $Li_{6.25}$ in the original, Al-stabilized material. A Li content of 0 would force the material to revert to LZO an intermediate identified by Zheng and coworkers during LLZO synthesis. The position along the x axis corresponds to the relative position along the diameter with the locations of 0 and 1.0 corresponding to the perimeter edges (at 0 mm and 15 mm) and the center of the sample 0.5 corresponding to the midpoint (7.5 mm) between the two edges.

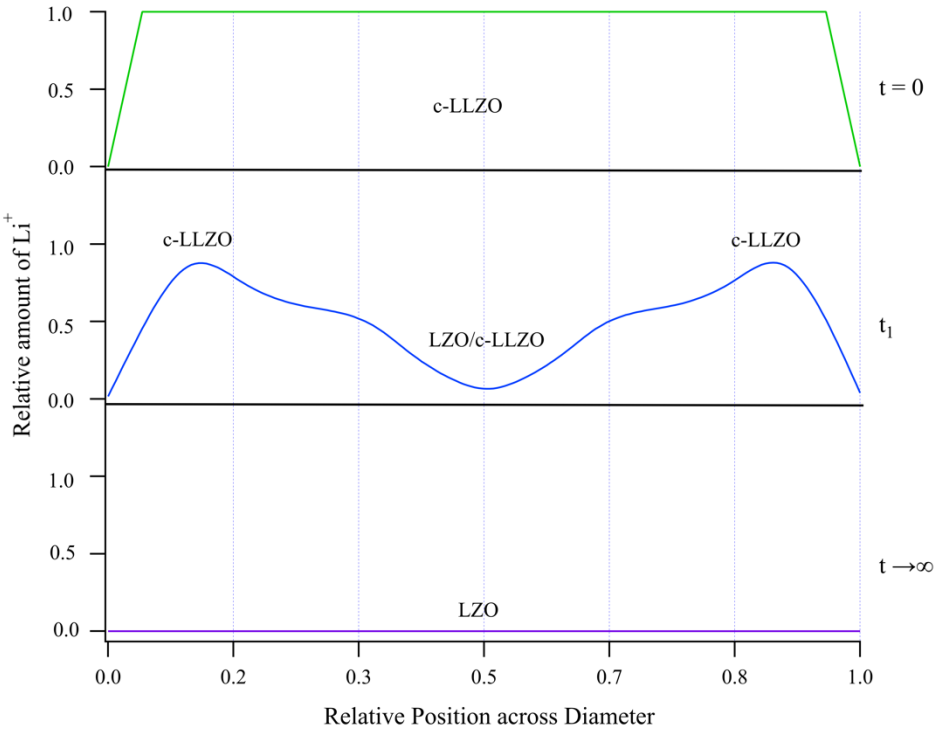

Figure 7. A schematic representation of how the *c*-LLZO material changes during sintering and Li^+ loss through volatilization. The top panel (t= 0) notes a uniform composition across (and throughout) the pellet prior to sintering. The middle panel (t_1) shows an intermediate time during sintering as Li^+ is depleted at the sample center and LZO begins to form. The bottom panel shows the eventual complete conversion to LZO if the sample were left at high temperatures and all the Li^+ volatilized.

This mechanism leads to irreversible loss of Li^+ in the middle of the material and the irreversible formation of LZO. Furthermore, the data in Figure 6 shows clearly that this effect extends throughout the entire sample interior. The effects of Li^+ migration coupled with LZO formation are illustrated schematically in Figure 7 where at time t = 0 before sintering, the sample consists of *c*-LLZO with a uniform Li^+ distribution throughout the sample. As the sample is heated Li^+ diffusion to the sample edges to replace volatilized Li_2O coupled with LZO formation at the sample center leads to the heterogeneous distribution of materials observed in

the final product. In the long-time limit, we expect that most, if not all, Li^+ would be lost and the sample would revert to a homogeneous LZO pyrochlore material.

Summary

Experiments described in this work characterize material heterogeneity that develops in a *c*-LLZO sample during sintering. A combination of spatially resolved Raman vibrational spectra together with complementary XRD measurements shows that a LZO concentration gradient develops after the sample has been heated at 1000˚C for one hour, with more LZO in the sample's center and non-observable amounts of LZO at the sample edges. LZO formation in *c*-LLZO is associated with Li^+ loss through volatilization. These experiments were designed so that Li^+ loss opportunities were limited to the 1.6 mm thick perimeter of the 15 mm diameter sample. This experimental geometry together coupled with our findings suggest a mechanism describing LZO formation and the relative stability of *c*-LLZO during sintering. Specifically, these results require that Li^+ diffusion within the sample be fast relative to Li^+ volatilization (presumably as Li_2O) *and* that Li^+ depletion in the sample center promotes LZO formation making the loss of Li^+ at the sample center irreversible. The data did not show any evidence of a second LLZO polymorph, *t*-LLZO, forming during the sintering process Our conclusions have consequences for strategies intended to use LLZO as an electrolyte in ASSBs. Specifically, once LZO begins to form anywhere within a sample, that region is likely to become irreversibly electrochemically inactive. Furthermore, LZO will form relatively quickly in regions that become Li^+ depleted. This proposed model now allows materials scientists and engineers to design sintering methods and processes that minimize LZO formation and preserve *c*-LLZO homogeneity throughout samples.

CHAPTER THREE

Dopant Effects on the Thermal Stability of Li^+ Conducting cubic-$Li_7La_3Zr_2O_{12}$

Contribution of Authors and Co-Authors

Manuscript in Chapter 3

Author: Steven Thomas Montoya

Contributions: Collected and analyzed all data, generated figures and wrote manuscript in preparation for publication.

Co-Author: Shah Ali Haider Shanto

Contributions: Made pellets, measured replicated data.

Co-Author: Robert A. Walker

Contributions: Assisted in planning experimental studies and interpreting results. Edited and assisted in preparation of the manuscript.

Manuscript Information

Steven T. Montoya, Shah A. H. Shanto, Robert A. Walker

Status of Manuscript:
☐ Prepared for submission to a peer-reviewed journal
☒ Officially submitted to a peer-reviewed journal
☐ Accepted by a peer-reviewed journal
☐ Published in a peer-reviewed journal

DOPANT EFFECTS ON THE THERMAL STABILITY OF Li^+ CONDUCTING CUBIC-$Li_7La_3Zr_2O_{12}$

Steven T. Montoya[1], Shah Ali Haider Shanto[2], and Robert A. Walker[1,2]*

[1]Department of Chemistry and Biochemistry, Montana State University, Bozeman, Montana, 59717 USA

[2]Montana Materials Science and Engineering Program, Montana State University, Bozeman, Montana, 59717 USA

[*]corresponding author

Abstract. Raman microscopy, thermal gravimetric analysis, and X-ray diffractometry were used to quantify how the thermal stability of $Li_7La_3Zr_2O_{12}$ (LLZO) changes with dopants used to stabilize the LLZO's cubic phase (*c*-LLZO). LLZO's thermodynamically stable phase at room temperature and 1 atmosphere is tetragonal (*t*-LLZO), a material with very low lithium-ion conductivity. Dopants such as Al, Nb, and Ta are commonly used to stabilize *c*-LLZO under ambient conditions and raise *c*-LLZO's lithium-ion conductivity by more than an order of magnitude. As a dopant, Al^{3+} substitutes into Li^+ sites creating 3 Li^+ vacancies while Ta^{5+} and Nb^{5+} substitute for Zr^{4+} creating a single Li^+ vacancy. Raman data show that upon heating to 1000˚C in air, *c*-LLZO decomposes to form an ion-insulating pyrochlore phase, $La_2Zr_2O_7$ (LZO). Ta-doped and Nb-doped *c*-LLZO form ~5-10 times more LZO than Al-doped *c*-LLZO, based on both vibrational Raman spectra and X-ray diffraction patterns. Ta-doped and Nb-doped *c*-LLZO also form La_2O_3 as an additional secondary phase implying close to quantitative loss of lithium in some parts of the sample. These results are consistent with TGA data that show Ta-doped and

Nb-doped *c*-LLZO samples losing >20% of their mass while Al-doped *c*-LLZO loses < 15% of its mass when heated above 800˚C. Taken together, these findings can be used to inform strategies used to process *c*-LLZO for use as solid-state lithium-ion battery electrolytes.

Introduction

Battery power represents an increasingly important contribution to energy systems worldwide. Growth in markets such as commercial electric vehicles are driving the demand for lighter batteries having higher energy densities.[95] While the materials research community is actively investigating new battery technologies including sodium ion and potassium ion batteries, lithium ion batteries remain the single-most commercially viable battery available for use.[116, 117, 16] Lithium ion batteries have energy densities as high as 360 Wh/kg, and state-of-the-art redox flow batteries have life spans of up to 15,000 cycles.[118, 119] Furthermore, lithium ion batteries are ubiquitous in most consumer electronics due to being lightweight and flexible, with energy densities of 200 Wh/kg or more, life spans of 3000 cycles and high efficiencies up to 95%.[119] Between the years 2022 and 2030, lithium ion battery manufacturing capacity is expected to increase ≥ 4-fold to almost 7 TW-hours, due in large part to the proliferation of electric vehicles.[120]

Despite these attractive metrics, lithium-ion batteries suffer from several important limitations. Liquid electrolyte-based batteries often experience dendrite growth during charge/discharge cycles as well as during fast charging regimens. Dendrite growth can short circuit a battery, igniting battery components and causing catastrophic damage.[121] To prevent such failures, secondary materials that limit dendrite growth have been added to electrodes and electrolytes and traditional separators have been treated with ceramic coatings that suppress

dendrite growth.[122] An alternate approach has focused on the developing lithium-ion conducting solid-state materials that can serve as nonflammable electrolytes in all solid-state batteries (SSBs).[60] These materials include Li_3PO_4 (LISICON), perovskite materials including $BaZrO_3$ and $CaTiO_3$, and garnet-structured materials including $Li_7La_3Zr_2O_{12}$ (LLZO).[61] Solid state electrolytes are more mechanically resistant to dendrite formation and offer the promise of lighter devices having higher energy storage capacity than current batteries using liquid electrolytes.[123]

Of these Li^+ ion conducting materials, LLZO is particularly attractive. In its cubic form (*c*-LLZO), this material has ion conductivities as high as 1 mS/cm, high thermal stabilities under operational conditions, and a wide electrochemical window.[69, 93] However, to form a dense material suitable for electrolyte applications, LLZO must be sintered at temperatures approaching 1200 °C.[124, 125] At these temperatures, Li^+ will react with oxygen in the crystal lattice forming Li_2O that can volatilize from the material.[126] Loss of Li^+ results in the formation of a lanthanum-zirconium pyrochlore phase, $La_2Zr_2O_7$ (LZO), a lithium-ion conduction insulator.[97] Most literature accounts, however, support the idea that when formed as a secondary phase during LLZO sintering, LZO limits material conductivity.[114, 126, 127, 128, 129, 130]

Findings reported in this work examine the how different dopants used to stabilize LLZO's cubic phase affect *c*-LLZO's thermal stability. A recent report suggests that LZO formed from aluminum doped LLZO decomposition forms a distinctive diffusion gradient during high temperature sintering.[71] Three types of dopants are examined: aluminum substituting for lithium and both tantalum and niobium substituting for zirconium. Aluminum is an aliovalent and non-mobile substitute that replaces three lithium ions in the crystal lattice.[131] The zirconium

substitutes – Ta and Nb – occupy a zirconium site and displace one lithium enabling lithium ion conductivity.[75, 108 132] Different doping strategies raise the question of whether Li volatilization mechanisms and the resulting material degradation observed for Al-doped, *c*-LLZO is universal for other *c*-LLZO materials. To address this question, Raman spectroscopy, X-ray diffraction (XRD) and thermogravimetric analysis (TGA) are employed to study dopant effects during and post- sintering.

Experimental Methods

Sample processing. Samples were prepared using Al ($Li_{6.25}Al_{.25}La_3Zr_2O_{12}$), Nb ($Li_{6.5}La_3Zr_{1.5}Nb_{0.5}O_{12}$), and Ta ($Li_{6.5}La_3Zr_{1.5}Ta_{0.5}O_{12}$) doped c-LLZO powder (manufactured by Ampera) using methods previously reported.[71] Materials were tested for purity using Raman and XRD prior to processing. Raman spectra from all three materials showed no evidence of secondary phases present. XRD patterns reported ≤3% LZO content in Ta-doped *c*-LLZO and ≤0.5% LZO in both Al-doped and Nb-doped *c*-LLZO. Powder *c*-LLZO samples were mixed with equal amounts of a binder/ethanol mixture and then pressed in 15 mm diameter die for 10 seconds at 495 MPa. Sintering times were 1 hr and 12 hrs at 1000℃. During sintering the samples were covered on their top and bottom surfaces with Al_2O_3 plates. (Figure 1)

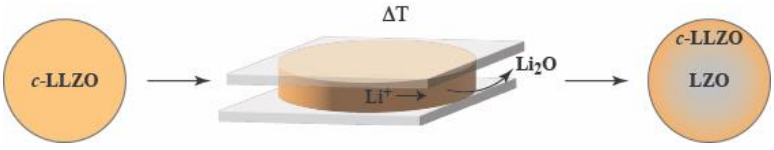

Figure 1. Schematic showing the experimental assembly using two alumina plates to cover the top and bottom of *c*-LLZO pellets sintered for 1 and 12 hours. In this configuration, Li+ could only volatilize from the pellet perimeter. Typical pellets measured 15 mm in diameter with a 1.2-1.5 mm thickness.

These plates constrained the pathway available for lithium volatilization to the 1.5 mm thick sample pellet perimeter. Previous work has shown that under these circumstances, Al-doped *c*-LLZO develops unusual degradation pattern with LZO forming at the center of the sample but not at the edges.[71]

Characterization – Raman spectroscopy. Raman spectra were acquired using a Renishaw InVia Microscope with a 488 nm single line argon laser (488 nm). Wire 5 software was employed to capture mapping measurements of each sample in a circular scan rastering from left to right and then from top to bottom. Each spectrum was measured with 5 mW of incident power and a 6 second acquisition time. Spectra locations were approximately 1 mm apart. False color 'heat maps' were generated using the analysis function in Renishaw's Wire 5 software.

Raman analysis will focus on three specific materials: *c*-LLZO and two degradation products, LZO and La_2O_3. While the low-frequency phonon spectrum of *c*-LLZO is congested, these three materials are distinguished by distinct and unique features. *c*-LLZO is marked by a strong vibrational band that appears between 635 and 650 cm^{-1} assigned to the symmetric stretching motion of ZrO_6 octahedra.[85, 100] We note that the Ta and Nb-doped samples show a second, higher frequency feature ~718-730 cm^{-1} that arises from MO_6 vibrations (M = Ta or Nb). The degradation products, LZO and La_2O_3 have vibrational features at 300 cm^{-1} and 940 cm^{-1}, respectively.[88] These features are diagnostic of *c*-LLZO that has lost lithium and begun forming secondary phases.

An important point to note is that Raman spectroscopy is extremely useful at identifying materials and *relative* changes in material abundance. Raman spectroscopy is not well suited to quantitative analysis, especially for heterogeneous solid samples, given differences in Raman

scattering cross sections, particulate size, and potential optical polarization related effects.[133] To assess how the relative abundance of these three materials – *c*-LLZO, LZO and La_2O_3 – are reflected in Raman vibrational band intensities, a control sample containing equal amounts of each (by mass) was measured. (Appendix, Figure AP-1). In this mixture, the molar amounts of the three materials are 18.8% *c*-LLZO: 32.8% LZO: 48.4% La_2O_3. Even after considering the stoichiometric differences, data show that LZO and La_2O_3 have stronger Raman scattering cross sections than *c*-LLZO.

Characterization – XRD. XRD patterns were acquired using a 1kW Bruker D8 Advance X-ray diffractometer rotational stage and processed using MDI Jade peak matching software. Each pellet sample was placed on top of clay in a deep-seated sample holder and pressed down until sample was flush with sample holder edges. Samples were scanned from 5 to 80 2θ in 0.05˚ increments with 0.2 second acquisitions per step. Jade peak matching software and Rietveld refinement were used to calculate material percentages and elemental analysis.

The relative intensities of different XRD peaks are used to calculate the mass percent of the sample's material makeup. This calculation can be impacted by multiple factors such as peak overlap between materials and feature intensity ratios. (As a control experiment, an XRD pattern was acquired from a composite material containing equal amounts (by mass) of c-LLZO, LZO, and La_2O_3. This pattern and the resulting mass analysis are reported in the Appendix (AP Figure 2 and show that XRD quantitation can be limited in its accuracy.) At low La_2O_3 concentrations, Rietveld refinement calculations overlap with scattering features from both *c*-LLZO and LZO. Due to this overlap, the software did not include La_2O_3 in % composition calculations due to uncertainty of La_2O_3's relatively low concentrations.

Characterization – TGA. TGA data were acquired using a TA Discovery TGA 5500. Pellets were prepared the same methods as reported above, but prior to sintering pellets were split into pieces that were then used for the TGA measurements. Each sample was subjected to 10 ℃/min ramp rate to 900℃ where it remained for for 1-3 hrs. Samples were subjected to air during TGA, flowing at 10 mL/min flow rate. Differential thermal analysis is calculated using central difference methods to determine derivatives for each data point.

Results

Optimizing processing conditions so that LLZO can be used as a solid-state electrolyte requires knowing not only the material's phase stability but also how elevated temperature, atmosphere composition, and external pressure affect material reactivity and volatility. Given the geometry shown in Figure 1, heating Al-doped LLZO to 1000˚C results in lithium loss (presumably as Li_2O) through volatilization at exposed edges, and the remaining material forms LZO as a lithium-depleted secondary phase.[71] The characteristic spatial distribution formed by LZO at the sample's center (e.g. Figure 1) implies that as lithium is lost from the perimeter, it is replaced by lithium rapidly diffusing from the middle of the sample. Lithium depletion from the sample center drives LZO formation. The *c*-LLZO → LZO change is irreversible at these temperatures, preventing lithium-ion back-diffusion into the affected areas. At the temperatures used in these studies, aluminum is an immobile, lithium-site dopant, replacing 3 lithium ions and creating a $Li_{6.25}Al_{0.25}La_3Zr_2O_{12}$ stoichiometry.[77] The dopants tantalum and niobium are also immobile and stabilize *c*-LLZO by substituting for zirconium (and one lithium) to form $Li_{6.50}La_3Zr_{2-x}M_xO_{12}$ where M = Ta or Nb and x = 0.5. Results below show that these materials

doped for Zr are thermally less stable than Al-doped *c*-LLZO and form more LZO when sintered at temperatures appropriate for fabricating solid electrolytes.

Figure 2 shows Raman spectra from all three LLZO samples – Al-doped, Ta-doped, and Nb-doped – after sintering in air at 1000˚C for one hour. Spectra were acquired from the center of each 15 mm diameter sample and the edge of the sample as indicated in the inset. *c*-LLZO and LZO spectra have been assigned previously.[85, 89, 98, 100] As noted in the previous section, the vibrational feature with a center frequency between 635 cm^{-1} and 652 cm^{-1} is assigned to vibrational motion of the octahedral ZrO_6 units while the 300 cm^{-1} vibrational band arises from LZO's O-Zr-O bending vibration having E_{2g} symmetry.[88] In Ta-doped and Nb-doped *c*-LLZO, the metal dopant gives rise to a second band at 718 cm^{-1} (Ta-doped) and 730 cm^{-1} (Nb-doped) also assigned to symmetric stretching of MO_6 octahedra (M = Ta or Nb).[100] Al-doped *c*-LLZO does not show this feature as Al substitutes for lithium and not zirconium. Spectra in Figure 2 all show clear signs of LZO formation at the sample centers and an absence of LZO at the sample edges. The Ta-doped and Nb-doped samples also show strong signal at 935 cm^{-1} at the sample centers indicating additional *c*-LLZO decomposition.

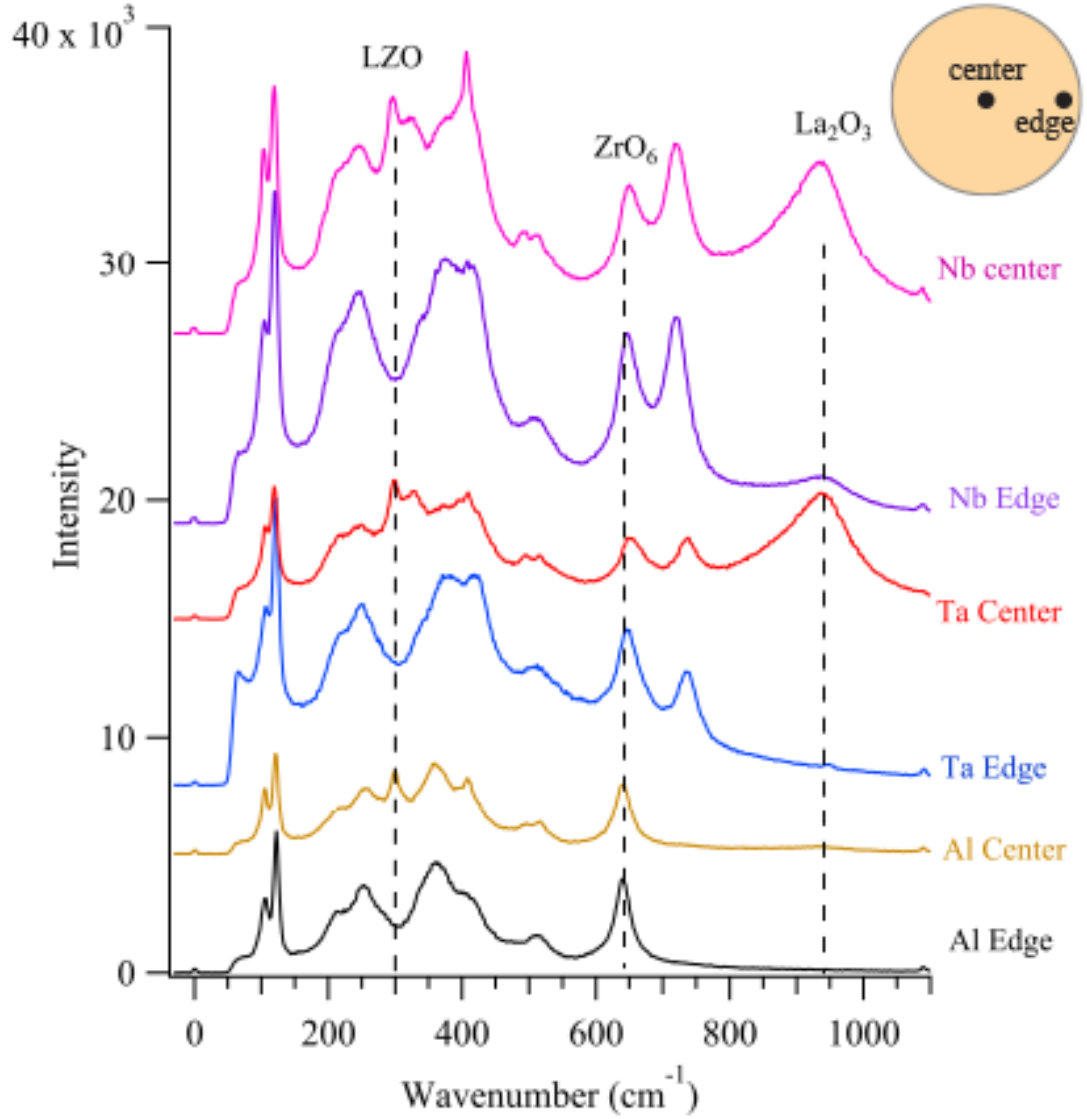

Figure 2. Raman spectra for 3 dopants of c-LLZO (Ta, Nb, and Al) measured at the center and edge of sample pellets after each sample has been sintered for 1 hour. The diagram shows schematically where spectra were measured. Edge spectra were typically acquired within ~1 mm of each sample's perimeter.

Prior work describing Al-doped *c*-LLZO's thermal stability used a ratio of LZO and LLZO Raman band intensities (at 300 cm^{-1} and 650 cm^{-1}, respectively) as a relative metric of thermal decomposition and reported that the I_{300}/I_{650} ratio varied between 0.6 (no LZO at edge) and 1.2 (measurable amounts of LZO at center).[71] Data shown in Figure 2 have ratios of 0.5 at

the Al doped LLZO edge and 1.2 at the material's center, consistent with that previous report. For the Ta and Nb-doped samples, the ratios are 0.8 (Ta) and 0.7 (Nb) at the sample edges indicating little – if any – LZO. The I_{300}/I_{650} ratio for Zr site dopants (Ta and Nb) is higher due to the intrinsically weaker 650 cm^{-1} intensity resulting from Ta/Nb substituting for Zr in a 1:3 ratio. At the sample centers, I_{300}/I_{650} ratios are 1.7 (Ta) and 1.6 (Nb) implying substantial lithium depletion and considerable LZO formation.

Table 1. Vibrational frequencies used to distinguish the three relevant materials (*c*-LLZO, LZO and La_2O_3) from each other.

Material	Energy (cm^{-1})	Vibration
c-LLZO	645-650	ZrO_6
c-LLZO (Ta or Nb = M)	718 and 735	MO_6
La_2O_3	940	O-La-O stretch
LZO	300	O-Zr-O bend

Thermogravimetric analysis was used to further evaluate the thermal stabilities of Al-doped, Ta-doped, and Nb-doped *c*-LLZO. Figure 3a shows the mass percent loss vs. time (in minutes) for the three *c*-LLZO dopants as the sample temperature was raised from 25 to 900 ℃ at a rate of 10℃/min. Samples were held at 900 ℃. All 3 samples – Al-doped, Ta-doped, and Nb-doped *c*-LLZO – showed terminal mass loss by ~90 minutes. Overall, Ta-doped and Nb-doped *c*-LLZO had the most mass loss, losing 23% and 20% of the total sample mass, respectively. In contrast, Al-doped *c*-LLZO lost only 14% of its total mass. These results support the Raman data in Figure 2. Assuming that mass loss is due primarily to Li_2O volatilization, Ta-doped and Nb-

doped LLZO lose more Li_2O than Al-doped LLZO and are expected to form more LZO. In the case of the Zr-substituted materials, thermal degradation does not stop with LZO formation but rather continues to form La_2O_3.

Data in Figure 3a contain more information than simply total mass loss. Data for all three samples show that mass loss is not monotonic but instead proceeds in a stepwise fashion. Figure 3b shows the time derivative of each trace in Figure 3a plotted as a function of time. Each inflection point in a TGA trace appears as a maximum in this differential thermal analysis (DTA). These inflection points correspond to times (and temperatures) when a sample's mass loss is most rapid. The times of these inflection points (and the corresponding temperatures) are listed in Table 2.

Common to all samples is mass loss at early times (< 10 min) and low temperatures (<110˚C). We assign this feature to loss of the organic additives used during sample pressing. (All samples have approximately equivalent amounts of organic additives.) After this first mass loss event, differences emerge between the Zr-substituted *c*-LLZO samples and the Li-substituted *c*-LLZO sample. The Zr-substituted Ta-doped and Nb-doped samples show four additional mass loss events labeled in Figure 3b as Zr-a1, Zr-a2, Zr-b, and Zr-c. The dominant mass loss feature is Zr-c, occurring at the latest times and highest temperatures. Based on prior reports, we attribute this feature to loss of Li_2O and decomposition of LLZO into LZO.[134] Notably, feature Zr-c occurs sooner (75.1 min) and at a lower temperature (766˚C) for Nb-doped *c*-LLZO than for Ta-doped *c*-LLZO (86.6 min, 877˚C) again indicating that of the two materials having dopants substituting for Zr, the Nb-doped *c*-LLZO is less stable than Ta-doped *c*-LLZO.

The earlier time features in the Zr-substituted samples are attributed to lower temperature decomposition of LiOH from a Li_2CO_3/LiOH passivation film believed to result from the reaction of organic binders and excess Li_2CO_3 with the *c*-LLZO.[114, 135] A final observation about the mass loss derivative traces for Ta-doped and Nb-doped *c*-LLZO is that the features in the Nb-doped sample are much broader than for the Ta-doped sample. This finding suggests that lithium mobility and material stability in the Nb-doped sample is more heterogeneous compared to the Ta-doped sample where thermal degradation proceeds in well-defined steps and implies material homogeneity.

The Li-substituted, Al-doped *c*-LLZO also shows late-time, high temperature mass-loss, but the mass loss is characterized by two inflection points (at 80.0 and 86.7 min) and the magnitudes of these features are considerably smaller than those observed in the Zr-substituted samples. This behavior could be due to formation of $LiAlO_2$ that has been reported to form on the surface of LLZO grains and hinder lithium ion loss.[126, 136] Whereas the Zr-substituted samples have a small, well-defined inflection point near 56 min (~575 ˚C), the Li-substituted Al-doped sample shows almost continuous mass loss between 425˚C and 725˚C with the data in Figure 3b characterized by broad, poorly-defined features. This mass loss is attributed to decomposition of Li_2CO_3 and LiOH that is known occur between 425 ˚C (LiOH) and 730 ˚C (Li_2CO_3).[114] Li_2CO_3 that is not a part of a passivation layer typically decomposes at ~540 ˚C.

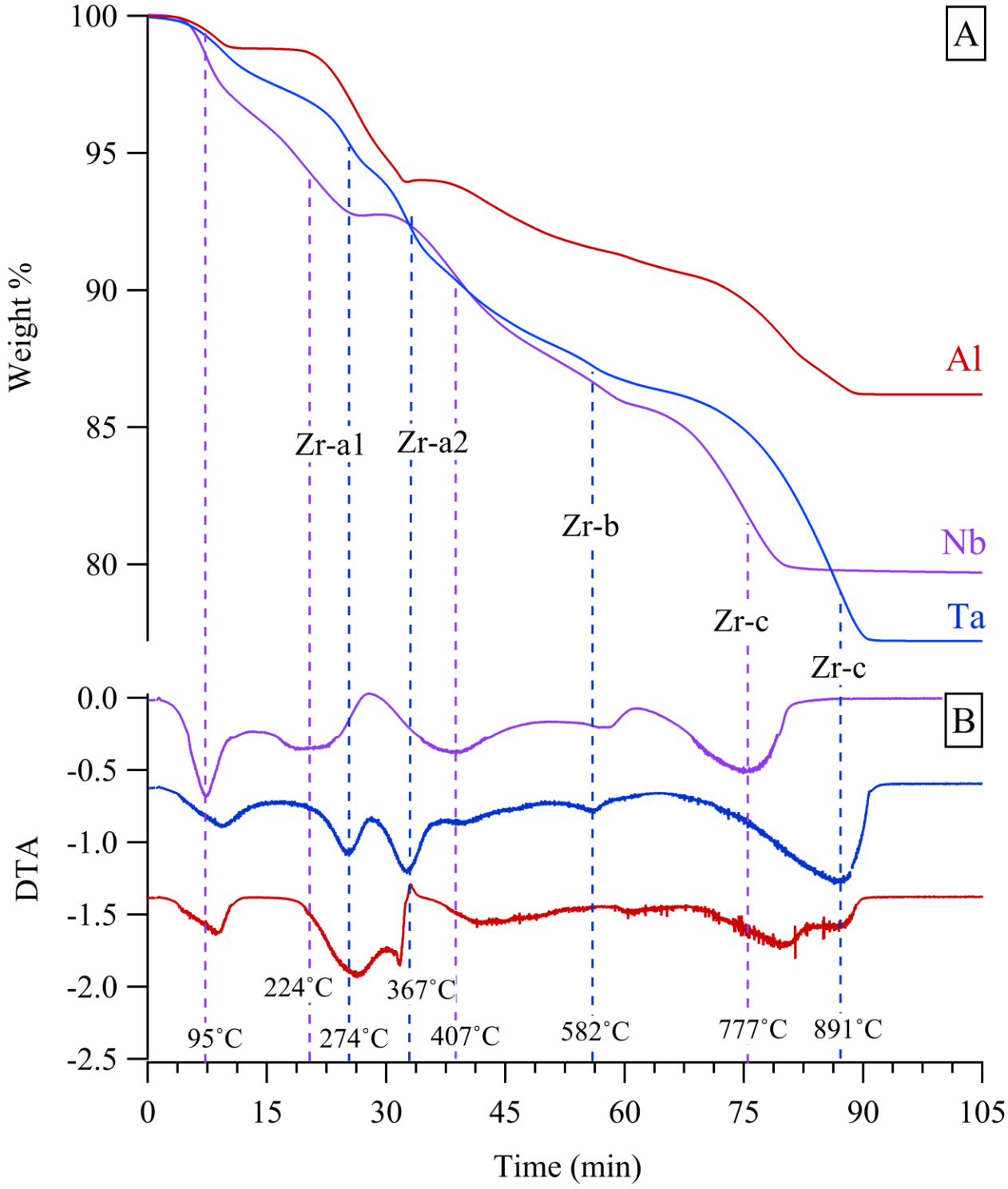

Figure 3a. Thermogravimetric analysis of Al, Ta, Nb plotted time vs derivative mass percent. **3b**. Derivative plot for TGA of Al, Ta, and Nb plotted time vs $d[weight\%]/dt$.

Table 2. Time and temperatures of the DTA minima shown in Figure 3B. Times are in minutes, temperatures are in ˚C. The asterisk for Al-doped c-LLZO at 31.5 min/340˚C notes the derivative-type line shape shown in Figure 3B.

Dopant							
Ta	Time	9.4	25.0 (sharp)	32.3 (sharp)	55.5 (sharp)	86.6	
	Temp	119	275	348	580	891	
Nb	Time	7.0	20.0 (broad)	38.4 (broad)	57.1 (sharp)	75.1	
	Temp	95	225	409	596	776	
Al	Time	9.2	26.1	31.5*	42.8/60.6	79.9	86.7
	Temp	117	286	340	453/631	824	892

The TGA data show that Al-doped *c*-LLZO is more thermally stable than either Ta-doped or Nb-doped *c*-LLZO. These findings, however, do not show whether the secondary materials formed from *c*-LLZO thermal degradation are distributed uniformly across the sample or if the secondary phases are patchier. Resolving this question is an important step towards understanding *c*-LLZO thermal decomposition mechanisms. If LZO (and La_2O_3) forms symmetrically within the *c*-LLZO sample, then we conclude that lithium-ion diffusion is fast, and degradation happens uniformly. If, however, degradation products appear distributed randomly across the surface, then we must conclude that secondary phase formation nucleates stochastically throughout the material leading to lithium rich (*c*-LLZO) and lithium poor regions.

To better understand LZO distribution across the different *c*-LLZO materials, spectroscopic mapping was used to spatially resolve compositional variation after sintering. In these mapping experiments, spectra were acquired from each sample using an array of ~185 spots. After spectra were acquired, each was analyzed in terms of its I_{300}/I_{650} ratio. In spectra where the ratio exceeded the ratio from a pure LLZO baseline, the site was marked as containing LZO. The relative intensity of the LZO was then highlighted using a false-color heat map.

Figure 4 shows 6 images including Ta-doped (top row), Nb-doped (middle row), and Al-doped (bottom row) *c*-LLZO sintered pellets. The first and second columns show mapping results for samples that were sintered for 1 hour and 12 hours, respectively. Superimposed on each pellet is the array of locations where Raman spectra were measured. The spots are marked with a false-color scale denoting the relative amount of LZO present as evidenced by the I_{300}/I_{650} intensity ratios. A black spot denotes pure LLZO with the only intensity at 300 cm^{-1} resulting from the underlying LLZO phonon structure. If intensity at 300 cm^{-1} rises above the LLZO baseline, spots are marked red, with brighter reds having a higher LZO intensity at 300 cm^{-1} and dimmer spots having lower intensities at 300 cm^{-1} (but still above the c-LLZO phonon baseline).

Several results stand out: first, the Ta-doped *c*-LLZO, 1-hour sintered sample has a heterogeneous LZO distribution implying that lithium-ion loss was anisotropic during the initial sintering stages. Second, after sintering for 12 hours, the Ta-doped sample shows LZO across the entire surface. Third, the Nb-doped sample shows extensive LZO formation after only 1 hour of sintering and results change very little for the 12-hour sintered sample. This result supports data shown earlier that Nb-doped *c*-LLZO is less thermally stable than Ta-doped *c*-LLZO. Fourth, the distribution of LZO in Al-doped c-LLZO is homogenous and tightly localized around the pellet's center. Fifth, relative to the 1-hour sintered sample, the LZO distribution expands in the 12-hour sintered Al-doped sample, but LZO is still not universally observed across the sample's entire surface. These results are summarized in Table 2.

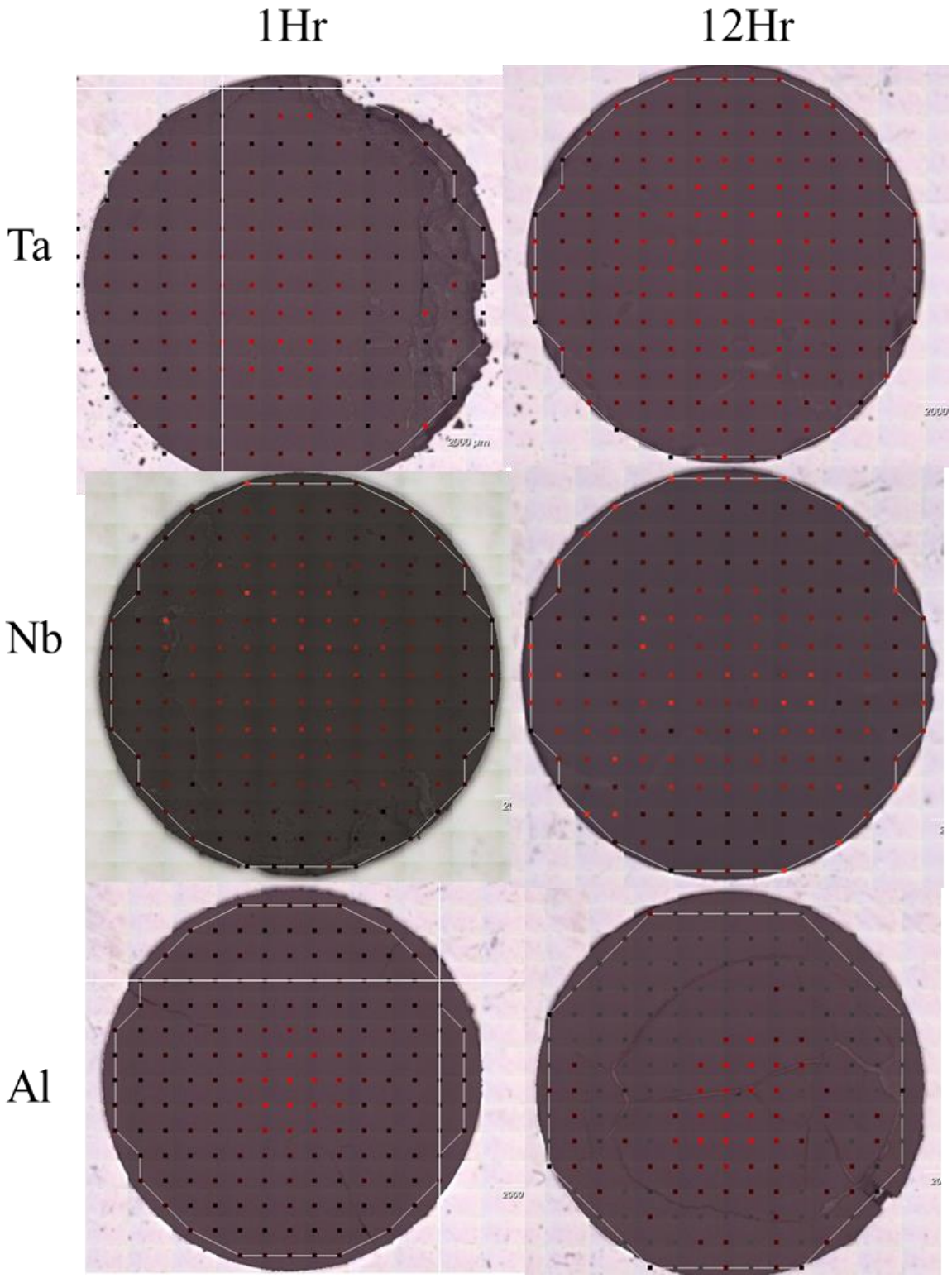

Figure 4. Raman maps for Ta, Nb, and Al doped pellets sintered for 1 hr on the left and 12 hrs on the right.

These results show that thermal degradation of Al-doped *c*-LLZO is self-limiting. This behavior leads to a radially symmetric gradient in LZO consistent with prior reports. In contrast, LZO in Ta and Nb-doped samples – where the dopant substitutes for Zr in LLZO – is uneven after 1 hour of sintering and is distributed broadly across each sample's surfaces with continued heating. Interestingly, Nb-doped LLZO forms most of its LZO within one hour of heating at 1000˚C and additional heating leads to no further significant changes. Ta-doped LLZO on the other hand appears to lose lithium more gradually, but after sintering for 12 hours both materials show LZO across the entire sample.

Table 3. Percentage of spectra showing LZO in mapping experiments (Figure 3) after sintering for 1 hour and 12 hours. The numbers in parentheses report the exact number of spectra showing evidence of LZO divided by the total number of spectra in a given mapping experiment. Uncertainties in these percentages are ±5%.

Dopant	1-hour sinter	12-hour sinter
Al	14% (24/178)	35% (64/185)
Ta	49% (86/177)	95% (169/177)
Nb	90% (160/177)	84% (149/177)

Following our approach in earlier work,[71] Raman spectra were taken at 1 mm intervals radially across each pellet specifically to monitor the *relative amount* of LZO that formed after sintering. Representative data from Ta-doped and Al-doped *c*-LLZO sintered for 1- and 12-hours are shown in Figure 5. (Equivalent data for Nb-doped *c*-LLZO are shown in Appendix AP 3.) Assignments for selected vibrational bands are reported in Table 1. As in Figure 2, we draw attention to three specific features: 1) the LZO vibration centered at 300 cm^{-1} corresponding to O – Zr – O bending mode; 2) the two features at 645 cm^{-1} and 735 cm^{-1} assigned to symmetric

vibrations of the MO_6 octahedra; and 3) the high frequency feature at 935 cm^{-1} assigned to La_2O_3. In the analysis below, the I_{300}/I_{650} intensity ratio is again used as a measure of the relative amount of *c*-LLZO degradation. An additional indicator of degradation is the appearance of La_2O_3 as evidenced by the strong vibrational band at 935 cm^{-1}.

Figure 5a shows spectra from 1-hour sintered Ta-doped *c*-LLZO measured at 1 mm intervals starting at the sample center and ending at the sample edge. The spectra are displaced vertically for clarity with the top spectrum measured at the sample center and the bottom spectrum measured at the sample edge. The spectrum from the sample center shows strong, discernible features from all three different materials: LZO (300 cm^{-1}), *c*-LLZO (650 cm^{-1}), and La_2O_3 (935 cm^{-1}). La_2O_3 is observed clearly up to 2 mm away from the sample center. LZO is evident in spectra up to 4 mm away from the sample center.

Similar spectra acquired from a 12-hour sintered Ta-doped *c*-LLZO sample are shown in Figure 5b. The La_2O_3 signature is more pronounced close to the center than in the 1-hour sintered sample and LZO is evident in all spectra. These results are consistent with the Raman mapping data in Figure 4 showing that >90% of all spectra from across the surface of the 12-hour sintered, Ta-doped *c*-LLZO contain some amount of LZO, but the data in Figure 5 show that the center of the 12-hour sintered sample contains modestly more LZO than the edge.

The Al-doped *c*-LLZO samples behave differently. The 1-hour sintered sample (Figure 5c) shows the expected LZO gradient originating at the sample center and diminishing at ~1-2 mm. The 12-hour sintered sample (Figure 5d) shows even more LZO formed at the sample center (as evidenced by a larger I_{300}/I_{650} ratio), but the extent of LZO formation remains tightly constrained with no detectable LZO near the sample's perimeter. Curiously, the Al-doped LLZO

shows very little La_2O_3 formation even after sintering for 12 hours. Taken together, data from the Zr-substituted and Li-substituted samples show clearly that the Al-doped *c*-LLZO is more resistant to thermal degradation than the Ta-doped and Nb-doped *c*-LLZO.

These data are summarized in Figure 6. Plotting the I_{300}/I_{650} ratios as a function of location across the sample diameter, Figure 6a shows that LZO in the Zr-substituted *c*-LLZO samples is broadly distributed after both 1-hour 12-hours of sintering. The total amount of LZO has increased but the distribution remains largely unchanged. In contrast, the amount of LZO formed in the Al-doped *c*-LLZO sample increases dramatically with increased sintering time but the LZO formation remains localized near the sample center. In Figure 6b integrated intensities of the La_2O_3 vibrational band as a function of position are plotted as a function of distance from the sample center for the Ta-doped *c*-LLZO samples. La_2O_3 is present at the sample center after 1 hour of sintering, but the vibrational intensity increases dramatically after 12 hours at 900˚C. Figure 6c shows a ratio of the LZO and La_2O_3 band intensities for the Ta-doped *c*-LLZO. Interestingly, this ratio changes little as a function of sintering time and suggests that La_2O_3 formation is self-limiting to the sample center where lithium loss is greatest.

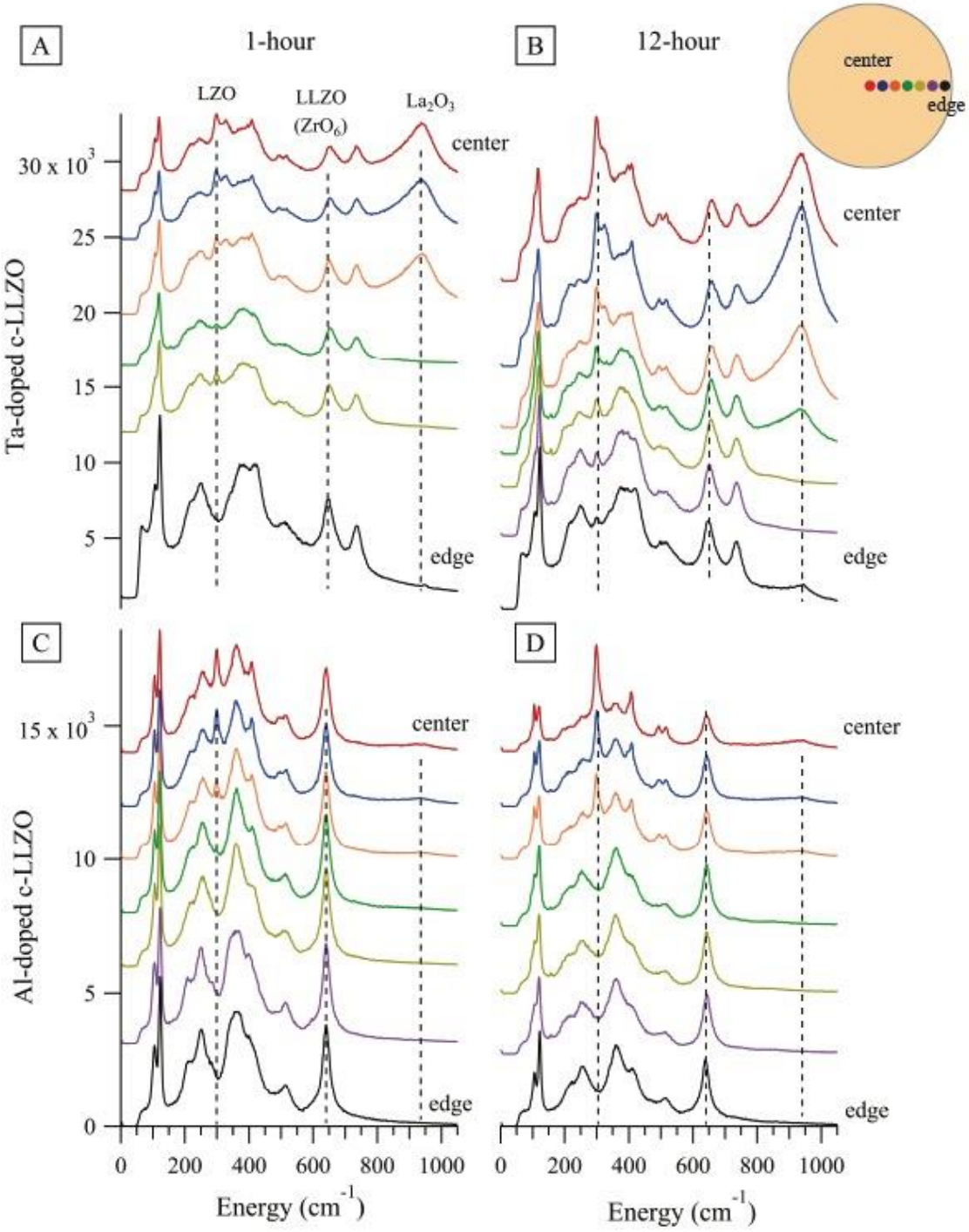

Figure 5a. Waterfall plot of radial measured Ta-doped c-LLZO spectra for 1 hr sintered pellet. **5b**. Waterfall plot of radial measured Ta doped c-LLZO spectra for 12hr sintered pellet. **5c**. Waterfall plot of radial measured Al-doped c-LLZO spectra for 1hr sintered pellet. **5d.** Waterfall plot of radial measured Al-doped c-LLZO spectra for 12hr sintered pellet.

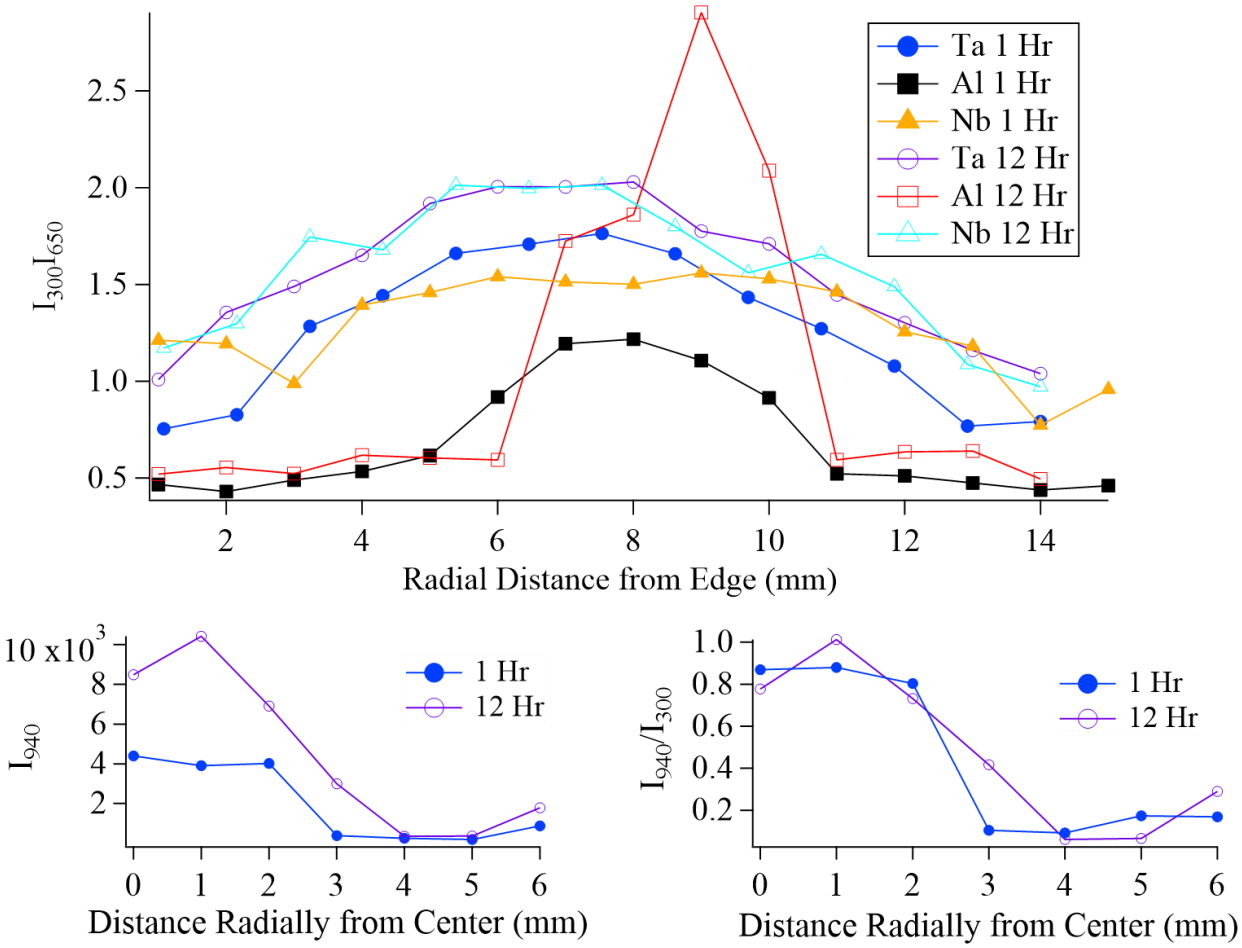

Figure 6a. Radial distance from edge vs I_{300}/I_{650} ratio for each sample sintered. **6b.** Intensity of I_{940} where lanthanum oxide is measured from the center of Ta 1 hr and 12 hr sintered pellets to their edges. **6c.** Intensity ratio I_{940}/I_{300} measured radially from the center for Ta 1 hr and 12 hr sintered pellets.

Raman spectroscopy is a valuable tool for determining *relative* changes in material composition and secondary phase formation. However, Raman spectroscopy is not well-suited for determining *absolute* amounts of materials. In contrast, XRD patterns can be analyzed to report percent mass composition based on the intensities of different diffraction peaks. Figures 7-9 show XRD patterns for the three different samples. Figure 7 displays the XRD pattern for the 1 hour sintered Ta doped *c*-LLZO pellet. Jade software was used to assign

individual features and Rietveld refinement was used to determine relative mass percentages of the different materials. Distinctive to LZO, the XRD feature at 28.6 2θ was the basis for determining this secondary phase's mass percentage. Quantitative analysis assigns LZO a mass percent ≤ 7% for the total volume sampled. A very small feature at 29.8° suggests the presence of La_2O_3, however this feature is so small that Rietveld refinement cannot accurately report the mass percentage so we report that La_2O_3 content is ≤1%. Numerically using ratios from Figure 2 in the Appendix, this value must be 2% La_2O_3 by mass.

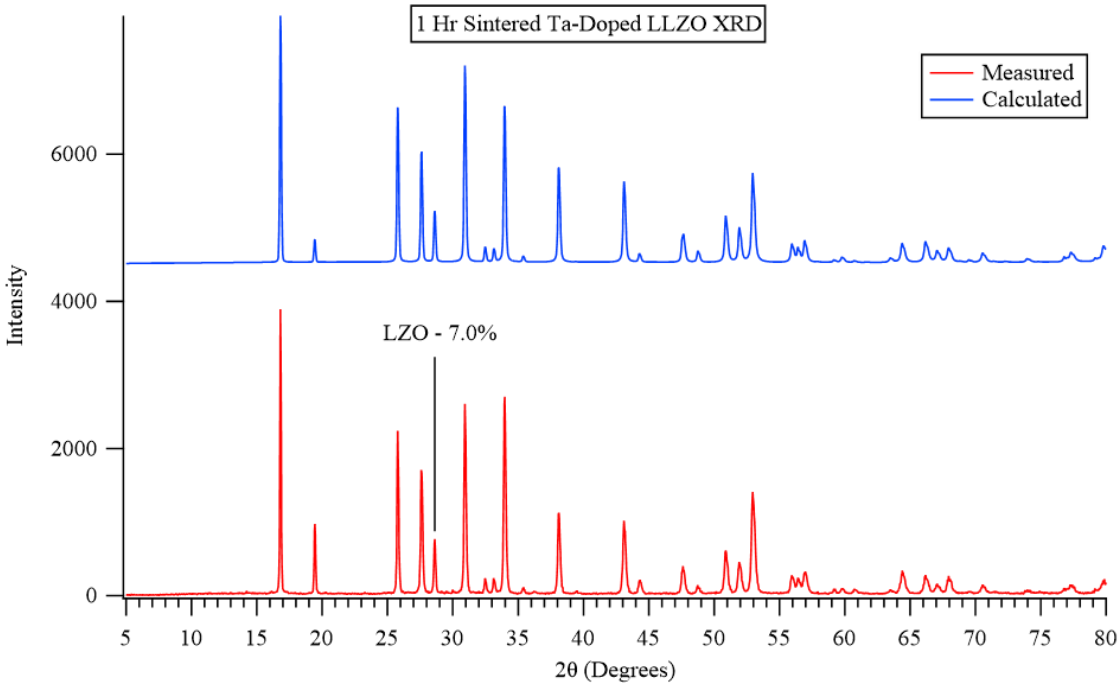

Figure 7. XRD measured and calculated for 1 hr sintered Ta-doped c-LLZO pellet. LZO peak is marked for comparison.

Figure 8. shows the measured and calculated XRD pattern for the Ta-doped *c*-LLZO pellet that was sintered for 12 hr. The feature for LZO at 28.6° is large relative to the 1 hr sintered Ta-doped *c*-LLZO pellet pattern measurement. Based on its magnitude, this LZO feature is calculated to represent 13.1% LZO by mass, nearly double the amount of LZO formed

for the 1-hr sintered pellet and indicating significant lithium depletion. A measurable feature at 29.6°is assigned to La_2O_3 and refinement estimates this material to comprise 2.8% of the sample by mass. Nb-doped samples measured very high LZO percentages for both the 1-hr and 12-hr sintered pellets. The 1-hr sintered pellet has 13.1 % LZO by mass and 17.9% for the 12-hr sintered pellet.

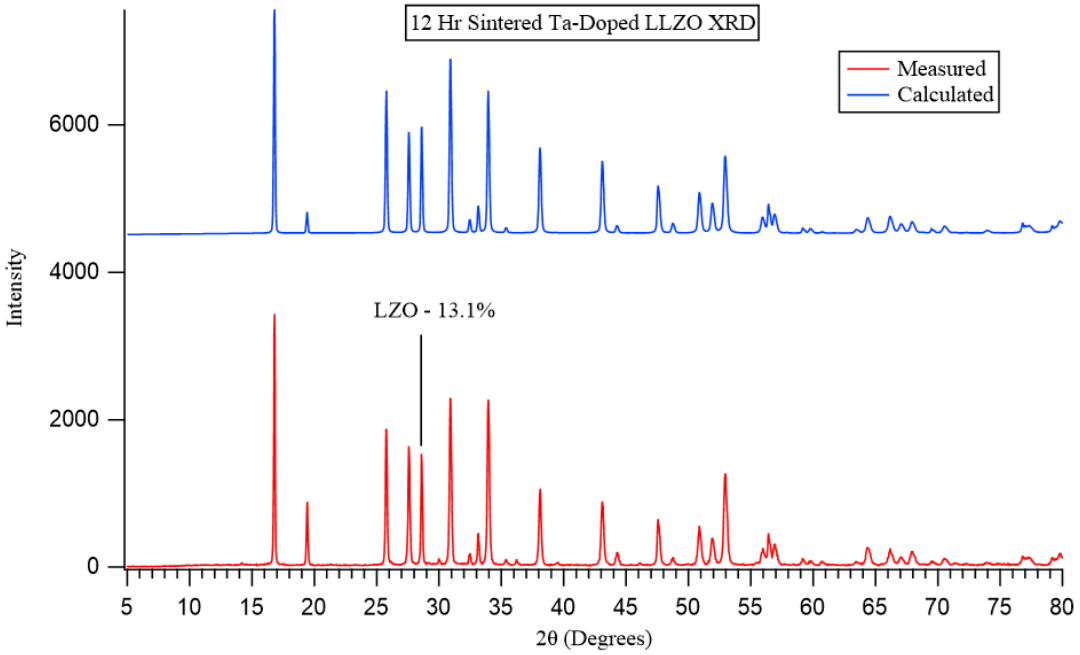

Figure 8. XRD measured and calculated for 12 hr sintered Ta-doped c-LLZO pellet. LZO peak is marked for comparison.

Figure 9 displays the XRD pattern for the 12-hr sintered Al doped *c*-LLZO pellet. The 28.6° feature for the Al sample is small and barely noticeable. The calculated mass percent for LZO peak is 1.5%, approximately an order of magnitude less LZO than was observed in the Ta-doped and Nb-doped samples samples. The higher LZO percentage for the Ta and Nb pellets further supports Raman and TGA results showing that Ta-doped and Nb-doped samples are more prone

to LLZO decomposition and LZO formation. Table 4. shows the LZO mass percent for Al, Ta, Nb doped samples sintered at both 1 and 12-hrs.

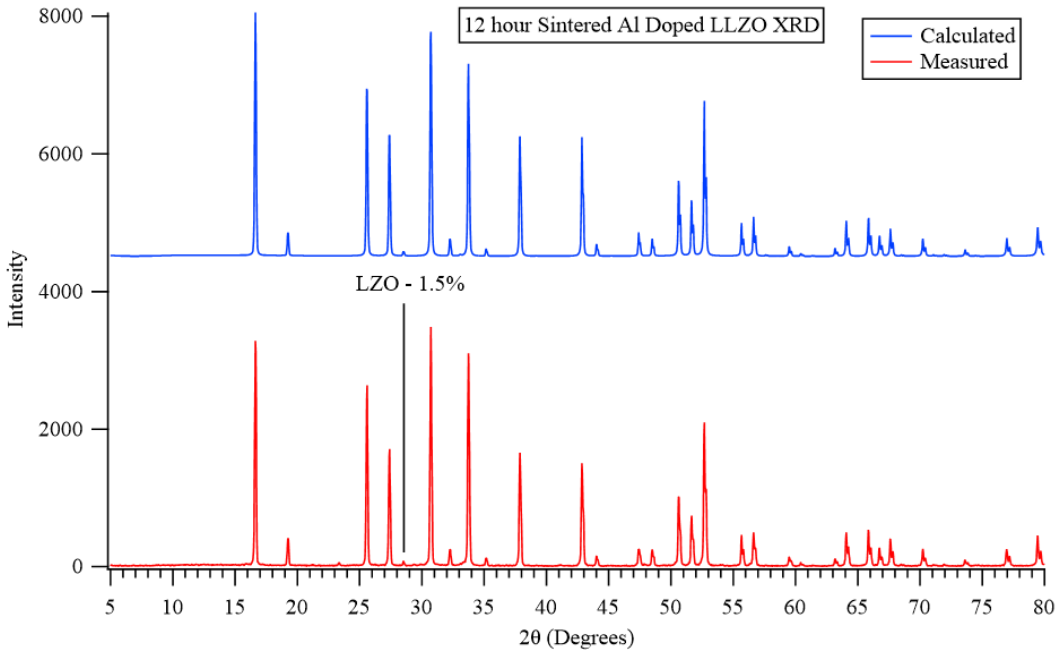

Figure 9. XRD measured and calculated for 12 hr sintered Al-doped c-LLZO pellet. LZO peak is marked for comparison.

Table 4. LZO percentage by dopant type and time sintered for a representative sample. Variances and ranges are included in the narrative.

XRD Results	Unsintered LLZO		1hr		12hr		Lattice Parameters
Starting Material	LLZO %	LZO %	LLZO %	LZO %	LLZO %	LZO %	LLZO Starting Materials
Al LLZO	100	0	98.3	1.7	98.5	1.5	a = 12.972 Å
Ta LLZO	96.8	3.2	93	7	86.9	13.1	a = 12.945 Å
Nb LLZO	99.8	0.2	94.1	5.9	91.7	8.3	a = 12.913 Å

Discussion

c-LLZO is an attractive SSB electrolyte candidate because of its high conductivity and because the cubic phase, naturally stable at higher temperatures, can be stabilized at room temperature by

substituting dopants for Li, La, Zr, and even O.[75] The most common dopants substitute for Li and for Zr. The experimental results presented in the previous section show that the lithium substituted Al-doped *c*-LLZO is more chemically stable than either Ta-doped or Nb-doped *c*-LLZO, both being Zr-substituted materials. When heated to 900˚C, Al-doped *c*-LLZO loses less mass (15 ± 1.5%) compared to Ta-doped (23 ± 0.2%) and Nb-doped (20 ±2.4%) *c*-LLZO. Assuming that much of the high-temperature mass loss is due to Li_2O volatilization, we conclude that Li is more mobile and/or is less tightly bound in the Zr-substituted forms of *c*-LLZO.

These differences also manifest in the secondary phases that form during thermally induced *c*-LLZO decomposition. LZO is observed in all samples, but the Al-doped *c*-LLZO shows less LZO and the spatial distribution is more tightly localized compared to the widespread LZO distributed across Ta-doped and Nb-doped samples. Furthermore, Ta-doped and Nb-doped *c*-LLZO show strong La_2O_3 growth in samples that have sintered for 12 hours. La_2O_3 is a product that forms when *c*-LLZO loses all its lithium:

$$2Li_7La_3Zr_2O_{12} \rightarrow 7Li_2O + 2La_2Zr_2O_7 + La_2O_3$$

With La_2O_3 clearly present in the Raman spectra of Zr-substituted samples and largely absent in the Li-substituted sample, we propose that Ta-doped and Nb-doped *c*-LLZO materials are less thermally stable than Al-doped *c*-LLZO, and that this difference arises from Al^{3+} blocking lithium conduction pathways while Ta^{5+} and Nb^{5+} leave these pathways unimpeded. This assertion is supported by both the TGA data showing more mass loss for Ta-doped and Nb-doped samples and from X-ray diffraction data.

The crystal structures of the three materials are unlikely to be responsible for Ta-doped and Nb-doped *c*-LLZO's thermal instability. After refinement, Al-doped, Ta-doped, and Nb-doped *c*-LLZO have lattice constants of 12.972 Å, 12.945 Å, and 12.913 Å, respectively.

The Al-doped sample has the largest lattice parameter of the three materials but is also the least susceptible to thermal degradation. If lattice size were correlated with lithium mobility, the XRD results would predict Al-doped *c*-LLZO to be the *most* susceptible to thermal degradation, followed by Ta-doped and then Nb-doped *c*-LLZO.[137, 138, 139] The data do not support this hypothesis.

Instead, we consider two other phenomena that might explain these results. First, lithium site dopants replace Li^+ in lithium conduction pathways within an LLZO unit cell. Specifically, Al^{3+} substitutes directly for lithium ions, preferentially occupying 24d sites in the lattice and creating 3 Li^+ vacancies. These vacancies enable lithium conductivity, but by occupying a 24d site, Al^{3+} ions block up to four of the lithium conducting pathways through the material. Ta and Nb doped *c*-LLZO substitute a 5+ ion for Zr^{4+} and one Li^+ creating a Li^+ vacancy and enable lithium conduction without blocking lithium conducting pathways.[77] While the improved mobility may benefit Zr-substituted *c*-LLZO electrolytes in terms of their final ion conductivity, the intrinsic material structure may limit their ability to be processed for their intended application.

A second phenomenon is the formation of $LiAlO_2$ that has been reported on Al-doped *c*-LLZO.[126] Selected area electron diffraction taken in tandem with TEM measurements show that this material can form a thin surface coating around LLZO grains. [136, 140] This coating is believed to hinder lithium volatilization from the material at elevated temperatures. The combination of these two phenomena – impeded lithium mobility and a conformal secondary phase coating – would effectively slow lithium transport, and hinder lithium volatilization in Al

doped c-LLZO. These explanations are consistent with experiments shown in this report and explain how Li site dopants are more thermally stable than Zr site dopants.

Conclusions

In this work, we have examined the thermal stability of 3 different c-LLZO dopants (Al Li-site, and Ta/Nb Zr-site) using three primary methods (XRD, TGA, Raman microscopy). One lesson learned from the analyses described in this work is that complementary analytical techniques are necessary when assessing *c*-LLZO degradation to develop accurate descriptions of secondary phase formation mechanisms. Based on post-sintered Raman spectra, *c*-LLZO breaks down into multiple secondary phases including LZO and La_2O_3. Furthermore, these materials have different spatial distributions across the sample, and these distributions depend on both dopant and sintering times. Such information is not readily available in XRD results, *but* XRD does provide quantitative information about the extent of *c*-LLZO decomposition.

TGA results indicated that Zr – site dopants (Ta and Nb) lose more mass during sintering than Li site dopants (Al) and all samples experience 5 unique mass loss events, however these occur at different rates and slightly different temperatures for each sample. Raman microscopy was used to determine spatially where LZO, the primary decomposition product is found on a sintered LLZO pellet, and using ratios (I_{300}/I_{650}) the relative amount of LZO between samples was found. Raman results also show an additional decomposition product for the Zr-site dopants in La_2O_3 which represents further decomposition beyond LZO. XRD results showed specific amounts of LZO formation due to decomposition of c-LLZO, with nearly 10-fold more LZO for Ta and Nb doped samples compared to Al doped c-LLZO. Results indicate that Al doped c-

LLZO is significantly easier to process, while remaining more thermally and chemically stable compared to Zr site dopants Ta and Nb.

CHAPTER FOUR

THERMAL HEAT TREATMENT AS STRATEGY FOR CLEANING *t*-LLZO AND *c*-LLZO SURFACES AND IMPROVING ELECTROCHEMICAL PERFORMANCE IN SOLID-STATE BATTERIES

Contribution of Authors and Co-Authors

Manuscript in Chapter 4

Author: Steven Thomas Montoya

Contributions: Collected and analyzed all data, generated figures and wrote manuscript in preparation for publication.

Co-Author: Shah Ali Haider Shanto

Contributions: Made pellets, measured replicated data.

Co-Author: Robert A. Walker

Contributions: Assisted in planning experimental studies and interpreting results. Edited and assisted in preparation of the manuscript.

Manuscript Information

Steven T. Montoya, Shah A. H. Shanto, Robert A. Walker

Status of Manuscript:
☒ Prepared for submission to a peer-reviewed journal
☐ Officially submitted to a peer-reviewed journal
☐ Accepted by a peer-reviewed journal
☐ Published in a peer-reviewed journal

THERMAL HEAT TREATMENT AS STRATEGY FOR CLEANING t-LLZO AND c-LLZO SURFACES AND IMPROVING ELECTROCHEMICAL PERFORMANCE IN SOLID-STATE BATTERIES

By Steven Montoya, Shah Shanto, Rob Walker

Abstract

Work presented in this chapter describes a high temperature heat treatment for the lithium ion conducting ceramic $Li_7La_3Zr_2O_{12}$ (LLZO) that removes surface contaminants such as Li_2CO_3 as well as protective coatings intentionally used to prevent lithium volatilization during sintering. Heating post-sintered LLZO at 800 ℃ for 1 hr in air renders the LLZO surface chemically pristine and, in the case of *c*-LLZO, increases chemical stability post-treatment. This result contrasts with results of *c*-LLZO that has been mechanically polished, the more traditional means of cleaning LLZO post-sintering. Raman spectroscopy is used to investigate surface composition in a series of *in situ* and *ex situ* measurements. EIS is used to characterize conductivity of two different cleaning methods – thermal conditioning and mechanical polishing. Thermal conditioning has clear advantages in creating a LLZO substrate better suited for use in electrochemical applications.

Introduction

Adverse environmental impacts resulting from fossil fuel use has driven the need for alternative energy conversion technologies that are both clean and durable.[141, 142] Technologies such as batteries and fuel cells have generated considerable interest as means to improve power generation efficiency from clean energy resources while remaining safe and scalable.[143, 144, 145]

Of the different clean energy solutions being explored, lithium ion batteries have commanded the spotlight due to their high energy densities (<250 Wh/kg), wide electrochemical windows, high power densities (<5000 W/L), and long cycle life (<3000 cycles).[146, 147, 148] However traditional lithium-ion batteries also suffer from significant safety risks including formation of uncontrolled and uneven SEI layers and dendrites that puncture charge separators and short circuiting batteries.[149, 150, 151] When a dendrite punctures a charge separator, the highly flammable organic electrolyte solvents can ignite causing catastrophic damage.[152, 153]

All solid-state batteries (SSBs), despite having lower power densities and shorter life cycles, *can* improve operational safety, energy density and electrochemical window width.[50,154] This tradeoff has catalyzed efforts to develop new solid-state electrolyte materials having improved power densities and cycle life in order to make safe, next-generation storage devices that improve performance in all respects. Increasing electrolyte conductivity, as well as improving electrolyte/electrode contact will lead to SSBs having higher power densities. Consequently, limiting surface contaminants and thereby improving charge transport across electrolyte/electrode interfaces has become an active area of study.[155]

Lithium lanthanum zirconate ($Li_7La_3Zr_2O_{12}$ or LLZO) is a lithium-ion conducting ceramic that is being considered as an electrolyte candidate for lithium-ion SSBs. LLZO can adopt two different crystal structures: tetragonal (*t*-LLZO) and cubic (*c*-LLZO). *t*-LLZO is the stable phase at room temperature and 1 atm pressure, but *c*-LLZO has higher ion conductivities and can be stabilized by elemental dopants.[100] *c*-LLZO has high conductivity (~1 mS/cm), resistance to dendrite growth, and is able to use elemental lithium anodes allowing batteries with *c*-LLZO electrolytes to have a very high theoretical energy densities (470 Wh/L).[156, 157] While

t-LLZO is the stable form of this material at room temperature, *c*-LLZO can be stabilized under ambient conditions when doped with a suitable metal (Al, Ta, Nb, etc.) that substitutes for Li, Zr, La, or O.[75] Some strategies have proposed using mixed LLZO polymorphs as electrolytes to leverage the mechanical stability imparted by *t*-LLZO with the superior ion conductivity of *c*-LLZO.[158]

To serve as a battery electrolyte, LLZO must be synthesized, sintered, and then cleaned in preparation for application of anodes and cathodes. These three steps present challenges to creating high performance batteries including decomposition of the parent material to form secondary phases as well as contamination from additives used to fabricate electrolyte assemblies or protective coatings intended to lithium volatilization during sintering. One decomposition product, Li_2CO_3, often forms a surface layer during sintering that eventually compromises contact between the electrolyte and electrodes. A second contaminant is residue left behind by GraFoil, a carbon-based protectant applied to LLZO before sintering to inhibit Li_2CO_3 contamination and lithium volatilization.[159] After sintering, however, the carbon residue left by GraFoil must be removed before electrodes can be applied. Typically, the residue is removed by mechanical polishing,[160] although mechanical polishing sensitizes the LLZO surface to secondary reactions. Consequently, mechanically polished samples must immediately have electrodes applied to ensure optimal electrode-electrolyte contact. Developing strategies to remove surface contaminants from both *c*-LLZO and *t*-LLZO are critical to overcome if this material is to realize its potential as a high performance solid-state lithium-ion battery electrolyte.[94]

Previous work by Zhang, *et al.* describe a novel heat treatment technique for *c*-LLZO that thermally cleans the *c*-LLZO surface by forcing Li_2CO_3 formed during processing to decompose and volatilize. This reported heat treatment heated *c*-LLZO contaminated with Li_2CO_3 to temperatures of 650 ℃, 750 ℃, and 900 ℃ for 1 hr under Ar. After the sample had cooled, Raman spectra, HAXPS data, and critical current density measurements showed that the highest temperature treatment was most effective in ridding the surface of Li_2CO_3. However, the 900 ℃ treatment also showed evidence of lanthanum zirconate (LZO), an insulating phase that forms when *c*-LLZO experiences lithium depletion.

Experiments presented below expand on Zhang, *et al*.'s findings in three important ways: first, all experiments are performed at 800 ℃ under air. *Ex situ* and *in situ* vibrational Raman measurements show no LZO being formed while Li_2CO_3 still decomposes and volatilizes. Second, our work demonstrates that using heat treatment to thermally clean *t*-LLZO and *c*-LLZO samples is effective for more than simply removing Li_2CO_3 thin films. Heating post-sintered *c*-LLZO samples to 800˚C in air effectively removes carbon residue left behind on the sample surface after the sample was protected with GraFoil during sintering. Third, heat treating *c*-LLZO renders it more chemical stable and more conductive in simple cell geometries than mechanically polished *c*-LLZO electrolytes. Curiously, the chemical stability conferred to *c*-LLZO is not observed with heat treated *t*-LLZO.

Methods

Material Processing. t-LLZO materials were prepared using undoped *t*-LLZO powder manufactured by Ampera (Tucson, Arizona, USA) and distributed by MSE Supplies (Tucson, Arizona, USA). *c*-LLZO materials were synthesized in-house using previously described

methods.[161, 110] Pellets of both materials were pressed using 0.5g of material in a 10 mm diameter die for 10 seconds under 300 MPa of pressure. *c*-LLZO pellets were then sintered at 1150 ˚C for 2 hr with a GraFoil (NeoGraf Solutions) protective film on the top and bottom of the pellets. *t*-LLZO pellets were sintered at 1000 ˚C for 2 hr uncovered.

Raman Spectroscopy. Raman spectra were taken using a Renishaw InVia Microscope with a 488 nm single line argon laser. Measurements were taken for 3 ten second acquisitions using 5mW of laser power. *In situ* measurements were taken using a Linkam CCR1000 catalyst stage with flowing air, at 800 ˚C for 1 hr with measurements taken every 5 minutes.

Electrochemical Impedance Spectroscopy (EIS). EIS data were taken from 1 to 1,000,000 Hz using VersaSTAT MC by Ametek potentiostat spectrometer. Aftermath Data Organizer™ software was used to determine fits to modified Randle's circuit model, a common model used to fit LLZO's ionic conductivity. Fits to the data were used to calculate bulk ionic conductivities for c-LLZO pellets.

Results and Discussion

Sintering LLZO often results in a thick Li_2CO_3 layer that forms when carbon-containing additives and stabilizers react with LLZO's lithium.[162, 163] Figure 1a shows Raman spectra from a *t*-LLZO sample prior to sintering, after sintering, and after being subjected to post-sintering heat treatment (800˚C for 1 hour in air). The pre-sintered sample spectrum is consistent with previous literature reports. The spectrum from the post-sintered sample shows less well resolved features and differences in relative vibrational band intensities. Notable in the post-sintered sample is the very strong vibration at 1084 cm^{-1} indicating extensive growth of Li_2CO_3.[164] Heat treating this

sintered sample at 800 ℃ leads to loss of the carbonate vibrational band and a reappearance of the typical *t*-LLZO vibrational spectrum.

The Raman spectrum of *t*-LLZO (including Li_2CO_3) includes many vibrational features that are cataloged in Table 1 along with their assignments:[85]

Table 1. Frequencies and assignments for common Raman vibrational modes for LLZO and secondary phases.

Frequency (cm^{-1})	Assignment
240	O Bending
290	O bending
329	Li-O Stretch
365	Li-O Stretch
397	Li-O stretch
485	Li-O stretch
640	ZrO_6
1084	Li_2CO_3

While the post-sintered spectrum (Figure 1a, middle) contains several of the major *t*-LLZO features, the spectral resolution is much poorer and several of *t*-LLZO's vibrational bands remain only as low intensity shoulders in the spectrum. Missing in this spectrum are characteristic bands at 240 cm^{-1}, 329 cm^{-1}, and 365cm^{-1}. The observed spectral changes might be interpreted as material degradation, but we believe a more likely explanation is that such a thick Li_2CO_3 film formed on the *t*-LLZO surface that light reaching the LLZO material is less intense than what impinges on the surface and the Raman scattered light is also attenuated by inelastic scattering as it reflects out of the sample.

We have several reasons for asserting that a thick Li_2CO_3 film on the post-sintered sample is responsible for the poorer quality post-sintered spectrum in Figure 1a. First, several existing features in the post-sintered spectrum appear lower in relative intensity but *no new features* characteristic of secondary phase formation appears. Second, after reheating the sample to 800˚C for one hour in air and then cooling to room temperature, the Li_2CO_3 all but disappears and the *t*-LLZO features return. Some relative intensities are different, but we note that the pre-sintered sample (bottom) also contains binder and solvent required to press the sample pellet.

Figure 1b shows a sequence of *in situ* spectra from the post-sintered LLZO sample as it is being thermally treated at 800˚C. Vibrational modes for LLZO at 800℃ are observed at 15-20 cm^{-1} lower than at room temperature. We note that at 800˚C, the stable form of LLZO is *c*-LLZO, which forms reversibly from *t*-LLZO at 650˚C. Structural changes in the material can be inferred from the evolving spectral features. Specifically, we calculate intensity ratios for several of the dominant features. From the data in Figure 1a, we calculate ratios for different peak intensities. The most instructive ratio is I_{380}/I_{1064}. The vibrational band at 380 cm^{-1} has been assigned to Li-O stretching motion and the band at 1164 cm^{-1} is due to the carbonate film that formed on the LLZO surface during sintering. After ramping the temperature quickly to 800 ˚C (at 50˚C per minute), the data show the carbonate peak diminishing in intensity to almost zero. The Li-O feature also loses intensity but at a slower rate. As a result, we interpret this ratio to reflect thermally induced decomposition of Li_2CO_3 and the re-emergence of the underlying *t*-LLZO.

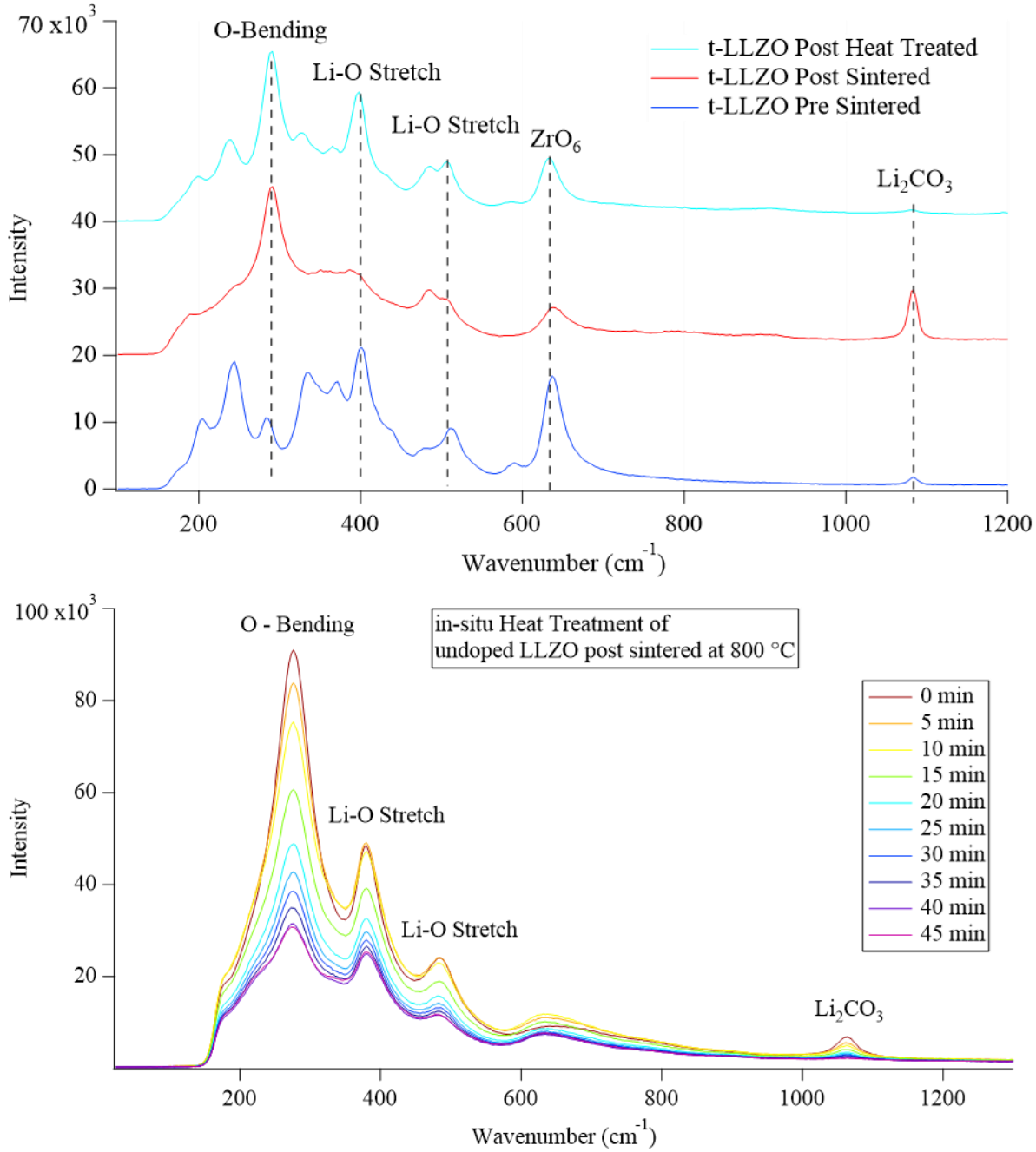

Figure 1a. Raman spectra of pre sintered t-LLZO, post sintered t-LLZO, and post annealed t-LLZO. 1b.In situ Raman spectra of heat treated (800 ℃ for 1 hr) post sintered t-LLZO pellet.

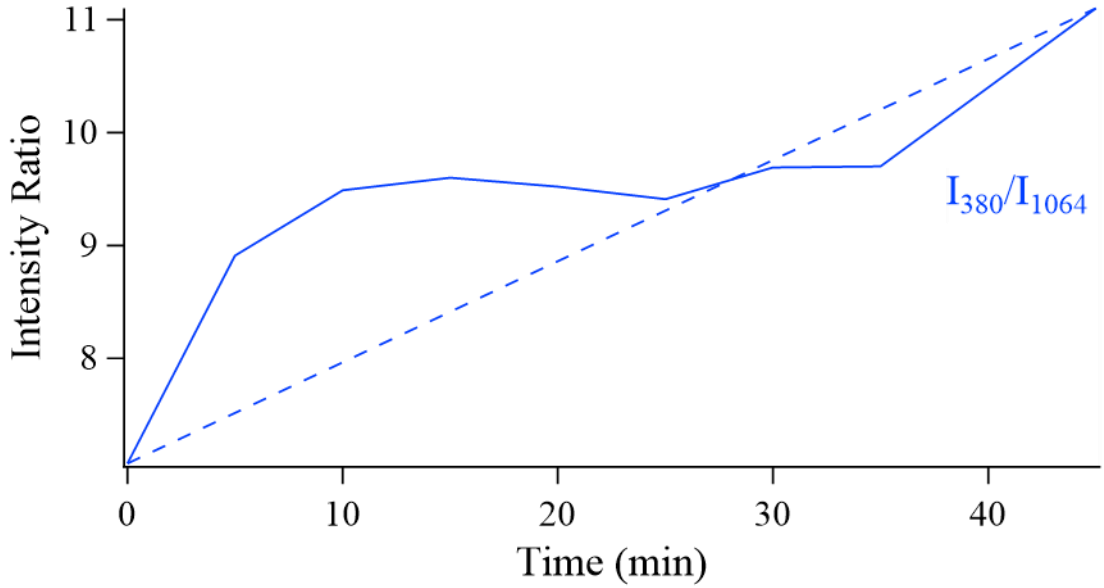

Figure 2. Plot for intensity ratio I_{380}/I_{1064} from Figure 1 for each time point. Dashed line is linear regression for data.

Closer inspection of the Li_2CO_3 vibrational band at 800˚C shows that this feature disappears steadily over time. Figure 3a shows an expanded view of the carbonate stretching band from the post-sintered LLZO sample as it undergoes heat treatment. After 45 minutes, the carbonate vibrational feature has all but disappeared. Figure 3b plots the natural log of the carbonate intensity as a function of time. The linear behavior observed in Figure 3b is strong evidence that Li_2CO_3 follows first order decomposition kinetics.

Further evidence that heat treatment will remove Li_2CO_3 from the *t*-LLZO surface without inducing significant LLZO degradation or secondary phase formation is inferred from *t*-LLZO's thermal stability. Figure 4 shows thermal gravimetric analysis data for *t*-LLZO and for Al-doped *c*-LLZO. Similar data for different *c*-LLZO doped samples presented in Figure 3 implied that LLZO does not undergo significant thermally induced degradation until a sample has lost more than 12% of its mass. This degradation results from lithium loss (in the form of

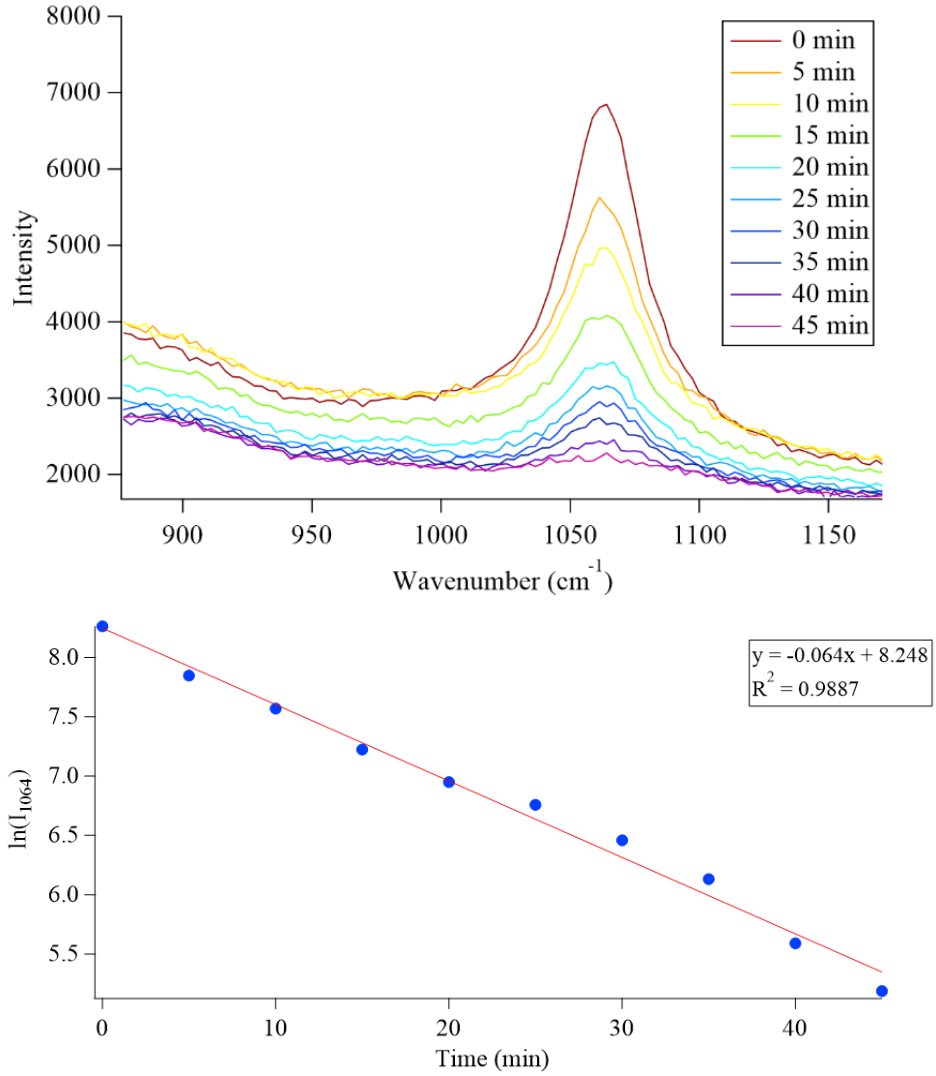

Figure 3a. Expanded view of Figure 1b carbonate removal showing the lithium carbonate peak at 1064 cm^{-1}. 3b. Exponential decay kinetics for carbonate removal plotting time vs $\ln(I_{1064})$.

volatile Li_2O). As shown in Figure 4 in Chapter 3 of this dissertation, this event happens at ~890˚C for Al-doped *c*-LLZO, well above the 800˚C of the thermal treatment in this work.

Heat treating the sintered samples have an additional impact on LLZO stability. Figure 5 shows Raman spectra from post-sintered *t*-LLZO as well as from *t*-LLZO immediately after annealing and 19 days after annealing. These spectra appear different from the post-sintered spectra shown in Figure 1. During the 19-day interlude between annealing and the final

measurements, the sample was placed in a clean sample bag and stored in a desiccator. Using the carbonate peak at 1084 cm^{-1} in the post-sintered sample for normalization, annealing the sintered

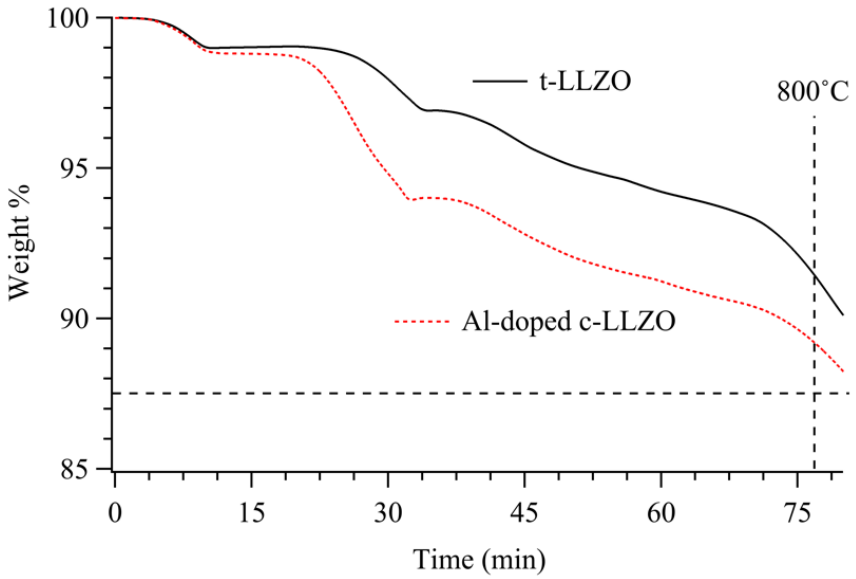

Figure 4. Thermal gravimetric analysis data for *t*-LLZO (black) and Al-doped *c*-LLZO (red) samples. The vertical dashed line at 77 minutes shows the time when the sample temperature reaches 800˚C. The horizontal dashed line at 87.5 weight % shows the threshold for LLZO decomposition and formation of LZO. (See Chapter 3.)

sample reduced this band's intensity ≥ 50-fold. Importantly, after annealing, the Raman spectrum of the *t*-LLZO showed *all* 10 allowed vibrational modes. After 19 days of storage, the annealed pellet showed the return of a carbonate feature that is approximately 20% of its original, pre-annealed intensity. This result indicates no substantial increase in chemical stability due to heat treatment for t-LLZO.

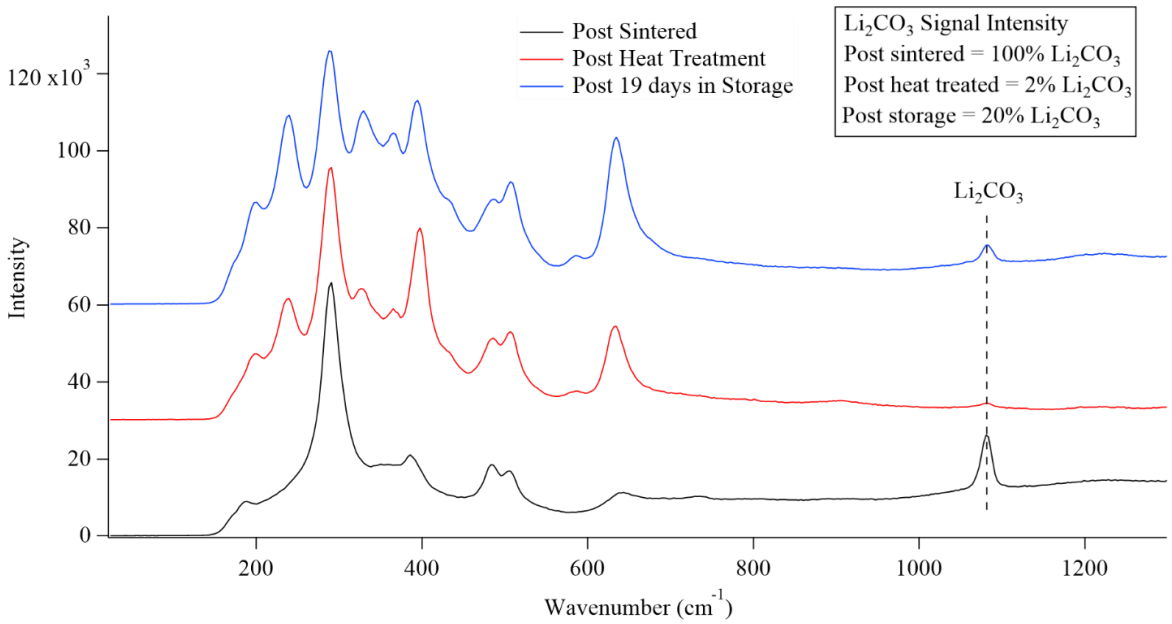

Figure 5. Raman spectra for post sintered t-LLZO, post heat treatment, and post 19 days in storage in desiccator before battery assembly.

t-LLZO and *c*-LLZO can exhibit different thermal and chemical stabilities and thus measurements in Figures 2 and 3 showing carbonate removal of lithium carbonate from *t*-LLZO are consistent with those reported by Zhang et al. and broaden those finding to the room-temperature phase of undoped LLZO, *t*-LLZO. However, c-LLZO is the material that has attracted the greatest research interest as a SSB electrolyte, leading us to explore if modest heat treatment as described above can serve as a general strategy for removing other surface contaminants. The studies described below examine heat treatment's efficacy in removing carbon residues that remain after sintering *c*-LLZO under GraFoil.

To address this issue, *c*-LLZO that had been sintered with a GraFoil protective coating was subjected to heat treatment at 800˚C in air for 1 hour. Figure 6a shows fragments of *c*-LLZO after sintering with GraFoil (left, pre-HT) and after the sintered sample had been heat treated (right, post-HT). The pre-HT sample shows a gray color resulting from graphitic residue that

remains after the sample has been sintered and the GraFoil removed. The post-HT sample evinces a light tan color reminiscent of native Al doped *c*-LLZO. Figure 4b shows three spectra: the black trace is the spectrum for the post sintered *c*-LLZO pellet, the red trace is the post-HT sample, and the blue trace is from the same, post-HT sample *after* 14 days.

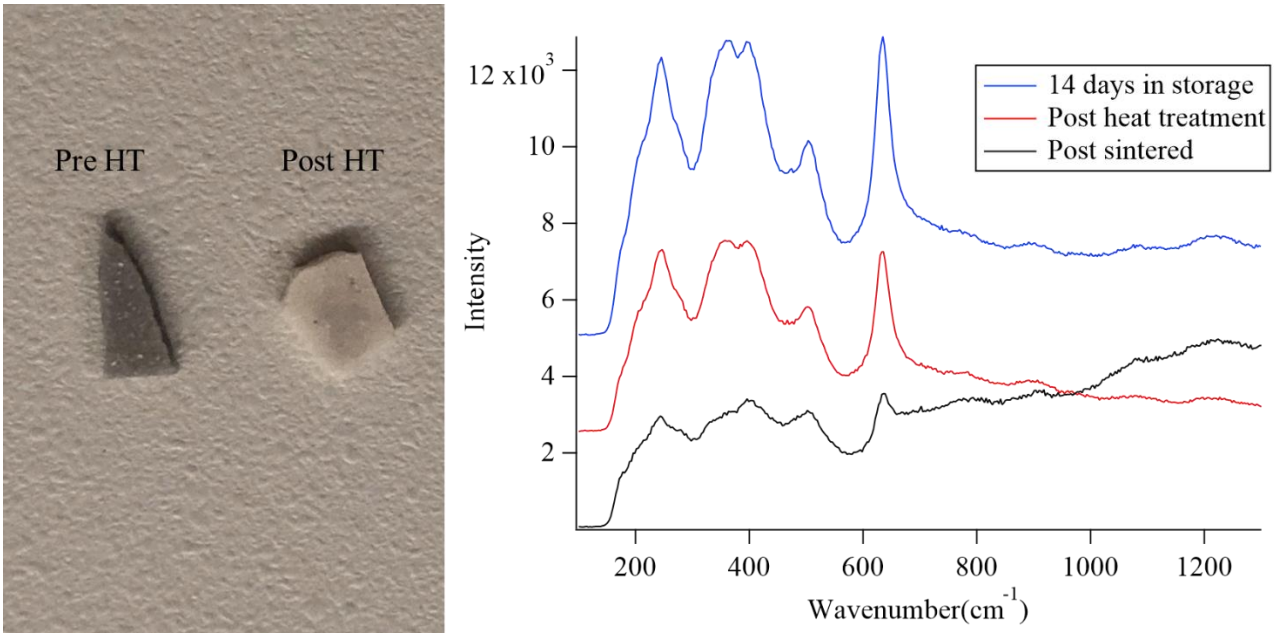

Figure 6a. Image of pre heat treated and post heat treated c-LLZO. 4b. Raman spectra for post sintered c-LLZO, post heat treated c-LLZO and post 2 weeks in storage. Spectra have been offset vertically for clarity.

Two important findings from Figure 6 stand out. First, heat treating *c*-LLZO successfully removes GraFoil residue. This result is visibly apparent in Figure 6a and also evident in Figure 6b, where the spectrum from the post-sintered sample (bottom) is poorly resolved with a rising baseline to higher frequencies, characteristic of a roughened surface and a thick contaminant layer. After heat treatment, a Raman spectrum from same sample (Figure 6b, middle) shows strong features characteristic of *c*-LLZO and a baseline that approaches zero at higher frequencies. Third, heat treating confers chemical stability as evidenced by an absence of

any Li_2CO_3 in the aged sample. (Compare the top spectrum from Figure 6b to the top spectrum of Figure 5 showing Li_2CO_3 reappearing in the *t*-LLZO sample that has aged for 19 days.)

The same chemical stability observed in the *c*-LLZO sample that has been heat treated *is not* observed in a *c*-LLZO sample whose carbon residue has been removed by mechanical polishing. Figure 7 shows three Raman spectra. The first spectrum (bottom) is from a *c*-LLZO that had been mechanically polished after being sintered under Grafoil. While there may be a trace of Li_2CO_3 evident in this spectrum as evidenced by a slight rise in the signal with a S/N of ~1.0, the Li_2CO_3 signal is abundantly clear in the mechanically polished sample after is has sat for 1 day bagged in a desiccator (middle spectrum). After 1 week, the Li_2CO_3 vibrational band is ~20x more intense than it was immediately after polishing. These observations demonstrate that the surface of mechanically polished c-LLZO is more reactive than *c*-LLZO that has been heat treated after sintering.

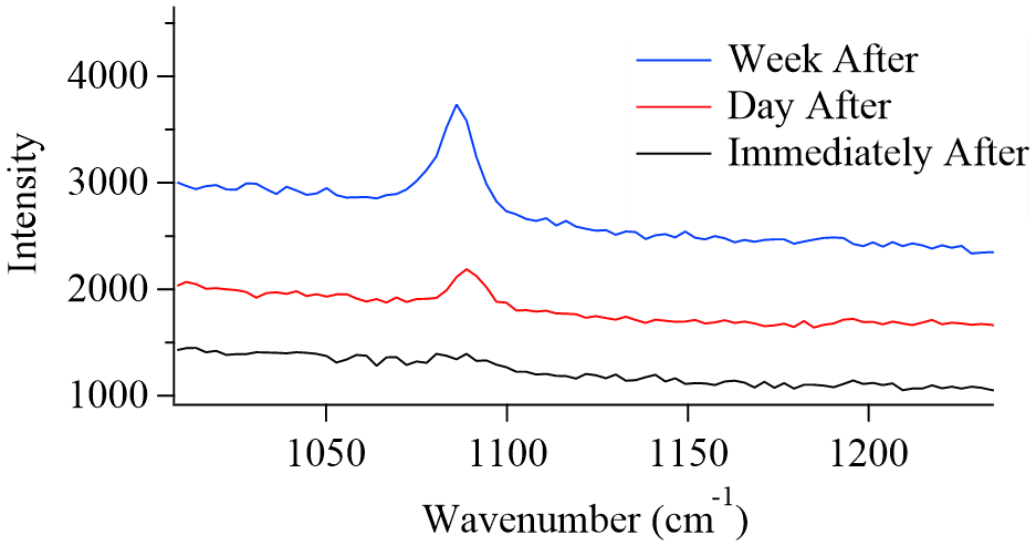

Figure 7. Raman spectra for mechanically polished Grafoil coated c-LLZO pellet, following polish, the day after and 1 week after.

To assess how these processing differences – heat treating vs. mechanically polishing – affected *c*-LLZO's properties as an electrolyte, six *c*-LLZO pellets were pressed and sintered with GraFoil. Three of these pellets were heat treated at 800˚C in air for one hour. The other three pellets were mechanically polished using 240 grit sandpaper for 5 minutes on each side of pellet. After processing – heat treatment or mechanical processing – all pellets were immediately sputter coated with gold for 2 minutes at 20 mA using an Emitech K575X peltier cooled metal coater per side. The gold layers were ~10nm thick. Pellets were then placed in an 8-channel assembly used for button cell testing and electrochemical impedance data were acquired using a VersaSTAT MC by Ametek potentiostat. Figure 8 shows representative Nyquist plots for heat treated and mechanically polished samples. In these plots, the real and imaginary impedance data acquired at high frequencies appear on the left-hand side of the plot while the steeply rising impedance on the right side of the plot are acquired at low input frequency.

The data are not trivial to interpret. Notably, the impedance data for both the heat treated and mechanically polished assemblies have y-offset of ~100 Ohms corresponding to a constant (frequency independent) capacitive contribution to the total impedance. Second, the low frequency data rise linearly but with a steeper slope than would be expected if equivalent circuit elements behaved ideally.

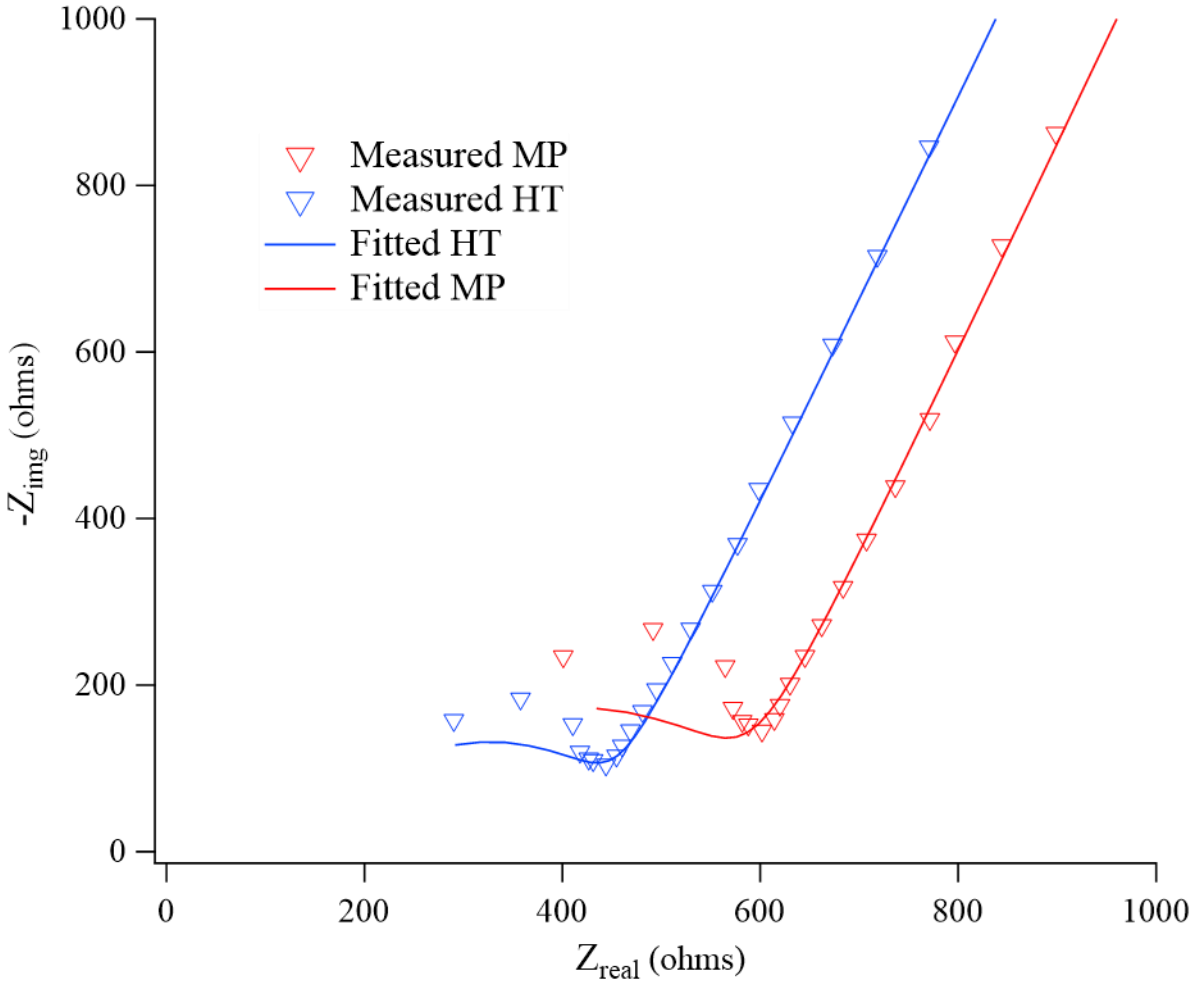

Figure 8. Nyquist plot for averaged Z_{real} vs $-Z_{img}$ for mechanically polished and heat-treated *c*-LLZO pellets. Fitted curves are also plotted for both mechanically polished and heat-treated pellets.

With these considerations in mind, data on the Nyquist plot were fit using a modified Randles circuit shown below. The Randles model is commonly used to fit EIS data from these types of devices.[165, 166] The modified Randles model shown below using constant phase elements (Q) to approximate imperfect capacitors. Q has two fitting variables, Q_n, which is the constant phase element impedance, and α_n which is the dispersion coefficient which quantifies how much a constant phase element deviates from ideal capacitive behavior.

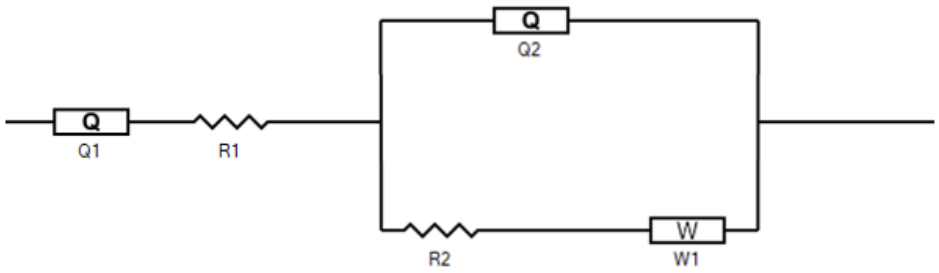

Figure 9. Modified Randles circuit.

The modification to the simple Randles circuit is the addition of the capacitor at the front of the circuit, Q_1. With inclusion of this circuit element, we can accurately fit the capacitive offset and the steeper than expected low-frequency impedance rise. Tentatively, we propose that Q_1 arises from poor or incomplete contact between the very thin Au electrodes and the *c*-LLZO substrate. Fitting the data in Figure 8 with the impedance arising from the model Randles circuit in Figure 9 leads to the following fitting parameters (Table 2):

Table 2. Fit values for heat treated and mechanically polished *c*-LLZO using EIS data.

	Heat Treat Avg	Mechanical Polish Avg
Q1 ($\mu s^a/\Omega$)	.484	0.275
α_1	0.753	0.758
Q2 ($\mu s^a/\Omega$)	.0021	0.0014
α_2	0.93	0.911
R1 (Ω)	176	212
R2 (Ω)	255	348
W ($\Omega/s^{1/2}$)	3.21	21.55
σ (mS/cm)	0.413	0.242

From these impedance data, conductivities are calculated as shown in Eq 1.[167] Bulk resistance is calculated by subtracting the R2 value from the R1 value generated by the fit.

$$\sigma_{bulk} = \frac{Pellet\ Thickness\ (cm)}{Bulk\ Resistance\ (Ohms) * Pellet\ Area (cm^2)} \qquad \textit{Eq 1.}$$

Conductivities were calculated to be 0.41 mS/cm ($\pm$ 0.01 mS/cm) for annealed samples and 0.24 mS/cm ($\pm$ 0.03 mS/cm) for mechanically polished samples on average. Results indicate that heat treating c-LLZO pellets as the method of surface cleaning improves electrochemical performance. This ~2-fold improvement in conductivity for the heat treated sample is a robust scaling, regardless of the model used to fit the data. Efforts to fit the Nyquist plots using a simple Randles circuit (without Q_1) led to poorer fits and did not capture the y-offset. The differences between R_1 and R_2, however, still resulted in (lower) conductivities for the heat treated sample that were ~2-fold larger than the mechanically polished sample. The better conductivity observed with the heat-treated c-LLZO samples also coincides with visible observations: the gold electrodes on the heat-treated samples retain a metallic luster over time, while the gold electrodes on the mechanically polished samples show signs of tarnishing after 2-5 days in storage that may be indicative of electrolyte degradation.

Heat treating sintered LLZO samples at 800 ℃ for 1 hr appears to be a promising approach for removing surface contaminants and other residues that remain after sample processing. Heat treating LLZO at 800˚C removes Li_2CO_3 from *t*-LLZO samples and GraFoil residues from *c*-LLZO samples without inducing LZO formation. These results imply that at these lower heat-treatment temperatures, materials retain most or all their original lithium content rather than lose Li^+ to formation and volatilization of Li_2O. Furthermore, heat treating *c*-LLZO also lowers sample impedance compared to samples whose contaminants have been

removed via mechanical polishing. These findings are exciting because heat treating in air is simple and scalable and may provide a means of creating commercial pathways for producing dense *c*-LLZO samples suitable for use as electrolytes in all-solid-state lithium-ion batteries.

Conclusions

t-LLZO and *c*-LLZO are both potential candidates to be used as solid-state electrolytes in next generation lithium-ion batteries. However, successful integration into a battery assembly requires that electrolytes have clean surfaces that can readily bind to applied electrodes. Chief among LLZO's surface contaminants are Li_2CO_3 and protective coatings such as GraFoil used during sintering to prevent LLZO decomposition. Heat treating samples *after* they have been sintered to form dense materials is an effective means of driving Li_2CO_3 decomposition and removing residues left behind by GraFoil. On *t*-LLZO, Li_2CO_3 grows back over time, presumably due to reaction with ambient CO_2 in air. Heat treated *c*-LLZO is less susceptible to Li_2CO_3 formation as evidenced by an absence of the carbonate band in Raman spectra from samples that have been exposed to laboratory air for up to two weeks. Interestingly, mechanically polished *c*-LLZO *is* susceptible to Li_2CO_3 formation with this surface contamination forming on mechanically polished samples within one day. Heat treating *c*-LLZO also improves the material's electrochemical performance compared to mechanically polished samples. EIS data show a decrease both real and imaginary impedance for annealed samples corresponding to increased ionic conductivity for the heat-treated samples.

CHAPTER FIVE

CONCLUSIONS AND FUTURE DIRECTIONS

Conclusions

Experiments presented in this thesis were designed to test, improve, and understand the processing requirements for c-LLZO to be used as an electrolyte in all solid-state batteries. Specifically, characterization techniques were used to monitor Li^+ loss during sintering and post sintering thermal treatment. Results detail the mechanism responsible for LZO formation/LLZO decomposition, thermal comparisons between Li and Zr site dopants during processing and chemical stability increase as a result of a high temperature (800 ℃) annealing treatment.

Chapter 2 demonstrates that Li^+ loss is a result of non-Fickian diffusion resulting from thermal decomposition of c-LLZO at sintering temperatures (1000℃). Raman spectroscopy is used to probe a *c*-LLZO pellet that was sintered to spatially resolve where the insulating contaminant LZO forms after lithium depletion and subsequent LLZO degradation. Results indicated that LZO forms a radially symmetric gradient starting from the center of the pellet and expands to a radius of about 2.5mm. This profile suggests that Li^+ diffusion through the material is faster than Li^+ loss via volatilization at the edges of the pellets. Raman data suggest that an intensity ratio of *c*-LLZO's ZrO_6 stretching motion at 650 cm^{-1} and LZO's F_{2g} peak (O-Zr-O stretch) at 300 cm^{-1} can be used to diagnose the amount of LZO present at a given location. This I_{300}/I_{650} intensity ratio is ~0.60 for pure Al doped c-LLZO samples, and above 0.80 for samples with non-negligible amounts of LZO present. This metric, when paired with spatial Raman

mapping can be used to effectively determine the width of an LZO gradient. Results in this chapter suggest new strategies for LLZO processing that minimize Li^+ loss during sintering.

Chapter 3 presents work examining how dopant identity impacts the thermal and chemical stability of *c*-LLZO. Specifically direct comparisons between Al-doped (a Li-site dopant) *c*-LLZO and Ta and Nb-doped *c*-LLZO (Zr site dopants) were made using *in situ* TGA and *ex situ* Raman spectroscopy and XRD. TGA results show that *c*-LLZO stabilized with the Li-site dopant Al loses less mass (14%) than *c*-LLZO stabilized with Zr-site dopants Ta and Nb (20% and 23% loss, respectively). Furthermore, Al-doped *c*-LLZO shows less mass loss at elevated temperatures compared to the Zr-site dopants. This behavior is likely due to formation of secondary surface phase $LiAlO_2$ that has been reported in the literature. Raman measurements show a homogenous spatial gradient for Al doped *c*-LLZO that is ~5mm across whereas Nb and Ta-doped samples show heterogeneous LZO distribution across the 15 mm diameter sample with higher intensities near the pellet center. The overall spatial distribution of Ta-doped samples show continued LLZO decomposition post-1 hour of sintering spread throughout the entire pellet. Nb-doped samples displayed significant LZO formation that did not substantially increase between short to long sintered times. LZO distributions in Zr-substituted *c*-LLZO was spread from the center to the edge, whereas even the long sintered (12 hour) Al-doped samples did not show any further LZO formation past 1 hr and remained within a 5mm diameter. La_2O_3, a LLZO precursor and decomposition product was seen spectroscopically for both Ta and Nb-doped LLZO. However, lanthanum oxide was not seen for Al-doped *c*-LLZO indicating further decomposition for Zr-site dopants into lanthanum oxide and zirconium oxide. XRD results were able to quantify the total amount of LZO present for the various pellets. Specifically, Nb-doped

LLZO had the most LZO present (17.9%), compared to Ta-doped (13.1%) and Al-doped (1.7%) *c*-LLZO.

Chapter 4 showed the effects of a recently developed heat-treatment method that can thermally clean the surface of LLZO. Using this cleaning method, lithium carbonate, a common LLZO contaminant was cleaned from the surface of *t*-LLZO by heating the material to 800 ℃ in air. Raman spectroscopy was used to monitor carbonate loss *in situ* and carbonate decomposition followed first order kinetics. Heat treated *t*-LLZO showed almost quantitative loss of the carbonate contaminant, but the contaminant slowly grew back during storage. Often, protective coatings such as GraFoil or graphitic foil are used to prevent lithium loss during sintering. However these coatings must be removed prior to electrochemical testing or battery manufacturing. Typical cleaning methods usually consist of mechanically polishing the sample with sand paper to remove the carbon residue. This polishing technique, however, sensitizes the LLZO surface and promotes carbonate growth. To test if thermally cleaning the surface of graphitic foil was possible, a graphitic coated Al doped *c*-LLZO pellet was heat treated at 800 ℃ for 1 hour in air. Visual and spectroscopic testing demonstrated that the heat treatment created a pristine c-LLZO surface. Heat treated samples were compared to mechanically polished samples, and the anneal treated samples showed both an increase in chemical stability with no carbonate growth during storage, and 1.7-fold better conductivity when compared to mechanically polished samples.

Results in this thesis demonstrated that spectroscopic techniques such as Raman and XRD can be used to understand material processing of c-LLZO solid state electrolyte candidate material. Furthermore, the work presented here focused on understanding and improving

processing methods so that the commercialization of an all solid-state lithium-ion battery can be achieved.

Future Directions

Stress Induced Phase Transitions for LLZO

Polymorphism in LLZO is often considered an area of concern when trying to obtain a high phase pure *c*-LLZO product during material processing. However, due to the high mechanical toughness of *t*-LLZO, a targeted mix phase material can provide some material benefits. Specifically, fracture toughness of a mixed phase *t*-LLZO/*c*-LLZO can mitigate Li dendrite growth through what is known as stress induced phase transformation. Dendrite growth propagates through pores/flaws in the material but is resisted due to mechanical properties of the material. The balance between the electrochemical driving force of dendrite propagation and

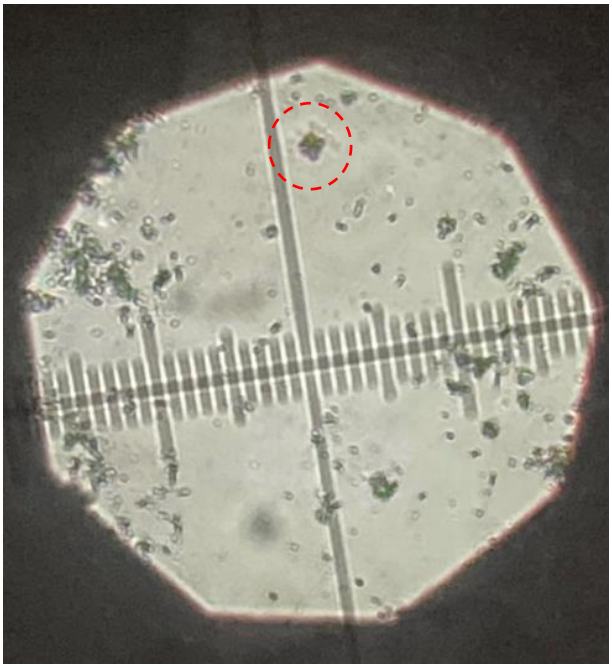

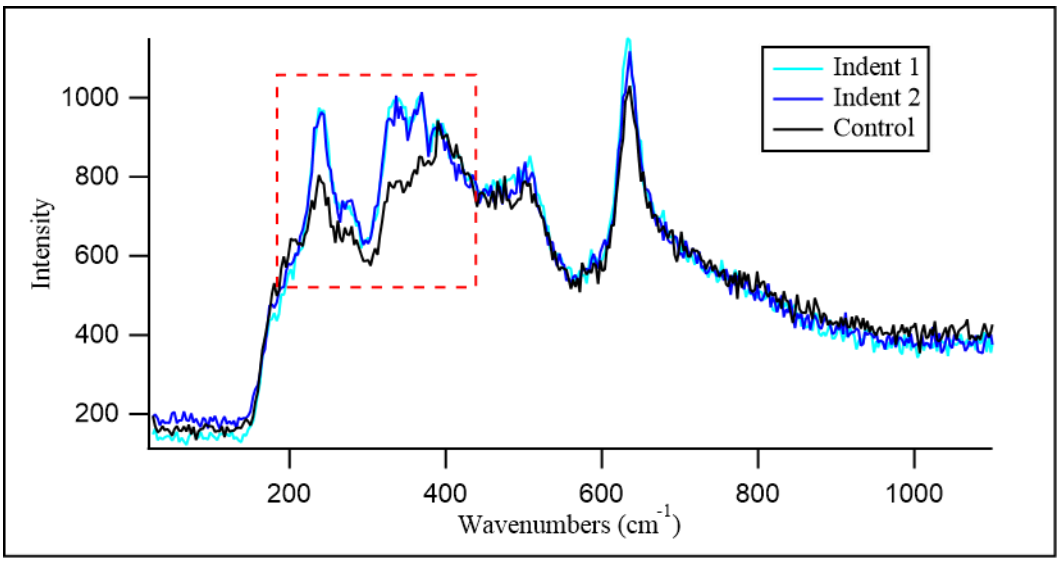

Figure 1a. Image through microscope objective of indented c-LLZO pellet. 1b. Raman spectra for indent 1 and 2 on c-LLZO pellet and control measurement.

mechanical toughness, which determines the rate of dendrite formation. By synthesizing Al-doped *c*-LLZO close to the phase stability limit, when dendrite or other mechanical force is applied to the electrolyte system, instead of dendrite propagation, phase change from the cubic form to the tetragonal form occurs, filling flaws, preventing dendrite propagation.[158, 168]

Specifically, Al doped *c*-LLZO replaces one Li^{+} for every Al^{3+} added into the material, and creates 2 additional Li^{+} vacancies. Typically, Al-doped *c*-LLZO has the chemical formula $Li_{6.25}Al_{0.25}La_3Zr_2O_{12}$, however to effectively allow phase transitions from *c*-LLZO to *t*-LLZO, doping close to the phase stability limit is necessary. Substituting in 0.16 stoichiometric amount of Al or $Al^{3+}{}_{0.16}$ ($Li_{6.52}Al_{0.16}La_3Zr_2O_{12}$) could achieve this stress induced phase transition because the $Al^{3+}{}_{0.16}$ is at the boundary between *c*-LLZO and *t*-LLZO phase stability.

To test this hypothesis micro-indentation-based fracture toughness measurements paired with Raman spectroscopy were used to characterize strain in the phonon modes of c-LLZO to

determine if a transition to *t*-LLZO was achieved. Figure 1a. shows in dotted red circle an indent on a $Al^{3+}_{0.16}$ 2hr sintered *c*-LLZO pellet. The diamond shape comes from the diamond tip from the Leco LM 700-AT indenter. Image was taken through 50x microscope objective focused on sample surface using a Renishaw InVia Raman microscope assembly. Raman spectra from the different locations are shown in Figure 1b. The first spectrum shown in light blue is what is known as Indent 1 (Figure 1a). The second spectrum is Indent 2, which is another of 12 indents on this c-LLZO pellet. The third spectrum is a control measurement of that is taken ~40 microns away from any other prominent feature on the surface. Raman data show three peaks for the Li-O stretching feature indicative of t-LLZO for both indent measurements, whereas the control measurement is indicative of a more singular Li-O peak indicating c-LLZO. This difference of 200+ intensity at ~350 cm^{-1} represents a stress induced phase transformation.

Collaborators in the Sofie Research group at Montana State University Mechanical and Industrial Engineering Department who manufactured the pellets shown here also indented and characterized the pellets using fracture toughness and ionic conductivity. These results are shown in Table 1. Toughness values determined for $Al^{3+}_{0.24}$ and $Al^{3+}_{0.20}$ c-LLZO are approximately 3-4 times smaller than $Al^{3+}_{0.16}$ while having ionic conductivity values 4 times greater. This one to one ratio of toughness to ionic conductivity for pellets shows great promise because modeling for critical current density (CCD) suggests that CCD depends on ionic conductivity to the first power but toughness to the fourth power.

Table 1. Indent fracture toughness and toughness of different dopant concentration and sintering times. The error bars are standard errors. Data generated by the Sophie Research Lab.

Sample	Fracture Toughness [MPa-$m^{1/2}$] [26]	Toughness [J/m^2] [31]	Ionic Conductivity [mS/cm]	Density [%]
$Al^{3+}_{0.24}$	0.76 ± 0.03	3.85 ± 0.36	0.40	87
$Al^{3+}_{0.20}$	0.68 ± 0.05	3.04 ± 0.45	0.15	81
$Al^{3+}_{0.16}$ 2 hr	1.15 ± 0.07	9.44 ± 1.4	0.09	84
$Al^{3+}_{0.16}$ 4 hr	1.45 ± 0.06	13.3 ± 1.0	0.11	87

Continued work on stress induced phase transformations for c-LLZO could radically improve chances for commercialization of c-LLZO. Improvements in chemical stability and mechanical toughness are the two requirements for using c-LLZO in commercial batteries. This work has the potential to improve mechanical toughness.

Continued Work on Heat Treatment vs Mechanical Polish Surface Cleaning Methods

Chapter 4 included work suggested interesting opportunities to prepare dense *c*-LLZO samples for use in solid state batteries. Thermally treating samples after sintering was tested as an alternative to surface polishing. While results were suggestive, considerable more work can be done to fully explore thermal treatment as a processing method. Specifically, a total of 14 pellets were tested in 3 batches of 2, 6, and 6. More testing is necessary to investigate chemical stability improvement for mechanical polished vs annealed samples. Other than further reproducibility testing, more electrochemical studies are necessary, such as formation of c-LLZO batteries to test critical current density of annealed pellets vs. performance of mechanically polished pellets. Additionally, a new Renishaw In Via microscope has the capabilities to measure surface roughness of a pellet surface by moving the XYZ stage, taking spectroscopic measurements

every step, including an auto focus in the vertical direction. This technique can be used to determine the approximate surface roughness and then make a 3-D model of the sample. Using this technique and comparing mechanically polished vs annealed samples can determine if the difference in electrochemical performance is due to surface roughness or a different cause. AFM measurements would be used to verify the Raman surface model.

CUMULATIVE REFERENCES CITED

(1) Vlack, H. L. *Elements of materials science and engineering*; Pearson, 1959.

(2) *Building a Voltaic Pile*; ACS.

(3) Hayyan, M.; Mjalli, F. S.; Hashim, M. A.; AlNashef, I. M.; Mei, T. X. Investigating the electrochemical windows of ionic liquids. *Journal of Industrial and Engineering Chemistry* **2013**, *19* (1), 106-112. DOI: https://doi.org/10.1016/j.jiec.2012.07.011.

(4) Thompson, T.; Yu, S.; Williams, L.; Schmidt, R. D.; Garcia-Mendez, R.; Wolfenstine, J.; Allen, J. L.; Kioupakis, E.; Siegel, D. J.; Sakamoto, J. Electrochemical Window of the Li-Ion Solid Electrolyte Li7La3Zr2O12. *ACS Energy Letters* **2017**, *2* (2), 462-468. DOI: 10.1021/acsenergylett.6b00593.

(5) Marchiori, C. F. N.; Carvalho, R. P.; Ebadi, M.; Brandell, D.; Araujo, C. M. Understanding the Electrochemical Stability Window of Polymer Electrolytes in Solid-State Batteries from Atomic-Scale Modeling: The Role of Li-Ion Salts. *Chemistry of Materials* **2020**, *32* (17), 7237-7246. DOI: 10.1021/acs.chemmater.0c01489.

(6) Zhan, X.; Li, M. M.; Weller, J. M.; Sprenkle, V. L.; Li, G. Recent Progress in Cathode Materials for Sodium-Metal Halide Batteries. In *Materials*, 2021; Vol. 14.

(7) Britannica. *Alessandro Volta*. 2024. https://www.britannica.com/biography/Alessandro-Volta (accessed 2025 Febuary).

(8) Kurzweil, P. Gaston Planté and his invention of the lead–acid battery—The genesis of the first practical rechargeable battery. *Journal of Power Sources* **2010**, *195* (14), 4424-4434. DOI: https://doi.org/10.1016/j.jpowsour.2009.12.126.

(9) Rapier, R. The Lead-Acid Battery's Demise Has Been Greatly Exaggerated. *Forbes*, 2019.

(10) Oliveri, R. L.; Insinga, M. G.; Pisana, S.; Patella, B.; Aiello, G.; Inguanta, R. High-Performance Lead-Acid Batteries Enabled by Pb and PbO2 Nanostructured Electrodes: Effect of Operating Temperature. In *Applied Sciences*, 2021; Vol. 11.

(11) Bauknecht, S.; Wätzold, F.; Schlösser, A.; Kowal, J. Comparing the Cold-Cranking Performance of Lead-Acid and Lithium Iron Phosphate Batteries at Temperatures below 0 °C. In *Batteries*, 2023; Vol. 9.

(12) Joseph T. Kummer, N. W. Battery having a molten alkali metal anode and a molten sulfur cathode. United States 1968.
(13) Hwang, J.-Y.; Myung, S.-T.; Sun, Y.-K. Sodium-ion batteries: present and future. *Chemical Society Reviews* **2017**, *46* (12), 3529-3614, 10.1039/C6CS00776G. DOI: 10.1039/C6CS00776G.

(14) Erik D. Spoerke, V. D., Hill Balliet. *Technology Strategy Assessment Findings from Storage Innovations 2030 Sodium Batteries*; Department of Energy, Department of Energy, 2023.

(15) Che, H.; Yang, X.; Wang, H.; Liao, X.-Z.; Zhang, S. S.; Wang, C.; Ma, Z.-F. Long cycle life of sodium-ion pouch cell achieved by using multiple electrolyte additives. *Journal of Power Sources* **2018**, *407*, 173-179. DOI: https://doi.org/10.1016/j.jpowsour.2018.08.025.

(16) Yabuuchi, N.; Kubota, K.; Dahbi, M.; Komaba, S. Research Development on Sodium-Ion Batteries. *Chemical Reviews* **2014**, *114* (23), 11636-11682. DOI: 10.1021/cr500192f.

(17) Guo, W.; Feng, T.; Li, W.; Hua, L.; Meng, Z.; Li, K. Comparative life cycle assessment of sodium-ion and lithium iron phosphate batteries in the context of carbon neutrality. *Journal of Energy Storage* **2023**, *72*, 108589. DOI: https://doi.org/10.1016/j.est.2023.108589.

(18) Scrosati, B.; Garche, J. Lithium batteries: Status, prospects and future. *Journal of Power Sources* **2010**, *195* (9), 2419-2430. DOI: https://doi.org/10.1016/j.jpowsour.2009.11.048.

(19) Evarts, E. C. Lithium batteries: To the limits of lithium. *Nature* **2015**, *526* (7575), S93-S95. DOI: 10.1038/526S93a.

(20) Li, Q.; Yang, Y.; Yu, X.; Li, H. A 700 W·h·kg−1 Rechargeable Pouch Type Lithium Battery. *Chinese Physics Letters* **2023**, *40* (4), 048201. DOI: 10.1088/0256-307X/40/4/048201.

(21) Wang, A.; Kadam, S.; Li, H.; Shi, S.; Qi, Y. Review on modeling of the anode solid electrolyte interphase (SEI) for lithium-ion batteries. *npj Computational Materials* **2018**, *4* (1), 15. DOI: 10.1038/s41524-018-0064-0.

(22) Nitta, N.; Wu, F.; Lee, J. T.; Yushin, G. Li-ion battery materials: present and future. *Materials Today* **2015**, *18* (5), 252-264. DOI: https://doi.org/10.1016/j.mattod.2014.10.040.

(23) Fergus, J. W. Recent developments in cathode materials for lithium ion batteries. *Journal of Power Sources* **2010**, *195* (4), 939-954. DOI: https://doi.org/10.1016/j.jpowsour.2009.08.089.

(24) Park, S.; Jeong, S. Y.; Lee, T. K.; Park, M. W.; Lim, H. Y.; Sung, J.; Cho, J.; Kwak, S. K.; Hong, S. Y.; Choi, N.-S. Replacing conventional battery electrolyte additives with dioxolone derivatives for high-energy-density lithium-ion batteries. *Nature Communications* **2021**, *12* (1), 838. DOI: 10.1038/s41467-021-21106-6.

(25) Lochala, J. A.; Zhang, H.; Wang, Y.; Okolo, O.; Li, X.; Xiao, J. Practical Challenges in Employing Graphene for Lithium-Ion Batteries and Beyond. *Small Methods* **2017**, *1* (6), 1700099. DOI: https://doi.org/10.1002/smtd.201700099 (acccessed 2025/02/28).
(26) Zhang, X.; Liwen, J.; Ozan, T.; Yinzheng, L.; and Alcoutlabi, M. Electrospun Nanofiber-Based Anodes, Cathodes, and Separators for Advanced Lithium-Ion Batteries. *Polymer Reviews* **2011**, *51* (3), 239-264. DOI: 10.1080/15583724.2011.593390.

(27) Yang, Y.-P.; Huang, A.-C.; Tang, Y.; Liu, Y.-C.; Wu, Z.-H.; Zhou, H.-L.; Li, Z.-P.; Shu, C.-M.; Jiang, J.-C.; Xing, Z.-X. Thermal Stability Analysis of Lithium-Ion Battery Electrolytes Based on Lithium Bis(trifluoromethanesulfonyl)imide-Lithium Difluoro(oxalato)Borate Dual-Salt. In *Polymers*, 2021; Vol. 13.

(28) Zallocco, V. M.; Freitas, J. M.; Bocchi, N.; Rodrigues, A. C. M. Electrochemical stability of a NASICON solid electrolyte from the lithium aluminum germanium phosphate (LAGP) series. *Solid State Ionics* **2022**, *378*, 115888. DOI: https://doi.org/10.1016/j.ssi.2022.115888.

(29) Khan, F. M. N. U.; Rasul, M. G.; Sayem, A. S. M.; Mandal, N. Maximizing energy density of lithium-ion batteries for electric vehicles: A critical review. *Energy Reports* **2023**, *9*, 11-21. DOI: https://doi.org/10.1016/j.egyr.2023.08.069.

(30) Niu, H.; Zhang, N.; Lu, Y.; Zhang, Z.; Li, M.; Liu, J.; Zhang, N.; Song, W.; Zhao, Y.; Miao, Z. Strategies toward the development of high-energy-density lithium batteries. *Journal of Energy Storage* **2024**, *88*, 111666. DOI: https://doi.org/10.1016/j.est.2024.111666.

(31) a123Systems. 2025. https://www.a123systems.com/Product/12V.html (accessed.

(32) Inc, H. E. *Lithium Ion*. 2024. https://www.hardingenergy.com/lithium-2/ (accessed.

(33) Lain, M. J.; Brandon, J.; Kendrick, E. Design Strategies for High Power vs. High Energy Lithium Ion Cells. In *Batteries*, 2019; Vol. 5.

(34) Jenu, S.; Hentunen, A.; Haavisto, J.; Pihlatie, M. State of health estimation of cycle aged large format lithium-ion cells based on partial charging. *Journal of Energy Storage* **2022**, *46*, 103855. DOI: https://doi.org/10.1016/j.est.2021.103855.

(35) Zhang, J.; Jiang, G.; Xu, P.; Ghorbani Kashkooli, A.; Mousavi, M.; Yu, A.; Chen, Z. An all-aqueous redox flow battery with unprecedented energy density. *Energy & Environmental Science* **2018**, *11* (8), 2010-2015, 10.1039/C8EE00686E. DOI: 10.1039/C8EE00686E.

(36) Andriunas, I.; Milojevic, Z.; Wade, N.; Das, P. K. Impact of solid-electrolyte interphase layer thickness on lithium-ion battery cell surface temperature. *Journal of Power Sources* **2022**, *525*, 231126. DOI: https://doi.org/10.1016/j.jpowsour.2022.231126.

(37) Liu, Q.; Sun, Y.; Wang, S.; An, Q.; Duan, L.; Zhao, G.; Wang, C.; Doyle-Davis, K.; Guo, H.; Sun, X. Highly adaptable SEI/CEI interfacial layers enabling remarkable performance of high-nickel solid-state batteries. *Materials Today* **2023**, *64*, 21-30. DOI: https://doi.org/10.1016/j.mattod.2023.02.011.

(38) Kiani, S.; Gharibi, H.; Javadian, S.; Zhiani, M.; Kashani, H. The effect of the SEI layer on the electrochemical impedance in the graphite/ Li[Ni0.5Mn0.3Co0.2]O2 lithium-ion full cells. *Applied Surface Science* **2023**, *633*, 157638. DOI: https://doi.org/10.1016/j.apsusc.2023.157638.

(39) Sun, S.-Y.; Zhang, X.-Q.; Wang, Y.-N.; Li, J.-L.; Zheng, Z.; Huang, J.-Q. Understanding the transport mechanism of lithium ions in solid-electrolyte interphase in lithium metal batteries with liquid electrolytes. *Materials Today* **2024**, *77*, 39-65. DOI: https://doi.org/10.1016/j.mattod.2024.06.001.

(40) Zhang, X.; Wang, Q. J.; Harrison, K. L.; Jungjohann, K.; Boyce, B. L.; Roberts, S. A.; Attia, P. M.; Harris, S. J. Rethinking How External Pressure Can Suppress Dendrites in Lithium Metal Batteries. *Journal of The Electrochemical Society* **2019**, *166* (15), A3639. DOI: 10.1149/2.0701914jes.

(41) Fincher, C. D.; Athanasiou, C. E.; Gilgenbach, C.; Wang, M.; Sheldon, B. W.; Carter, W. C.; Chiang, Y.-M. Controlling dendrite propagation in solid-state batteries with engineered stress. *Joule* **2022**, *6* (12), 2794-2809. DOI: https://doi.org/10.1016/j.joule.2022.10.011.

(42) Larsson, F.; Andersson, P.; Blomqvist, P.; Mellander, B. E. Toxic fluoride gas emissions from lithium-ion battery fires. *Sci Rep* **2017**, *7* (1), 10018. DOI: 10.1038/s41598-017-09784-z From NLM.

(43) Rieh, J. S. 5.01 - SiGe/Si Heterojunction Bipolar Transistors and Circuits. In *Comprehensive Semiconductor Science and Technology*, Bhattacharya, P., Fornari, R., Kamimura, H. Eds.; Elsevier, 2011; pp 1-51.

(44) Han, X.; Zhong, H.; Li, K.; Xue, X.; Wu, W.; Hu, N.; Lu, X.; Huang, J.; Xiao, G.; Mai, Y.; et al. Operando monitoring of dendrite formation in lithium metal batteries via ultrasensitive tilted fiber Bragg grating sensors. *Light: Science & Applications* **2024**, *13* (1), 24. DOI: 10.1038/s41377-023-01346-5.

(45) Tikekar, M. D.; Choudhury, S.; Tu, Z.; Archer, L. A. Design principles for electrolytes and interfaces for stable lithium-metal batteries. *Nature Energy* **2016**, *1* (9), 16114. DOI: 10.1038/nenergy.2016.114.

(46) Ma, T.; Ni, Y.; Wang, Q.; Xiao, J.; Huang, Z.; Tao, Z.; Chen, J. Lithium dendrites inhibition by regulating electrodeposition kinetics. *Energy Storage Materials* **2022**, *52*, 69-75. DOI: https://doi.org/10.1016/j.ensm.2022.07.038.

(47) Cao, J.; Sun, Y.; Zhang, D.; Luo, D.; Wu, H.; Wang, X.; Yang, C.; Zhang, L.; Yang, X.; Qin, J. Regulating Electrode/Electrolyte Interface with Additives towards Dendrite-Free Zinc-Ion Batteries. *ChemElectroChem* **2024**, *11* (13), e202400064. DOI: https://doi.org/10.1002/celc.202400064 (acccessed 2025/02/28).

(48) Ding, L.; Li, D.; Zhao, S.; Zhang, Y.; Zhang, S.; Zhang, S.; Wang, Z.; Du, F.; Zhang, P.; Yang, F. Separator porous skeleton regulation dependency on lithium-ion and lithium-metal battery performances. *Journal of Power Sources* **2024**, *624*, 235584. DOI: https://doi.org/10.1016/j.jpowsour.2024.235584.

(49) Yu, Z.; Cui, Y.; Bao, Z. Design Principles of Artificial Solid Electrolyte Interphases for Lithium-Metal Anodes. *Cell Reports Physical Science* **2020**, *1* (7), 100119. DOI: https://doi.org/10.1016/j.xcrp.2020.100119.

(50) Boaretto, N.; Garbayo, I.; Valiyaveettil-SobhanRaj, S.; Quintela, A.; Li, C.; Casas-Cabanas, M.; Aguesse, F. Lithium solid-state batteries: State-of-the-art and challenges for materials, interfaces and processing. *Journal of Power Sources* **2021**, *502*, 229919. DOI: https://doi.org/10.1016/j.jpowsour.2021.229919.

(51) Daems, K.; Yadav, P.; Dermenci, K. B.; Van Mierlo, J.; Berecibar, M. Advances in inorganic, polymer and composite electrolytes: Mechanisms of Lithium-ion transport and pathways to enhanced performance. *Renewable and Sustainable Energy Reviews* **2024**, *191*, 114136. DOI: https://doi.org/10.1016/j.rser.2023.114136.

(52) Alkhalidi, A.; Khawaja, M. K.; Ismail, S. M. Solid-state batteries, their future in the energy storage and electric vehicles market. *Science Talks* **2024**, *11*, 100382. DOI: https://doi.org/10.1016/j.sctalk.2024.100382.

(53) Xia, S.; Wu, X.; Zhang, Z.; Cui, Y.; Liu, W. Practical Challenges and Future Perspectives of All-Solid-State Lithium-Metal Batteries. *Chem* **2019**, *5* (4), 753-785. DOI: https://doi.org/10.1016/j.chempr.2018.11.013.

(54) Dai, Y.; Panahi, A. Thermal runaway process in lithium-ion batteries: A review. *Next Energy* **2025**, *6*, 100186. DOI: https://doi.org/10.1016/j.nxener.2024.100186.

(55) Liu, Z.; Li, X.; Zhang, H.; Huang, K.; Yu, Y. Are solid-state batteries absolutely more environmentally friendly compared to traditional batteries-analyzing from the footprint family viewpoint. *Journal of Cleaner Production* **2024**, *447*, 141452. DOI: https://doi.org/10.1016/j.jclepro.2024.141452.

(56) Li, Q.; Li, Y.; Wang, Y.; Zhao, X.; Wang, T.; Liu, J. Achieving fast ionic conductivity and high electrochemical stability through polyhedral structure design. *Energy Storage Materials* **2022**, *47*, 70-78. DOI: https://doi.org/10.1016/j.ensm.2022.01.050.

(57) Wang, S.; Zhang, Y.; Zhang, X.; Liu, T.; Lin, Y.-H.; Shen, Y.; Li, L.; Nan, C.-W. High-Conductivity Argyrodite Li6PS5Cl Solid Electrolytes Prepared via Optimized Sintering Processes for All-Solid-State Lithium–Sulfur Batteries. *ACS Applied Materials & Interfaces* **2018**, *10* (49), 42279-42285. DOI: 10.1021/acsami.8b15121.

(58) Minkiewicz, J.; Jones, G. M.; Ghanizadeh, S.; Bostanchi, S.; Wasely, T. J.; Yamini, S. A.; Nekouie, V. Large-scale manufacturing of solid-state electrolytes: Challenges, progress, and prospects. *Open Ceramics* **2023**, *16*, 100497. DOI: https://doi.org/10.1016/j.oceram.2023.100497.

(59) Lou, S.; Zhang, F.; Fu, C.; Chen, M.; Ma, Y.; Yin, G.; Wang, J. Interface Issues and Challenges in All-Solid-State Batteries: Lithium, Sodium, and Beyond. *Advanced Materials* **2021**, *33* (6), 2000721. DOI: https://doi.org/10.1002/adma.202000721 (acccessed 2025/02/28).

(60) Sarfraz, N.; Kanwal, N.; Ali, M.; Ali, K.; Hasnain, A.; Ashraf, M.; Ayaz, M.; Ifthikar, J.; Ali, S.; Hendi, A.; et al. Materials advancements in solid-state inorganic electrolytes for highly anticipated all solid Li-ion batteries. *Energy Storage Materials* **2024**, *71*, 103619. DOI: https://doi.org/10.1016/j.ensm.2024.103619.

(61) Machín, A.; Morant, C.; Márquez, F. Advancements and Challenges in Solid-State Battery Technology: An In-Depth Review of Solid Electrolytes and Anode Innovations. In *Batteries*, 2024; Vol. 10.

(62) Voronin, V. I.; Sherstobitova, E. A.; Blatov, V. A.; Shekhtman, G. S. Lithium-cation conductivity and crystal structure of lithium diphosphate. *Journal of Solid State Chemistry* **2014**, *211*, 170-175. DOI: https://doi.org/10.1016/j.jssc.2013.12.015.

(63) Wang, J.; He, T.; Yang, X.; Cai, Z.; Wang, Y.; Lacivita, V.; Kim, H.; Ouyang, B.; Ceder, G. Design principles for NASICON super-ionic conductors. *Nature Communications* **2023**, *14* (1), 5210. DOI: 10.1038/s41467-023-40669-0.

(64) Kodama, M.; Komiyama, S.; Ohashi, A.; Horikawa, N.; Kawamura, K.; Hirai, S. High-pressure in situ X-ray computed tomography and numerical simulation of sulfide solid electrolyte. *Journal of Power Sources* **2020**, *462*, 228160. DOI: https://doi.org/10.1016/j.jpowsour.2020.228160.

(65) Lee, Y.; Jeong, J.; Lee, H. J.; Kim, M.; Han, D.; Kim, H.; Yuk, J. M.; Nam, K.-W.; Chung, K. Y.; Jung, H.-G.; et al. Lithium Argyrodite Sulfide Electrolytes with High Ionic Conductivity and Air Stability for All-Solid-State Li-Ion Batteries. *ACS Energy Letters* **2022**, *7* (1), 171-179. DOI: 10.1021/acsenergylett.1c02428.

(66) Bannister, D. J.; Davies, G. R.; Ward, I. M.; McIntyre, J. E. Ionic conductivities for poly(ethylene oxide) complexes with lithium salts of monobasic and dibasic acids and blends of poly(ethylene oxide) with lithium salts of anionic polymers. *Polymer* **1984**, *25* (9), 1291-1296. DOI: https://doi.org/10.1016/0032-3861(84)90378-1.

(67) Yoon, H.-K.; Chung, W.-S.; Jo, N.-J. Study on ionic transport mechanism and interactions between salt and polymer chain in PAN based solid polymer electrolytes containing LiCF3SO3. *Electrochimica Acta* **2004**, *50* (2), 289-293. DOI: https://doi.org/10.1016/j.electacta.2004.01.095.
(68) Septiana, A. R.; Honggowiranto, W.; Sudaryanto; Kartini, E.; Hidayat, R. Comparative study on the ionic conductivities and redox properties of LiPF6 and LiTFSI electrolytes and the characteristics of their rechargeable lithium ion batteries. *IOP Conference Series: Materials Science and Engineering* **2018**, *432* (1), 012061. DOI: 10.1088/1757-899X/432/1/012061.

(69) Ohta, S.; Kobayashi, T.; Asaoka, T. High lithium ionic conductivity in the garnet-type oxide Li7−X La3(Zr2−X, NbX)O12 (X=0–2). *Journal of Power Sources* **2011**, *196* (6), 3342-3345. DOI: https://doi.org/10.1016/j.jpowsour.2010.11.089.

(70) Kravchyk, K. V.; Karabay, D. T.; Kovalenko, M. V. On the feasibility of all-solid-state batteries with LLZO as a single electrolyte. *Scientific Reports* **2022**, *12* (1), 1177. DOI: 10.1038/s41598-022-05141-x.

(71) Montoya, S. T.; Shanto, S. A. H.; Walker, R. A. Lithium Volatilization and Phase Changes during Aluminum-Doped Cubic Li6.25La3Zr2Al0.25O12 (c-LLZO) Processing. In *Crystals*, 2024; Vol. 14.

(72) Zhang, L.; Zhuang, Q.; Zheng, R.; Wang, Z.; Sun, H.; Arandiyan, H.; Wang, Y.; Liu, Y.; Shao, Z. Recent advances of Li7La3Zr2O12-based solid-state lithium batteries towards high energy density. *Energy Storage Materials* **2022**, *49*, 299-338. DOI: https://doi.org/10.1016/j.ensm.2022.04.026.

(73) Xu, H.; Zhang, X.; Jiang, J.; Li, M.; Shen, Y. Ultrathin Li7La3Zr2O12@PAN composite polymer electrolyte with high conductivity for all-solid-state lithium-ion battery. *Solid State Ionics* **2020**, *347*, 115227. DOI: https://doi.org/10.1016/j.ssi.2020.115227.

(74) Xiang, X.; Liu, Y.; Chen, F.; Yang, W.; Yang, J.; Ma, X.; Chen, D.; Su, K.; Shen, Q.; Zhang, L. Crystal structure and lithium ionic transport behavior of Li site doped Li7La3Zr2O12. *Journal of the European Ceramic Society* **2020**, *40* (8), 3065-3071. DOI: https://doi.org/10.1016/j.jeurceramsoc.2020.02.054.

(75) Anderson, E.; Zolfaghar, E.; Jonderian, A.; Khaliullin, R. Z.; McCalla, E. Comprehensive Dopant Screening in Li7La3Zr2O12 Garnet Solid Electrolyte. *Advanced Energy Materials* **2024**, *14* (20), 2304025. DOI: https://doi.org/10.1002/aenm.202304025 (acccessed 2025/03/03).

(76) Karasulu, B.; Emge, S. P.; Groh, M. F.; Grey, C. P.; Morris, A. J. Al/Ga-Doped Li7La3Zr2O12 Garnets as Li-Ion Solid-State Battery Electrolytes: Atomistic Insights into Local Coordination Environments and Their Influence on 17O, 27Al, and 71Ga NMR Spectra. *Journal of the American Chemical Society* **2020**, *142* (6), 3132-3148. DOI: 10.1021/jacs.9b12685.

(77) Shin, D. O.; Oh, K.; Kim, K. M.; Park, K.-Y.; Lee, B.; Lee, Y.-G.; Kang, K. Synergistic multi-doping effects on the Li7La3Zr2O12 solid electrolyte for fast lithium ion conduction. *Scientific Reports* **2015**, *5* (1), 18053. DOI: 10.1038/srep18053.

(78) Wagner, R.; Rettenwander, D.; Redhammer, G. J.; Tippelt, G.; Sabathi, G.; Musso, M. E.; Stanje, B.; Wilkening, M.; Suard, E.; Amthauer, G. Synthesis, Crystal Structure, and Stability of Cubic Li7–xLa3Zr2–xBixO12. *Inorganic Chemistry* **2016**, *55* (23), 12211-12219. DOI: 10.1021/acs.inorgchem.6b01825.

(79) Holland, J.; Demeyere, T.; Bhandari, A.; Hanke, F.; Milman, V.; Skylaris, C.-K. A Workflow for Identifying Viable Crystal Structures with Partially Occupied Sites Applied to the Solid Electrolyte Cubic Li7La3Zr2O12. *The Journal of Physical Chemistry Letters* **2023**, *14* (45). DOI: 10.1021/acs.jpclett.3c02064.

(80) Liu, G.; Li, T.; Xing, Y.; Pan, W. Synthesis of Li7La3Zr2O12 Solid Electrolyte by Solid Phase Sintering Method. *IOP Conference Series: Materials Science and Engineering* **2019**, *678* (1), 012150. DOI: 10.1088/1757-899X/678/1/012150.

(81) Kiyek, V.; Schwab, C.; Scheld, W. S.; Roitzheim, C.; Lindner, A.; Menesklou, W.; Finsterbusch, M.; Fattakhova-Rohlfing, D.; Guillon, O. Direct Precursor Route for the Fabrication of LLZO Composite Cathodes for Solid-State Batteries. *Advanced Science* **2024**, *11* (42), 2404682. DOI: https://doi.org/10.1002/advs.202404682 (acccessed 2025/02/28).

(82) Shi, X.-L.; Chen, Z.-G. 12 - Characterizations of thermoelectric ceramics. In *Advanced Ceramics for Energy Storage, Thermoelectrics and Photonics*, Cao, P., Chen, Z.-G., Xia, Z. Eds.; Elsevier, 2023; pp 305-326.

(83) Gordon, K. C. Special Issue “Raman Spectroscopy: A Spectroscopic ‘Swiss-Army Knife’”. In *Molecules*, 2019; Vol. 24.

(84) Popov, M. N.; Spitaler, J.; Veerapandiyan, V. K.; Bousquet, E.; Hlinka, J.; Deluca, M. Raman spectra of fine-grained materials from first principles. *npj Computational Materials* **2020**, *6* (1), 121. DOI: 10.1038/s41524-020-00395-3.

(85) Tietz, F.; Wegener, T.; Gerhards, M. T.; Giarola, M.; Mariotto, G. Synthesis and Raman micro-spectroscopy investigation of Li7La3Zr2O12. *Solid State Ionics* **2013**, *230*, 77-82. DOI: https://doi.org/10.1016/j.ssi.2012.10.021.

(86) Peltzer, D.; Múnera, J.; Cornaglia, L. Operando Raman spectroscopic studies of lithium zirconates during CO2 capture at high temperature. *RSC Advances* **2016**, *6* (10), 8222-8231, 10.1039/C5RA21970A. DOI: 10.1039/C5RA21970A.

(87) Scheithauer, M.; Knözinger, H.; Vannice, M. A. Raman Spectra of La2O3Dispersed on γ-Al2O3. *Journal of Catalysis* **1998**, *178* (2), 701-705. DOI: https://doi.org/10.1006/jcat.1998.2187.

(88) Zhang, S.-X.; Liu, J.; Xie, H.; Xu, L.-J.; Hu, P.-P.; Zeng, J.; Li, Z.-Z.; Liu, L.; Ai, W.-S.; Zhai, P.-F. Vibrational modes in La2Zr2O7 pyrochlore irradiated with disparate electrical energy losses*. *Chinese Physics B* **2019**, *28* (11), 116102. DOI: 10.1088/1674-1056/ab43bf.

(89) Glerup, M.; Nielsen, O. F.; Poulsen, F. W. The Structural Transformation from the Pyrochlore Structure, A2B2O7, to the Fluorite Structure, AO2, Studied by Raman Spectroscopy

and Defect Chemistry Modeling. *Journal of Solid State Chemistry* **2001**, *160* (1), 25-32. DOI: https://doi.org/10.1006/jssc.2000.9142.

(90) Yoshio Waseda , E. M., Kozo Shinoda. *X-Ray Diffraction Crystallography*; Springer, 2011.

(91) Tanzi, M. C.; Farè, S.; Candiani, G. Chapter 7 - Techniques of Analysis. In *Foundations of Biomaterials Engineering*, Tanzi, M. C., Farè, S., Candiani, G. Eds.; Academic Press, 2019; pp 393-469.

(92) Miara, L. J.; Richards, W. D.; Wang, Y. E.; Ceder, G. First-Principles Studies on Cation Dopants and Electrolyte|Cathode Interphases for Lithium Garnets. *Chemistry of Materials* **2015**, *27* (11), 4040-4047. DOI: 10.1021/acs.chemmater.5b01023.

(93) Wang, C.; Fu, K.; Kammampata, S. P.; McOwen, D. W.; Samson, A. J.; Zhang, L.; Hitz, G. T.; Nolan, A. M.; Wachsman, E. D.; Mo, Y.; et al. Garnet-Type Solid-State Electrolytes: Materials, Interfaces, and Batteries. *Chemical Reviews* **2020**, *120* (10), 4257-4300. DOI: 10.1021/acs.chemrev.9b00427.

(94) Wang, Y.; Chen, Z.; Jiang, K.; Shen, Z.; Passerini, S.; Chen, M. Accelerating the Development of LLZO in Solid-State Batteries Toward Commercialization: A Comprehensive Review. *Small* **2024**, *20* (35), 2402035. DOI: https://doi.org/10.1002/smll.202402035 (acccessed 2025/03/03).

(95) Kang, K.; Meng, Y. S.; Bréger, J.; Grey, C. P.; Ceder, G. Electrodes with High Power and High Capacity for Rechargeable Lithium Batteries. *Science* **2006**, *311* (5763), 977-980. DOI: 10.1126/science.1122152 (acccessed 2024/07/26).

(96) Fu, K.; Gong, Y.; Liu, B.; Zhu, Y.; Xu, S.; Yao, Y.; Luo, W.; Wang, C.; Lacey, S. D.; Dai, J.; et al. Toward garnet electrolyte–based Li metal batteries: An ultrathin, highly effective, artificial solid-state electrolyte/metallic Li interface. *Science Advances* **2017**, *3* (4), e1601659. DOI: 10.1126/sciadv.1601659 (acccessed 2024/07/25).

(97) Chen, R.-J.; Huang, M.; Huang, W.-Z.; Shen, Y.; Lin, Y.-H.; Nan, C.-W. Effect of calcining and Al doping on structure and conductivity of Li7La3Zr2O12. *Solid State Ionics* **2014**, *265*, 7-12. DOI: https://doi.org/10.1016/j.ssi.2014.07.004.

(98) Larraz, G.; Orera, A.; Sanjuán, M. L. Cubic phases of garnet-type Li7La3Zr2O12: the role of hydration. *Journal of Materials Chemistry A* **2013**, *1* (37), 11419-11428, 10.1039/C3TA11996C. DOI: 10.1039/C3TA11996C.

(99) Rettenwander, D.; Redhammer, G.; Preishuber-Pflügl, F.; Cheng, L.; Miara, L.; Wagner, R.; Welzl, A.; Suard, E.; Doeff, M. M.; Wilkening, M.; et al. Structural and Electrochemical Consequences of Al and Ga Cosubstitution in Li7La3Zr2O12 Solid Electrolytes. *Chemistry of Materials* **2016**, *28* (7), 2384-2392. DOI: 10.1021/acs.chemmater.6b00579.

(100) Thompson, T.; Wolfenstine, J.; Allen, J. L.; Johannes, M.; Huq, A.; David, I. N.; Sakamoto, J. Tetragonal vs. cubic phase stability in Al – free Ta doped Li7La3Zr2O12 (LLZO). *Journal of Materials Chemistry A* **2014**, *2* (33), 13431-13436, 10.1039/C4TA02099E. DOI: 10.1039/C4TA02099E.

(101) Li, Y.; Han, J.-T.; Wang, C.-A.; Xie, H.; Goodenough, J. B. Optimizing Li+ conductivity in a garnet framework. *Journal of Materials Chemistry* **2012**, *22* (30), 15357-15361, 10.1039/C2JM31413D. DOI: 10.1039/C2JM31413D.

(102) Xie, H.; Alonso, J. A.; Li, Y.; Fernández-Díaz, M. T.; Goodenough, J. B. Lithium Distribution in Aluminum-Free Cubic Li7La3Zr2O12. *Chemistry of Materials* **2011**, *23* (16), 3587-3589. DOI: 10.1021/cm201671k.

(103) Zhang, J. X.; Li, J.; Zhai, H. Y.; Tan, G. J.; Tang, X. F. One-Step Processing of Soft Electrolyte/Metallic Lithium Interface for High-Performance Solid-State Lithium Batteries. *Acs Applied Energy Materials* **2020**, *3* (7), 6139-6145. DOI: 10.1021/acsaem.0c01470.

(104) Biao, J.; Han, B.; Cao, Y.; Li, Q.; Zhong, G.; Ma, J.; Chen, L.; Yang, K.; Mi, J.; Deng, Y.; et al. Inhibiting Formation and Reduction of Li2CO3 to LiCx at Grain Boundaries in Garnet Electrolytes to Prevent Li Penetration. *Advanced Materials* **2023**, *35* (12), 2208951. DOI: https://doi.org/10.1002/adma.202208951 (acccessed 2024/07/31).

(105) Paolella, A.; Zhu, W.; Bertoni, G.; Savoie, S.; Feng, Z.; Demers, H.; Gariepy, V.; Girard, G.; Rivard, E.; Delaporte, N.; et al. Discovering the Influence of Lithium Loss on Garnet Li7La3Zr2O12 Electrolyte Phase Stability. *ACS Applied Energy Materials* **2020**, *3* (4), 3415-3424. DOI: 10.1021/acsaem.9b02401.

(106) Ping, X.; Zheng, Q.; Meng, B.; Lin, W.; Chen, Y.; Fang, C.; Zhang, H.; Liang, W. Influence of sintering atmosphere on the phase, microstructure, and lithium-ion conductivity of the Al-doped Li7La3Zr2O12 solid electrolyte. *Ceramics International* **2022**, *48* (18), 25689-25695. DOI: https://doi.org/10.1016/j.ceramint.2022.05.176.

(107) Sharafi, A.; Yu, S.; Naguib, M.; Lee, M.; Ma, C.; Meyer, H. M.; Nanda, J.; Chi, M.; Siegel, D. J.; Sakamoto, J. Impact of air exposure and surface chemistry on Li–Li7La3Zr2O12 interfacial resistance. *Journal of Materials Chemistry A* **2017**, *5* (26), 13475-13487, 10.1039/C7TA03162A. DOI: 10.1039/C7TA03162A.

(108) Kumar, K. G.; Bhargav, P. B.; Balaji, C.; Nafis, A.; Aravinth, K.; Ramasamy, P. Effect of Sintering on Structural Modification and Phase Transition of Al-Substituted LLZO Electrolytes for Solid State Battery Applications. *Journal of Electrochemical Energy Conversion and Storage* **2021**, *18* (3). DOI: 10.1115/1.4049573.

(109) Laptev, A. M.; Zheng, H.; Bram, M.; Finsterbusch, M.; Guillon, O. High-pressure field assisted sintering of half-cell for all-solid-state battery. *Materials Letters* **2019**, *247*, 155-158. DOI: 10.1016/j.matlet.2019.03.109.

(110) Heywood, S.; Lessmeier, M.; Driscoll, D.; Sofie, S. Tailoring solid-state synthesis routes for high confidence production of phase pure, low impedance Al-LLZO. *Journal of the American Ceramic Society* **2023**, *106* (5), 2786-2796. DOI: https://doi.org/10.1111/jace.18994 (acccessed 2025/03/03).

(111) Park, T.; Lee, S.; Kim, D.-M. Low-Temperature Manufacture of Cubic-Phase Li7La3Zr2O12 Electrolyte for All-Solid-State Batteries by Bed Powder. In *Crystals*, 2024; Vol. 14.

(112) Barai, P.; Fister, T.; Liang, Y.; Libera, J.; Wolfman, M.; Wang, X.; Garcia, J.; Iddir, H.; Srinivasan, V. Investigating the Calcination and Sintering of Li7La3Zr2O12 (LLZO) Solid Electrolytes Using Operando Synchrotron X-ray Characterization and Mesoscale Modeling. *Chemistry of Materials* **2021**, *33* (12), 4337-4352. DOI: 10.1021/acs.chemmater.0c04393.

(113) Lu, W.; Wang, T.; Xue, M.; Zhang, C. Improved Li6.5La3Zr1.5Nb0.5O12 electrolyte and effects of atmosphere exposure on conductivities. *Journal of Power Sources* **2021**, *497*, 229845. DOI: https://doi.org/10.1016/j.jpowsour.2021.229845.

(114) Zhang, H.; Paggiaro, G.; Okur, F.; Huwiler, J.; Cancellieri, C.; Jeurgens, L. P. H.; Chernyshov, D.; van Beek, W.; Kovalenko, M. V.; Kravchyk, K. V. On High-Temperature Thermal Cleaning of Li7La3Zr2O12 Solid-State Electrolytes. *ACS Applied Energy Materials* **2023**, *6* (13), 6972-6980. DOI: 10.1021/acsaem.3c00459.

(115) Zheng, H.; Xu, M.; He, K. Elucidating Phase Transformation and Surface Amorphization of Li7La3Zr2O12 by In Situ Heating TEM. *Small* **2024**, *20* (6), 2304799. DOI: https://doi.org/10.1002/smll.202304799 (acccessed 2025/04/15).

(116) Chen, X.; Zhong, Z.; Chen, X.; Li, H. Advancements in cathode materials for aqueous potassium-ion batteries. *Energy Storage Materials* **2025**, *74*, 103948. DOI: https://doi.org/10.1016/j.ensm.2024.103948.
(117) Wu, H.; Hao, J.; Jiang, Y.; Jiao, Y.; Liu, J.; Xu, X.; Davey, K.; Wang, C.; Qiao, S.-Z. Alkaline-based aqueous sodium-ion batteries for large-scale energy storage. *Nature Communications* **2024**, *15* (1), 575. DOI: 10.1038/s41467-024-44855-6.

(118) Li, Q.; Yu, X.; Li, H.; Chen, L. The road towards high-energy-density batteries. *The Innovation Energy* **2024**, *1* (1), 100005. DOI: 10.59717/j.xinn-energy.2024.100005.

(119) da Silva Lima, L.; Quartier, M.; Buchmayr, A.; Sanjuan-Delmás, D.; Laget, H.; Corbisier, D.; Mertens, J.; Dewulf, J. Life cycle assessment of lithium-ion batteries and vanadium redox

flow batteries-based renewable energy storage systems. *Sustainable Energy Technologies and Assessments* **2021**, *46*, 101286. DOI: https://doi.org/10.1016/j.seta.2021.101286.

(120) *Lithium-ion battery manufacturing capacity*. 2023. https://www.iea.org/data-and-statistics/charts/lithium-ion-battery-manufacturing-capacity-2022-2030 (accessed 2025 Feb).

(121) Rafiz, K.; Murali, D. R. L.; Lin, J. Y. S. Suppressing lithium dendrite growth on lithium-ion/metal batteries by a tortuously porous γ-alumina separator. *Electrochimica Acta* **2022**, *421*, 140478. DOI: https://doi.org/10.1016/j.electacta.2022.140478.

(122) Ren, W.; Zheng, Y.; Cui, Z.; Tao, Y.; Li, B.; Wang, W. Recent progress of functional separators in dendrite inhibition for lithium metal batteries. *Energy Storage Materials* **2021**, *35*, 157-168. DOI: https://doi.org/10.1016/j.ensm.2020.11.019.

(123) Cao, D.; Sun, X.; Li, Q.; Natan, A.; Xiang, P.; Zhu, H. Lithium Dendrite in All-Solid-State Batteries: Growth Mechanisms, Suppression Strategies, and Characterizations. *Matter* **2020**, *3* (1), 57-94. DOI: https://doi.org/10.1016/j.matt.2020.03.015.

(124) Sazvar, A.; Sarpoolaky, H.; Golmohammad, M. The effects of electric field on physical properties of LLZO made by flash sintering method. *Solid State Ionics* **2022**, *386*, 116054. DOI: https://doi.org/10.1016/j.ssi.2022.116054.

(125) Kern, A.; McGinn, P. J. Ultrafast high-temperature sintering of Li7La3Zr1.75Nb0.25Al0.15O12 (LLZO). *Journal of the European Ceramic Society* **2022**, *42* (16), 7501-7507. DOI: https://doi.org/10.1016/j.jeurceramsoc.2022.08.054.

(126) Košir, J.; Mousavihashemi, S.; Wilson, B. P.; Rautama, E.-L.; Kallio, T. Comparative analysis on the thermal, structural, and electrochemical properties of Al-doped Li7La3Zr2O12 solid electrolytes through solid state and sol-gel routes. *Solid State Ionics* **2022**, *380*, 115943. DOI: https://doi.org/10.1016/j.ssi.2022.115943.

(127) Ihrig, M.; Finsterbusch, M.; Tsai, C.-L.; Laptev, A. M.; Tu, C.-h.; Bram, M.; Sohn, Y. J.; Ye, R.; Sevinc, S.; Lin, S.-k.; et al. Low temperature sintering of fully inorganic all-solid-state batteries – Impact of interfaces on full cell performance. *Journal of Power Sources* **2021**, *482*, 228905. DOI: https://doi.org/10.1016/j.jpowsour.2020.228905.

(128) Yan, Z.; Song, Y.; Wu, S.; Wu, Y.; Song, S.; Wang, X.; Zhu, Y.; Chen, J.; Guo, R.; Xiang, Y. Improving the Ionic Conductivity of the LLZO–LZO Thin Film through Indium Doping. In *Crystals*, 2021; Vol. 11.

(129) Yoshikawa, K.; Yamamoto, T.; Sugumar, M. K.; Motoyama, M.; Iriyama, Y. Room Temperature Operation and High Cycle Stability of an All-Solid-State Lithium Battery Fabricated by Cold Pressing Using Soft Li2OHBr Solid Electrolyte. *Energy & Fuels* **2021**, *35* (15), 12581-12587. DOI: 10.1021/acs.energyfuels.1c01190.

(130) Chen, R.-J.; Huang, M.; Huang, W.-Z.; Shen, Y.; Lin, Y.-H.; Nan, C.-W. Sol–gel derived Li–La–Zr–O thin films as solid electrolytes for lithium-ion batteries. *Journal of Materials Chemistry A* **2014**, *2* (33), 13277-13282, 10.1039/C4TA02289K. DOI: 10.1039/C4TA02289K.

(131) Kobayashi, Y.; Tamura, S.; Imanaka, N.; Adachi, G. Quantitative demonstration of Al3+ ion conduction in Al2(WO4)3 solids. *Solid State Ionics* **1998**, *113-115*, 545-552. DOI: https://doi.org/10.1016/S0167-2738(98)00320-8.

(132) Adams, S.; Rao, R. P. Ion transport and phase transition in Li7−xLa3(Zr2−xMx)O12 (M = Ta5+, Nb5+, x = 0, 0.25). *Journal of Materials Chemistry* **2012**, *22* (4), 1426-1434, 10.1039/C1JM14588F. DOI: 10.1039/C1JM14588F.

(133) Penney, C. M.; Goldman, L. M.; Lapp, M. Raman Scattering Cross Sections. *Nature Physical Science* **1972**, *235* (58), 110-112. DOI: 10.1038/physci235110b0.

(134) Takahashi, T.; Watanabe, H. Preparation and characterization of lithium oxide. *Fusion Engineering and Design* **1989**, *8*, 399-405. DOI: https://doi.org/10.1016/S0920-3796(89)80139-5.

(135) Sharafi, A.; Kazyak, E.; Davis, A. L.; Yu, S.; Thompson, T.; Siegel, D. J.; Dasgupta, N. P.; Sakamoto, J. Surface Chemistry Mechanism of Ultra-Low Interfacial Resistance in the Solid-State Electrolyte Li7La3Zr2O12. *Chemistry of Materials* **2017**, *29* (18), 7961-7968. DOI: 10.1021/acs.chemmater.7b03002.

(136) Hu, X.; Chen, S.; Wang, Z.; Chen, Y.; Yuan, B.; Zhang, Y.; Liu, W.; Yu, Y. Microstructure of the Li–Al–O Second Phases in Garnet Solid Electrolytes. *Nano Letters* **2023**, *23* (3), 887-894. DOI: 10.1021/acs.nanolett.2c04135.

(137) Shi, J.; Wu, X.; Chen, Y.; Zhang, Y.; Hou, X.; Lv, R.; Liu, J.; Jiang, M.; Huang, K.; Feng, S. Structure factors dictate the ionic conductivity and chemical stability for cubic garnet-based solid-state electrolyte. *Chinese Chemical Letters* **2025**, *36* (5), 109938. DOI: https://doi.org/10.1016/j.cclet.2024.109938.

(138) Kang, K.; Ceder, G. Factors that affect Li mobility in layered lithium transition metal oxides. *Physical Review B* **2006**, *74* (9), 094105. DOI: 10.1103/PhysRevB.74.094105.
(139) Mizumoto, K.; Hayashi, S. Lithium Ion Mobility and Activation Energy for Lithium Ion Conduction in A-Site Deficient Perovskites La_{1/3-x}Li_{3x}TaO₃. *Journal of the Ceramic Society of Japan* **1998**, *106* (1232), 369-371. DOI: 10.2109/jcersj.106.369.

(140) Chen, S.; Hu, X.; Bao, W.; Wang, Z.; Yang, Q.; Nie, L.; Zhang, X.; Zhang, J.; Jiang, Y.; Han, Y.; et al. Low-sintering-temperature garnet oxides by conformal sintering-aid coating. *Cell Reports Physical Science* **2021**, *2* (9), 100569. DOI: https://doi.org/10.1016/j.xcrp.2021.100569.

(141) Wang, J.; Azam, W. Natural resource scarcity, fossil fuel energy consumption, and total greenhouse gas emissions in top emitting countries. *Geoscience Frontiers* **2024**, *15* (2), 101757. DOI: https://doi.org/10.1016/j.gsf.2023.101757.

(142) Amin, M.; Shah, H. H.; Fareed, A. G.; Khan, W. U.; Chung, E.; Zia, A.; Rahman Farooqi, Z. U.; Lee, C. Hydrogen production through renewable and non-renewable energy processes and their impact on climate change. *International Journal of Hydrogen Energy* **2022**, *47* (77), 33112-33134. DOI: https://doi.org/10.1016/j.ijhydene.2022.07.172.

(143) Yun, P.; Wu, H.; Alsenani, T. R.; Bouzgarrou, S. M.; Alkhalaf, S.; Alturise, F.; Almujibah, H. On the utilization of artificial intelligence for studying and multi-objective optimizing a compressed air energy storage integrated energy system. *Journal of Energy Storage* **2024**, *84*, 110839. DOI: https://doi.org/10.1016/j.est.2024.110839.

(144) Winter, M.; Brodd, R. J. What Are Batteries, Fuel Cells, and Supercapacitors? *Chemical Reviews* **2004**, *104* (10), 4245-4270. DOI: 10.1021/cr020730k.

(145) Amir, M.; Deshmukh, R. G.; Khalid, H. M.; Said, Z.; Raza, A.; Muyeen, S. M.; Nizami, A.-S.; Elavarasan, R. M.; Saidur, R.; Sopian, K. Energy storage technologies: An integrated survey of developments, global economical/environmental effects, optimal scheduling model, and sustainable adaption policies. *Journal of Energy Storage* **2023**, *72*, 108694. DOI: https://doi.org/10.1016/j.est.2023.108694.

(146) Aghmadi, A.; Mohammed, O. A. Energy Storage Systems: Technologies and High-Power Applications. In *Batteries*, 2024; Vol. 10.

(147) Blanc, L. E.; Kundu, D.; Nazar, L. F. Scientific Challenges for the Implementation of Zn-Ion Batteries. *Joule* **2020**, *4* (4), 771-799. DOI: https://doi.org/10.1016/j.joule.2020.03.002.

(148) Olabi, A. G.; Allam, M. A.; Abdelkareem, M. A.; Deepa, T. D.; Alami, A. H.; Abbas, Q.; Alkhalidi, A.; Sayed, E. T. Redox Flow Batteries: Recent Development in Main Components, Emerging Technologies, Diagnostic Techniques, Large-Scale Applications, and Challenges and Barriers. In *Batteries*, 2023; Vol. 9.

(149) Adenusi, H.; Chass, G. A.; Passerini, S.; Tian, K. V.; Chen, G. Lithium Batteries and the Solid Electrolyte Interphase (SEI)—Progress and Outlook. *Advanced Energy Materials* **2023**, *13* (10), 2203307. DOI: https://doi.org/10.1002/aenm.202203307 (acccessed 2025/03/03).

(150) Tan, K. M.; Babu, T. S.; Ramachandaramurthy, V. K.; Kasinathan, P.; Solanki, S. G.; Raveendran, S. K. Empowering smart grid: A comprehensive review of energy storage technology and application with renewable energy integration. *Journal of Energy Storage* **2021**, *39*, 102591. DOI: https://doi.org/10.1016/j.est.2021.102591.

(151) Njema, G. G.; Ouma, R. B. O.; Kibet, J. K. A Review on the Recent Advances in Battery Development and Energy Storage Technologies. *Journal of Renewable Energy* **2024**, *2024* (1), 2329261. DOI: https://doi.org/10.1155/2024/2329261 (acccessed 2025/03/03).

(152) Feng, X.; Ren, D.; He, X.; Ouyang, M. Mitigating Thermal Runaway of Lithium-Ion Batteries. *Joule* **2020**, *4* (4), 743-770. DOI: https://doi.org/10.1016/j.joule.2020.02.010.

(153) Naguib, M.; Allu, S.; Simunovic, S.; Li, J.; Wang, H.; Dudney, N. J. Limiting Internal Short-Circuit Damage by Electrode Partition for Impact-Tolerant Li-Ion Batteries. *Joule* **2018**, *2* (1), 155-167. DOI: https://doi.org/10.1016/j.joule.2017.11.003.

(154) Moradi, Z.; Lanjan, A.; Tyagi, R.; Srinivasan, S. Review on current state, challenges, and potential solutions in solid-state batteries research. *Journal of Energy Storage* **2023**, *73*, 109048. DOI: https://doi.org/10.1016/j.est.2023.109048.

(155) Li, C.; Tong, X.; Yuan, C.; Tong, Y.; Zhang, Y.; Wang, N.; Li, P.; Pang, S.; Wang, L.; Zhan, Z. Electrolyte-electrode interface: A key factor for advanced protonic ceramic electrochemical cells. *Ceramics International* **2024**, *50* (3, Part A), 4656-4664. DOI: https://doi.org/10.1016/j.ceramint.2023.11.209.

(156) Yu, S.; Schmidt, R. D.; Garcia-Mendez, R.; Herbert, E.; Dudney, N. J.; Wolfenstine, J. B.; Sakamoto, J.; Siegel, D. J. Elastic Properties of the Solid Electrolyte Li7La3Zr2O12 (LLZO). *Chemistry of Materials* **2016**, *28* (1), 197-206. DOI: 10.1021/acs.chemmater.5b03854.

(157) Kim, S.; Kim, J.-S.; Miara, L.; Wang, Y.; Jung, S.-K.; Park, S. Y.; Song, Z.; Kim, H.; Badding, M.; Chang, J.; et al. High-energy and durable lithium metal batteries using garnet-type solid electrolytes with tailored lithium-metal compatibility. *Nature Communications* **2022**, *13* (1), 1883. DOI: 10.1038/s41467-022-29531-x.

(158) Porz, L.; Swamy, T.; Sheldon, B. W.; Rettenwander, D.; Frömling, T.; Thaman, H. L.; Berendts, S.; Uecker, R.; Carter, W. C.; Chiang, Y.-M. Mechanism of Lithium Metal Penetration through Inorganic Solid Electrolytes. *Advanced Energy Materials* **2017**, *7* (20), 1701003. DOI: https://doi.org/10.1002/aenm.201701003 (acccessed 2025/04/10).

(159) Zhang, H.; Dubey, R.; Inniger, M.; Okur, F.; Wullich, R.; Parrilli, A.; Karabay, D. T.; Neels, A.; Kravchyk, K. V.; Kovalenko, M. V. Ultrafast-sintered self-standing LLZO membranes for high energy density lithium-garnet solid-state batteries. *Cell Reports Physical Science* **2023**, *4* (7), 101473. DOI: https://doi.org/10.1016/j.xcrp.2023.101473.

(160) Siniscalchi, M.; Gibson, J. S.; Tufnail, J.; Swallow, J. E. N.; Lewis, J.; Matthews, G.; Karagoz, B.; van Spronsen, M. A.; Held, G.; Weatherup, R. S.; et al. Removal and Reoccurrence of LLZTO Surface Contaminants under Glovebox Conditions. *ACS Applied Materials & Interfaces* **2024**, *16* (21), 27230-27241. DOI: 10.1021/acsami.4c00444.

(161) Heywood, S.; Sofie, S.; Driscoll, D. Solid State Synthesis of Aluminum Doped Li7La3Zr2O12 Garnet with Enhanced Thermal Processing Stability. *ECS Meeting Abstracts* **2022**, *MA2022-01* (6), 2427. DOI: 10.1149/MA2022-0162427mtgabs.

(162) Wang, J.-C.; Li, Y.; Li, Z.-X.; Wang, P.-F.; Zhu, Y.-R.; Sun, Y.; Yi, T.-F. Review on Interface Issues between a Garnet Li7La3Zr2O12 Solid Electrolyte and Li Anode: Advances and Perspectives. *Energy & Fuels* **2024**, *38* (14), 12528-12545. DOI: 10.1021/acs.energyfuels.4c02506.

(163) Huo, H.; Luo, J.; Thangadurai, V.; Guo, X.; Nan, C.-W.; Sun, X. Li2CO3: A Critical Issue for Developing Solid Garnet Batteries. *ACS Energy Letters* **2020**, *5* (1), 252-262. DOI: 10.1021/acsenergylett.9b02401.

(164) Brooker, M. H.; Wang, J. Raman and infrared studies of lithium and cesium carbonates. *Spectrochimica Acta Part A: Molecular Spectroscopy* **1992**, *48* (7), 999-1008. DOI: https://doi.org/10.1016/0584-8539(92)80176-W.

(165) Kim, M.; Park, H. G.; Park, K. A strategy of enhancing the ionic conductivity of Li7La3Zr2O12 under accurate sintering conditions. *Physical Chemistry Chemical Physics* **2022**, *24* (47), 29159-29164, 10.1039/D2CP03072A. DOI: 10.1039/D2CP03072A.

(166) Cheng, E. J.; Kushida, Y.; Abe, T.; Kanamura, K. Degradation Mechanism of All-Solid-State Li-Metal Batteries Studied by Electrochemical Impedance Spectroscopy. *ACS Applied Materials & Interfaces* **2022**, *14* (36), 40881-40889. DOI: 10.1021/acsami.2c09841.

(167) Wolfenstine, J.; Rangasamy, E.; Allen, J. L.; Sakamoto, J. High conductivity of dense tetragonal Li7La3Zr2O12. *Journal of Power Sources* **2012**, *208*, 193-196. DOI: https://doi.org/10.1016/j.jpowsour.2012.02.031.

(168) Bonilla, M. R.; García Daza, F. A.; Carrasco, J.; Akhmatskaya, E. Exploring Li-ion conductivity in cubic, tetragonal and mixed-phase Al-substituted Li7La3Zr2O12 using atomistic simulations and effective medium theory. *Acta Materialia* **2019**, *175*, 426-435. DOI: https://doi.org/10.1016/j.actamat.2019.06.033.

APPENDIX

Supporting Information for

Dopant Effects on the Thermal Stability of Li+ Conducting cubic-$Li_7La_3Zr_2O_{12}$

Due to Raman scattering cross sections it was necessary to make a 1/3 LZO, 1/3 c-LLZO, and 1/3 La_2O_3 mixture. Raman measurements were made and shown in AP Figure 1. outlining that LZO and lanthanum oxide have larger Raman scattering cross sections than c-LLZO.

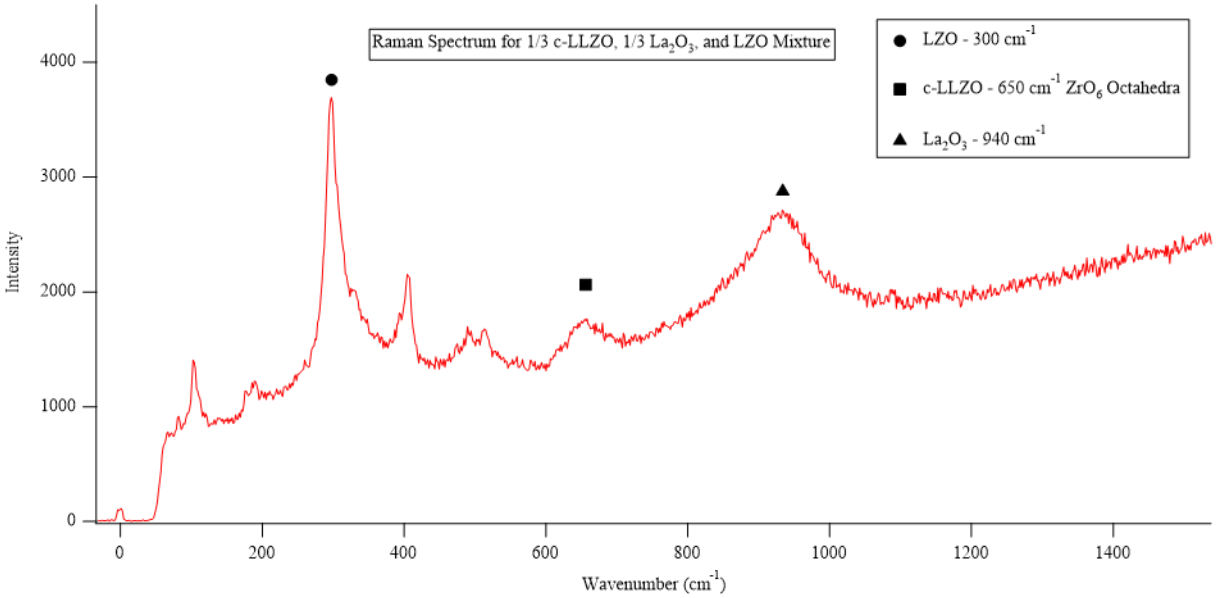

AP Figure 1

Additionally, XRD measurements were taken and Rietveld refinements were calculated generating mass percentage values from the refinement peak matching software JADE in AP Figure 2. LZO was calculated to be 52.1% by mass of the mixture, c-LLZO was calculated to be 35% by mass and lanthanum oxide is 12.9% by mass.

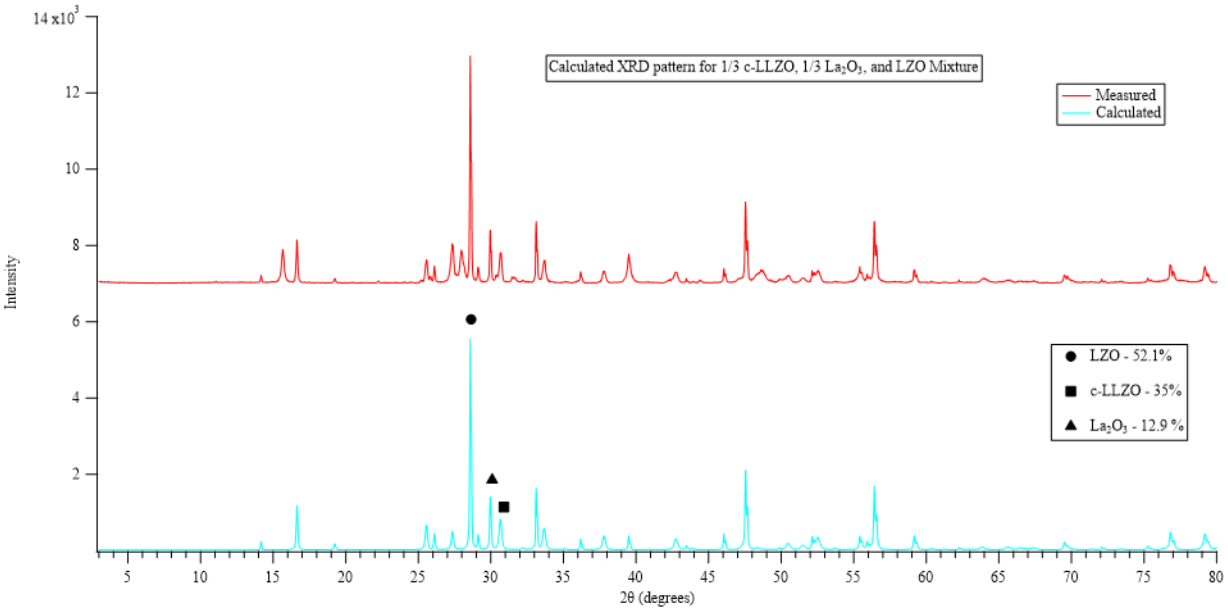

AP Figure 2

Results in AP Figure 3 are representative of Nb doped pellets sintered 1hr and 12 hr that are shown in Figure 3.4. These spectra are taken from the center of the pellet and marched outwards towards the edge, with the circle with dots modeling each spectrum measured.

Data shown in Figures AP 4, AP 5 and AP 6 are XRD patterns from pellets sintered and with LLZO and LZO mass percentages described in Table 3.4 that are not shown in the narrative.

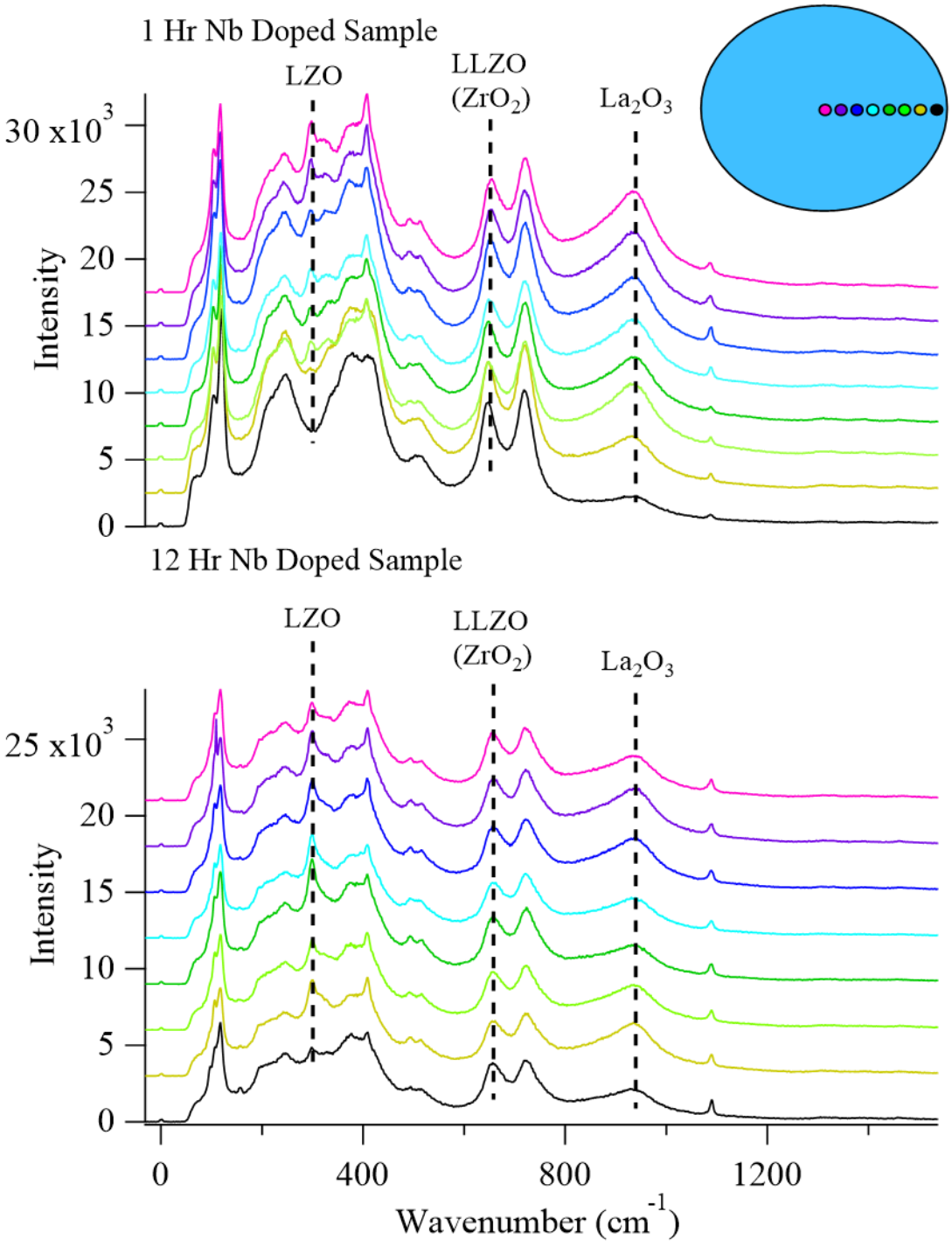

AP Figure 3. Waterfall plot showing Raman spectra for Nb doped 1hr and 12 hr sintered pellets rastering from center to edge of pellet.

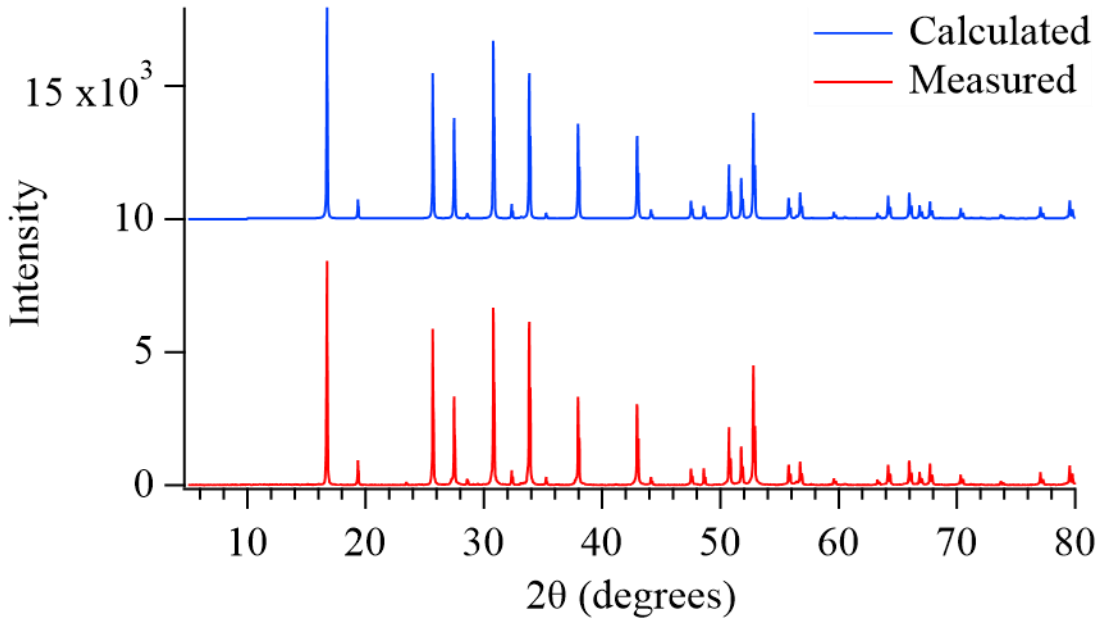

AP Figure 4. Al 1 hr sintered c-LLZO pattern.

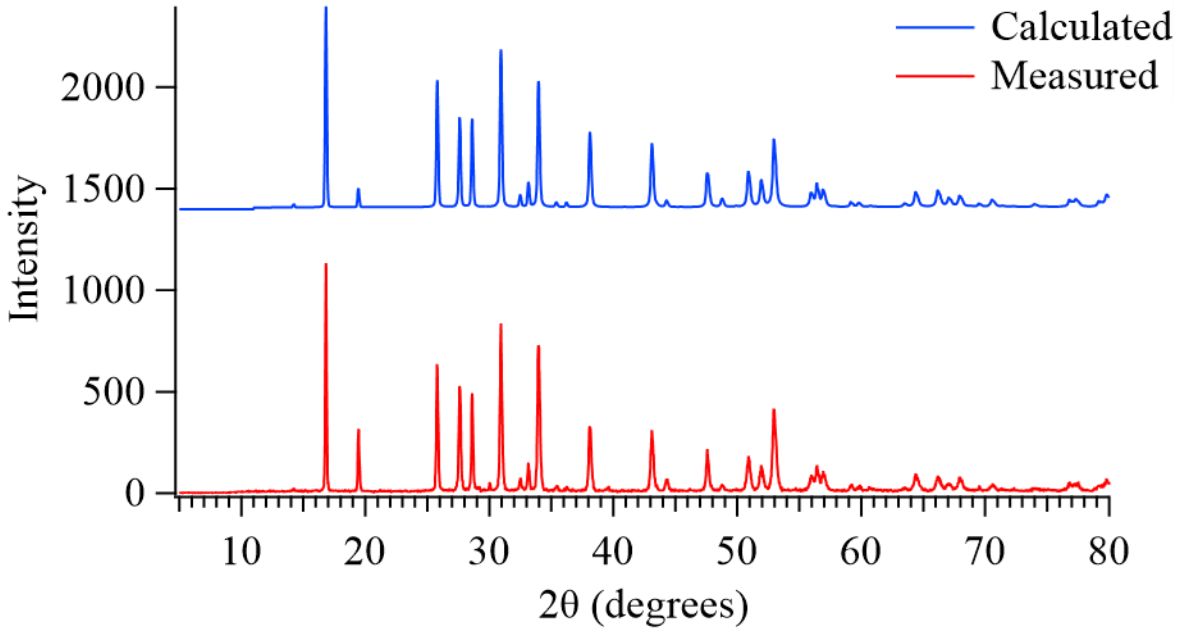

AP Figure 5. Nb 1 hr sintered c-LLZO XRD pattern.

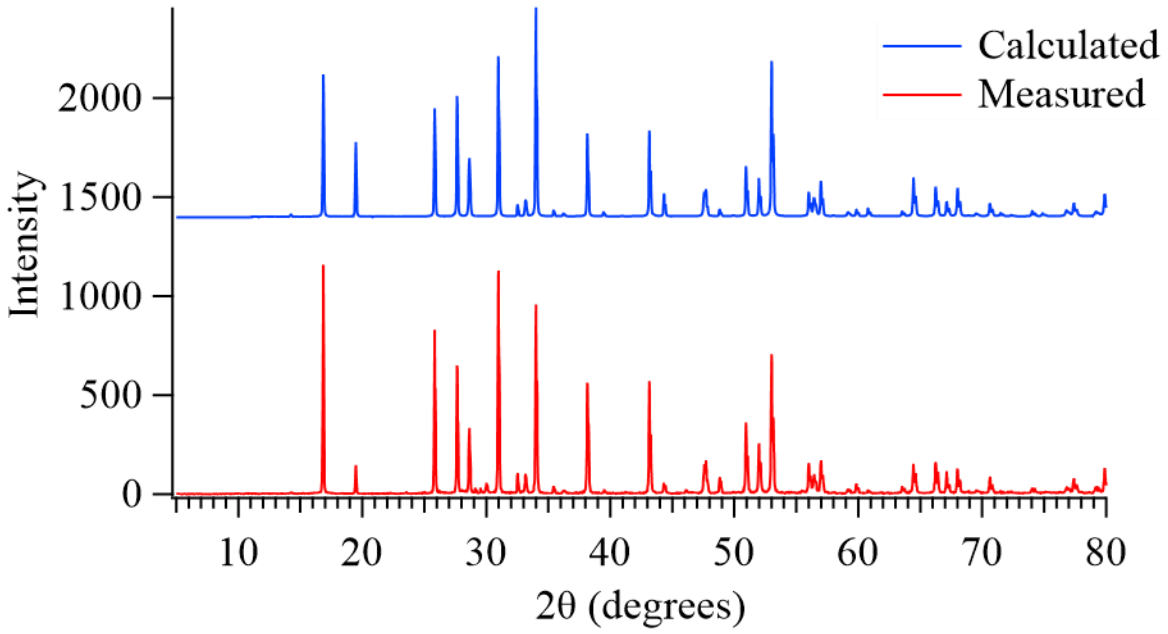

AP Figure 6. Nb 12 hr sintered c-LLZO XRD pattern.